ADDITIVE MANUFACTURE OF TISSUE ENGINEERING SCAFFOLDS FOR BONE AND CARTILAGE

A Dissertation
Presented to
The Academic Faculty

by

Shaun Eshraghi

In Partial Fulfillment
of the Requirements for the Degree
Doctor of Philosophy in the
School of Bioengineering

Georgia Institute of Technology
December 2015

ADDITIVE MANUFACTURE OF TISSUE ENGINEERING SCAFFOLDS FOR BONE AND CARTILAGE

Approved by:

Dr. Suman Das, Advisor
School of Mechanical Engineering
Georgia Institute of Technology

Dr. Wilbur Lam
School of Biomedical Engineering
Georgia Institute of Technology

Dr. Kyriaki Kalaitzidou
School of Mechanical Engineering
Georgia Institute of Technology

Dr. Jeannette Yen
School of Biology
Georgia Institute of Technology

Dr. David Ku
School of Mechanical Engineering
Georgia Institute of Technology

Date Approved: October 13, 2015

ACKNOWLEDGEMENTS

I would like to thank my advisor Dr. Suman Das for his guidance and encouragement during my research. I would also like to thank Dr. Kyriaki Kalaitzidou for her willingness to meet with me and for her expert feedback.

My PhD reading committee members: Dr. David Ku, Dr. Wilbur Lam, and Dr. Jeannette Yen have also been very insightful and provided me with invaluable direction during the proposal of my work.

I would also like to thank my fellow past and present lab members: Dr. Anirudh Rudraraju, Dr. Hassan Rashidi, Dr. Taiwo Raphael Alabi, Dr. Rohan Bansal, Justin Gambone, Dr. Dajun Yuan, Matthew Conrad, Dr. Rui Guo, Way Joe Lee, Dr. Michael Kirka, Peng Shao, Dr. Chan Yoon, Dr. Siddharth Athreya, Dr. Kiran Kambly, Paul Cilino, Dr. Tao Wu, and Dr. Ranadip Acharya.

Lastly, I would like to thank my dear fiancée Deena for her love and support during the last part of my PhD. It was her love and kindness that kept me going.

TABLE OF CONTENTS

LIST OF TABLES

Page

LIST OF FIGURES

Page

LIST OF SYMBOLS AND ABBREVIATIONS

2PP	two-photon photopolymerization
ABS	acrylonitrile butadiene styrene
CAD	computer aided design
CCITT	Consultative Committee on International Telephone
DMP	dynamic mask projection
DMD	digital micromirror device
DMLS	direct metal laser sintering
DOE	design of experiments
FDM	fused deposition modeling
HA	hydroxyapatite
ISO	International Organization for Standardization
LAMP	large area maskless photopolymerization
LENS	laser engineered net shaping
LM	laser melting
LOM	laminated object manufacturing
PC	polycarbonate
PCL	polycaprolactone
PI	proportional integral
PEGDA	polyethylene glycol diacrylate
PEEK	polyether ether ketone
PLA	polylactic acid
PPSF	polyphenylsulfone

PVA	polyvinyl alcohol
SEM	scanning electron microscope
SLA	stereolithography
SLM	selective laser melting
SLS	selective laser sintering
STL	standard tessellation language
TIFF	tagged image file format
UHMWPE	ultra high molecular weight polyethylene
UV	ultraviolet
VRML	virtual reality modeling language
XRD	x-ray diffraction

SUMMARY

Bone and cartilage constructs are often plagued with mechanical failure, poor nutrient transport, poor tissue ingrowth, and necrosis of embedded cells. However, advances in computer aided design (CAD) and computational modeling enable the design of constructs with complex internal michroarchitectures having transport and mechanical properties tailored to the tissue environment. In this dissertation two additive manufacturing techniques were investigated to determine their capabilities in manufacturing scaffolds with complex 3D microarchitectures for hard and soft tissue applications.

The design, fabrication, computational modeling, and characterization of complex 3D microarchitectured scaffolds is described in this dissertation. Selective laser sintering (SLS) was used to manufacture bioresorbable thermoplastic scaffolds out of polycaprolactone (PCL) and hydroxyapatite (HA) for bone tissue engineering. It was observed that complex 3D features as small as 700 μm could be created and that mechanical properties in the lower range of human trabecular bone (~500 MPa) could be achieved. The manufacture of polyethylene glycol diacrylate (PEGDA) hydrogel scaffolds for soft tissue applications was explored through a new technology called large area maskless photopolymerization (LAMP). LAMP is a massively parallel ultraviolet curing-based process that can be used to create hydrogel scaffolds on a large-scale (101x113 mm) having complex 3D channels as small as 0.196 mm^2 in cross-sectional area. Computational modeling that can be used to predict the mechanical properties and fluid flow properties of the scaffolds is also described.

This dissertation demonstrates that additive manufacturing techniques, namely LAMP and SLS, can be used to successfully create both hard and soft tissue scaffolds with carefully engineered 3D channels with desirable fluid flow properties while not compromising the mechanical integrity of the scaffolds. This capability could open up several new pathways in the design and fabrication of more advanced tissue constructs.

CHAPTER 1

INTRODUCTION

Additive manufacturing is an emerging field in advanced manufacturing that has shown promise in the fabrication of scaffolds for tissue engineering. Scaffolds are used in tissue engineering to act as a controlled extracellular environment where the cells can attach and differentiate. Scaffolds also act as a highway system for cells that can limit and direct their movement. In regenerative medicine, the final goal for a scaffold is to host cells that will eventually regenerate the native tissue; however, scaffolds can also have other uses in areas such as 3D cell culture.

Scaffolds that are fabricated using additive manufacturing methods can have a microarchitecture that is designed instead of the random type produced by particulate leaching or gas foaming [1, 2]. Additive manufacturing also offers a higher degree of feature resolution and repeatability that conventional manufacturing methods do not. The native geometry of human tissues can be extremely complex, and creating biomimetic structures that facilitate cell attachment and motility on the correct size-scale is not possible with current conventional manufacturing techniques [3]. However, fundamental research into additive manufacturing may enable the creation of scaffolds with microstructures that closely match what is found in nature.

Scaffolds with designed microarchitectures have applications in areas of tissue engineering where control of the mechanical properties, transport properties, and internal geometry is desirable. Much effort has gone into rapid prototyping of bone and cartilage tissue engineering scaffolds because of the need for scaffolds with a custom external geometry and tailorable mechanical and transport properties [3]. Engineering of tissues

such as cartilage and bone has an exceptionally high demand for multifunctional scaffolds, i.e. scaffolds that are mechanically resilient to high loads while maintaining transport properties that will not cause necrosis of cells that are deep inside of large scaffolds.

1.1 Additive Manufacturing Methods

There are many different additive manufacturing methods currently found in the literature. In accordance with active Standard ASTM F2792 developed by the F42 subcommittee these methods can be divided into 7 categories [4]:

- **Binder Jetting** — an additive manufacturing process in which a liquid bonding agent is selectively deposited to join powder materials (e.g. inkjet 3D printing).
- **Directed Energy Deposition** — an additive manufacturing process in which focused thermal energy is used to fuse materials by melting as they are being deposited (e.g. laser engineered net shaping a.k.a. LENS).
- **Material Extrusion** — an additive manufacturing process in which material is selectively dispensed through a nozzle (e.g. fused deposition molding a.k.a. FDM)
- **Material Jetting** — an additive manufacturing process in which droplets of build material are selectively deposited (e.g. multi-material jetting).
- **Powder Bed Fusion** — an additive manufacturing process in which thermal energy selectively fuses regions of a powder bed (e.g. selective laser sintering a.k.a. SLS).
- **Sheet Lamination** — an additive manufacturing process in which sheets of material are bonded to form an object (e.g. laminated object manufacturing a.k.a. LOM).

- **Vat Photopolymerization** — an additive manufacturing process in which liquid photopolymer in a vat is selectively cured by light-activated polymerization (e.g. stereolithography a.k.a. SLA).

1.1.1 Binder Jetting

Binder jetting machines are also called inkjet 3D printing machines or simply 3D printing machines. The part is built in a flat bed of powder on a single axis stage. An overhead 2-axis inkjet print head moves across the powder bed and selectively deposits a binding material that causes the powder to fuse. The stage then moves the powder bed down one layer so a roller or blade can deposit the next layer of powder on top of the material that was bound. The most common material used in inkjet 3D printing machines is plaster that can be used to create a mold for casting a wide range of materials. A schematic of an inkjet 3D printer is shown in Figure 1.1.

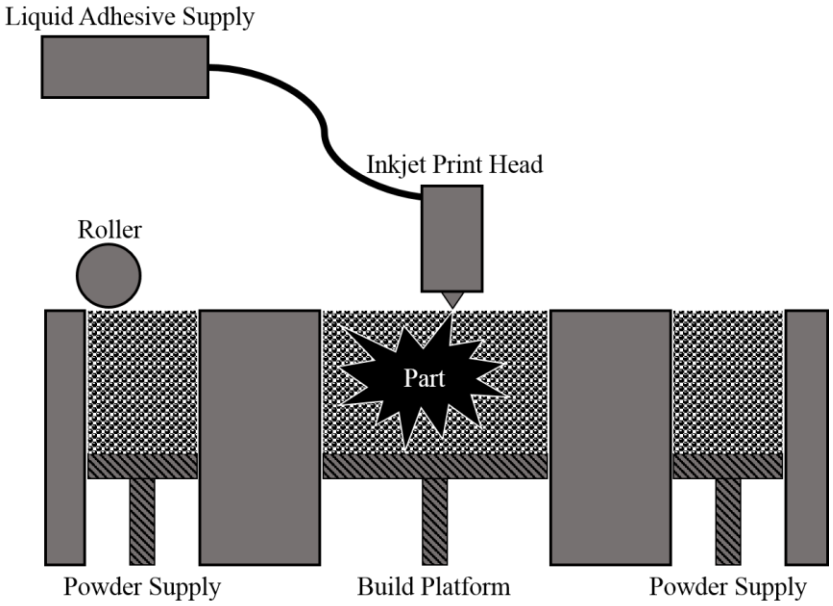

Figure 1.1. Simplified diagram of an inkjet 3D printer

1.1.2 Directed Energy Deposition

The most well known machine technology that falls under directed energy deposition is laser engineered net shaping (LENS) also known as laser powder forming, direct metal deposition, or laser consolidation. Powder is supplied coaxially around a laser beam through powder inlets and either dropped or sprayed onto the substrate. The laser is focused by one or more focusing lenses onto the substrate and melts the powder as it is deposited. An inert gas shroud is used to shield the melt pool from oxygen gas that could interfere with the solidification of the metal causing poor mechanical properties. The substrate is rastered in the x-y plane by motors to expose each slice and the head is stepped upwards after each layer is finished exposing. Materials such as titanium, stainless steel, and aluminum along with different alloys, composites, and specialty materials have been used in LENS. A diagram of a typical LENS machine is shown in Figure 1.2.

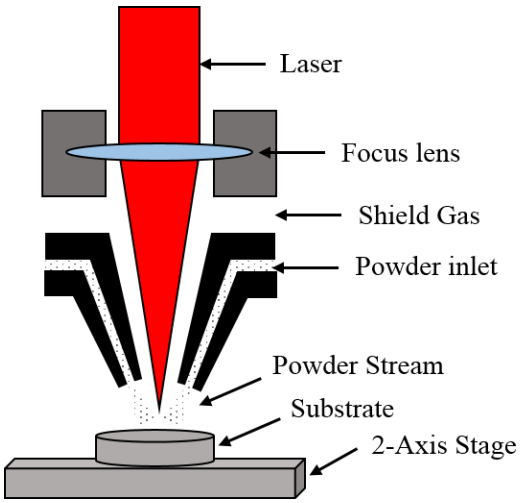

Figure 1.2. Simplified diagram of a laser engineered net shaping (LENS) machine

1.1.3 Material Extrusion

Material extrusion encompasses the additive manufacturing technologies where a plastic filament or metal wire is unwound from a spool and melted to create a part. The

most well-known technology that falls in this category is fused deposition modeling (FDM) which is trademarked by Stratasys Inc. Material extrusion involves the dispense of one or more materials from supply spools, through an extrusion head with heating elements, and out through one or more extrusion nozzles onto a stage. Either the extrusion head or stage can be moved in the x, y, and/or z directions to produce a part. A number of materials have been used with FDM including acrylonitrile butadiene styrene (ABS), along with different blends and composites. A simplified diagram of a typical FDM machine is shown in Figure 1.3.

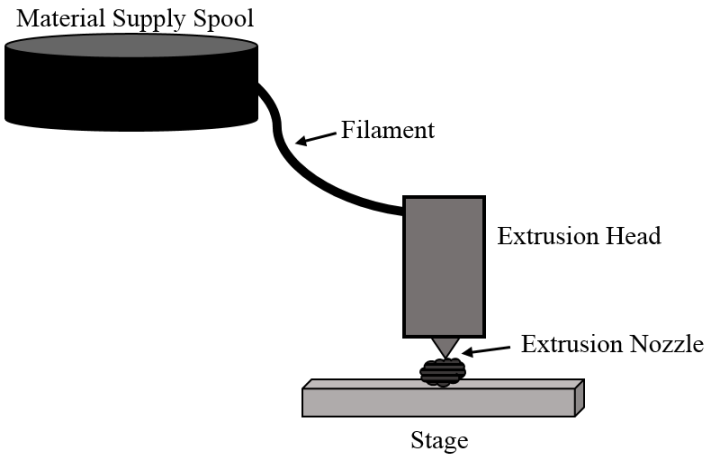

Figure 1.3. Simplified diagram of a fused deposition modeling (FDM) machine

1.1.4 Material Jetting

Material jetting machines utilize inkjet print heads to jet liquid materials onto the build stage. The materials jetted can be melted materials that solidify (e.g. waxes) or photopolymers (e.g. acrylates and epoxies) that are then cured by a UV light source. The UV light source is typically a UV lamp that is located in the print head and shines light through a window located behind the inkjet print heads. Multi-material parts can be made by having multiple build tanks that feed through separate inkjet print heads. A simplified diagram of material jetting machine designed for photopolymers is shown in Figure 1.4.

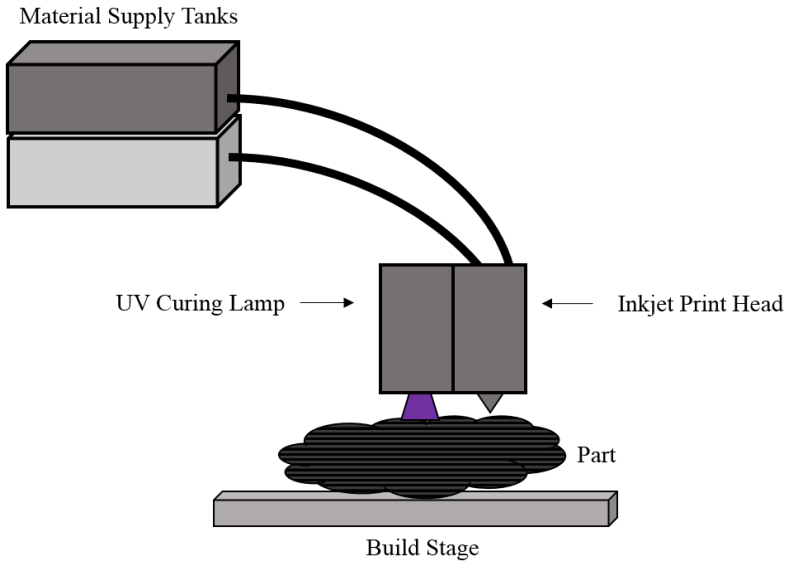

Figure 1.4. Simplified diagram of a photopolymer material jetting machine

1.1.5 Powder Bed Fusion

The category of powder bed fusion technologies encompasses methods such as laser melting (LM) and selective laser sintering (SLS). LM is also referred to as selective laser melting (SLM), and direct metal laser sintering (DMLS). LM involves the use of a laser to selectively melt thin layers of metal powder that are sequentially deposited by a recoater. SLS is similar to LM but utilizes plastic powders instead of metal powders. Extensive support structures are used in LM to prevent warping caused by thermal stresses while SLS typically does not require support structures because plastics have lower melting points and are typically less thermally conductive. A simplified diagram of a LM machine is shown in Figure 1.5.

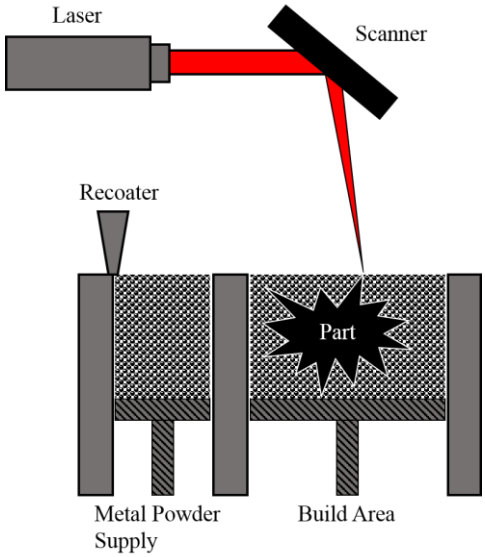

Figure 1.5. Simplified diagram of a laser melting (LM) machine

1.1.6 Sheet Lamination

Sheet lamination refers to additive processes where the starting material is an adhesive-coated laminate such as in laminated object manufacturing (LOM). During sheet lamination, sheets of adhesive coated paper, plastic, or metal laminates are cut to shape with a laser or blade and then layered on top of each other so that they are held together by adhesive. Parts made by sheet lamination are often post-processed by machining to eliminate the stair-stepping effect caused by the sheets. A simplified diagram of a LOM machine is shown in Figure 1.6.

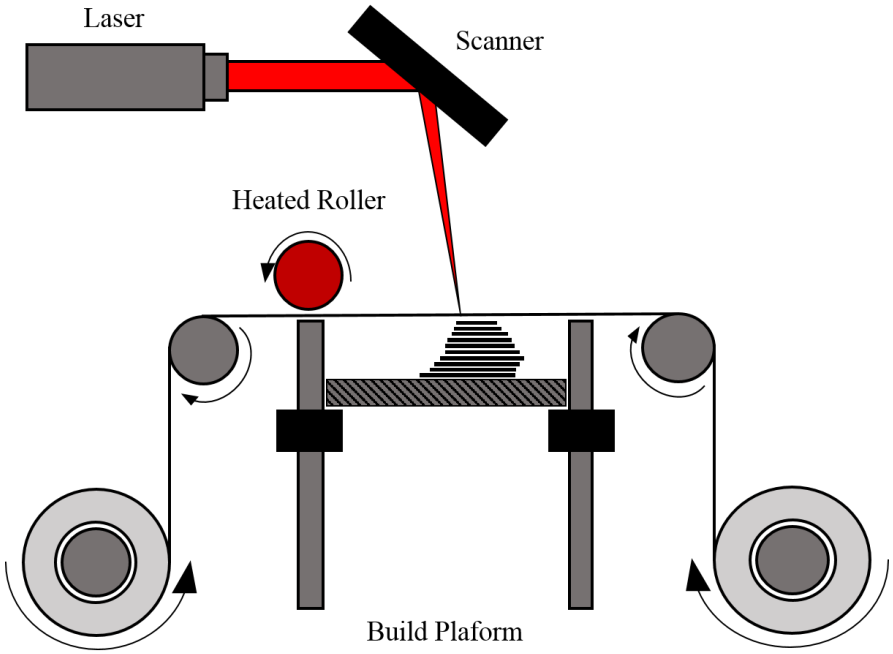

Figure 1.6. Simplified diagram of a laminated object manufacturing (LOM) machine

1.1.7 Vat Photopolymerization

Vat photopolymerization refers to technologies that build parts in a vat of liquid photopolymer by selectively curing it with UV light. Vat photopolymerization can utilize a laser or a lamp as the UV light source to initiate the photopolymerization reaction. Systems with a laser use a scanner to control the trajectory of the laser and raster patterns on the vat in a process called stereolithography (SLA). Other systems that use a UV curing lamp spatially modulate the projection of light by using a series of physical masks or a digital light processing (DLP) device such as a digital micromirror device (DMD). Vat photopolymerization machines can be set up so the exposure can be from above through the air or below through a window. In both cases a build platform moves away from the light source in incremental steps through a vat of liquid photopolymer. A simplified diagram of a SLA machine is in shown in Figure 1.7.

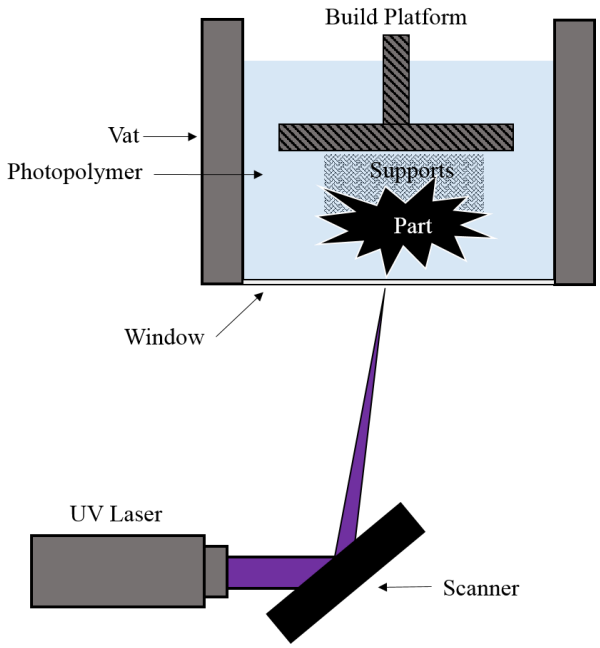

Figure 1.7. Simplified diagram of stereolithography (SLA) machine

1.1.8 Additive Methodologies Investigated

In this work, two promising additive manufacturing techniques are investigated for the manufacture of tissue engineering scaffolds. SLS was selected for bone tissue engineering because SLS has the capability of fabricating bioresorbable thermoplastic scaffolds that are suitably large with reasonable feature resolution. A novel process called large area maskless photopolymerization (LAMP) was selected for soft tissue applications because it is has the capability to process photopolymerizable hydrogels at a high resolution over large length scales in a timely manner.

1.2 Selective Laser Sintering (SLS)

SLS is a laser-based additive manufacturing technique in which an object is built layer-by-layer using a laser, heaters, and powdered starting materials [5]. In SLS, the digital representation of an object is mathematically sliced into a number of thin layers. The object is then created by scanning a laser beam and selectively fusing (melting or

sintering) patterns into layers of powder that are sequentially deposited by a roller. Each patterned layer of powder is also fused to its underlying layer and corresponds to a cross-section of the object as determined from the mathematical slicing operation. A schematic of the SLS process is shown in Figure 1.8.

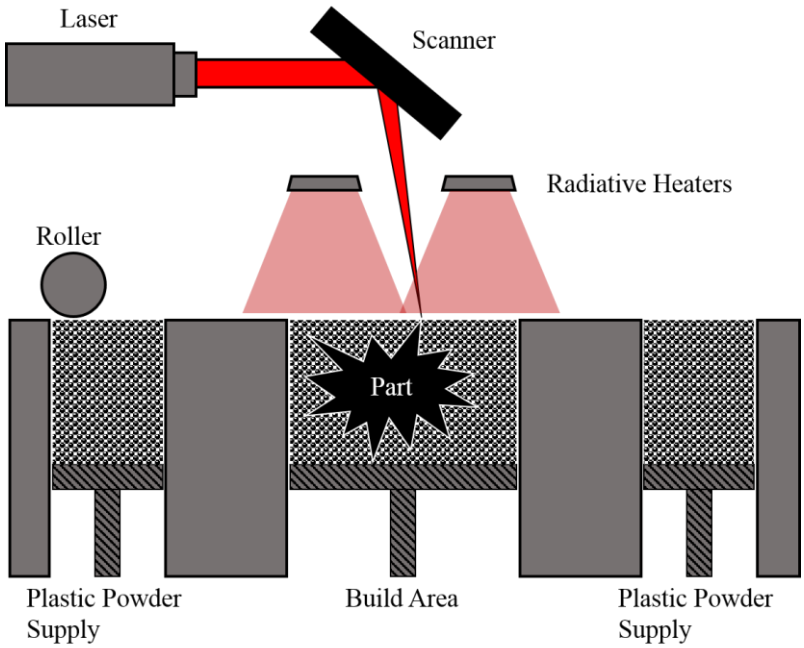

Figure 1.8. Schematic of selective laser sintering process.

In the SLS process, the key controllable processing parameters are: 1) build area temperature, 2) energy density, 3) layer thickness, and 4) recoating speed. The part bed temperature is the temperature of the build area during fabrication of the parts. The part bed temperature is kept slightly below the melting temperature of the powder so that a low energy density from the laser can be used to melt it; however, if the part bed temperature is too high it will cause the powder to clump and not form a uniform layer. The energy density refers to the power per unit area supplied by the laser. The energy density is the most difficult parameter to optimize because there is a very small window for many materials where the energy is high enough to fully melt the powder while not

being so high that it causes the powder to burn. The layer thickness is the height of the deposited powder in each successive layer and it is usually kept as low as possible to give better resolution along the build axis however it is constrained on the lower end by the particle size of the powder. Lastly, the recoating speed determines the rate at which the recoater moves across the build area. The recoating speed is maintained at a sufficient speed so that a uniform layer is deposited while not being so slow that it significantly increases the total time required to complete the build.

SLS allows the fabrication of scaffolds with a high degree of geometric complexity and enables the direct conversion of a scaffold's computer model into its physical realization—allowing patient-specific and tissue-specific reconstruction strategies to be easily developed [6-13]. Medical applications for SLS were first investigated in 1997 by Berry et al. [14] where 3D reconstructions of human bones were used for surgical planning. Scaffolds made of UHMWPE, PLA, Nylon-6, PEEK, PVA and different composites were fabricated by SLS in the early 2000's [15-24]. These scaffolds did not have degradation properties and in some cases did not have mechanical properties that were suitable for bone tissue engineering. Williams et al. [25] first used PCL for an SLS processed scaffold in 2005 and showed promising results in an animal model. Since then PCL and PCL composites have been used extensively in additive manufacturing for bone tissue engineering. An example of a PCL scaffold designed for a human condyle is shown in Figure 1.9.

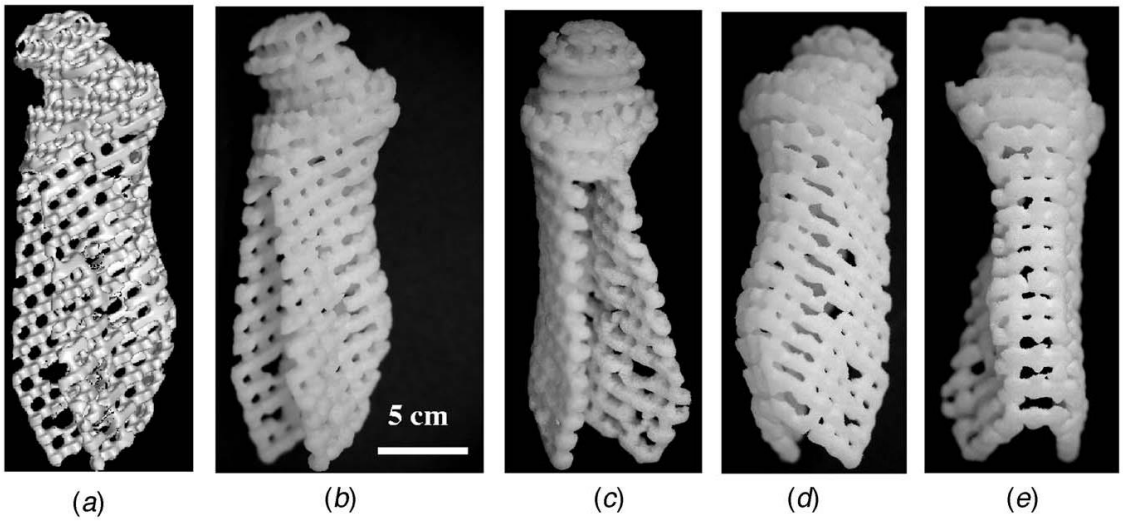

Figure 1.9. (a) 3D model of a human condyle scaffold, (b) - (e) PCL scaffolds fabricated by SLS [26].

Powder based additive manufacturing methods such as SLS are desirable for tissue engineering because they do not require the use of strong organic solvents that may be difficult to remove once the part is built. Also SLS has been shown to be able to produce scaffolds with tailorable degradation properties that can last in the body up to 2 years and be completely removed after 3 years leaving only the regenerated tissue in the implant site [25, 27].

1.3 Large Area Maskless Photopolymerization (LAMP)

LAMP is an additive manufacturing technique similar to other DLP based systems in that it projects a bitmap image from a DMD onto a photocurable resin. LAMP, however, has a very high resolution and the capability of large-area curing to build large parts or arrays of small parts in a single build.

The optical imaging system, shown in Figure 1.10, consists of an UV lamp, condenser, reflection mirror, DMD, and projection lens. The DMD modulates over 1.3 million UV beams by individually rotating the micro-mirrors by ±10-12° to an on or off state as dictated by a computer controller. Large objects can be built quickly with ~20 µm

feature resolution and without post-processing. The imaging system is capable of projecting a 1500 dpi image at energy densities up to 1.5 $W \cdot cm^{-2}$.

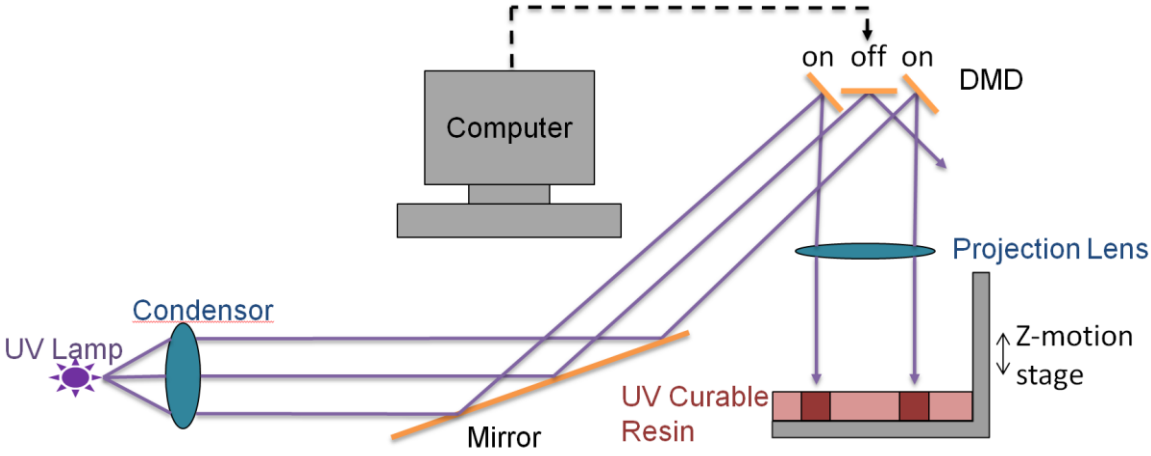

Figure 1.10. A simplified schematic of the LAMP setup showing how the DMD works.

The LAMP process starts with a CAD model of the desired part that is then sliced into discrete layers. The cross-sections resulting from the slicing operation are then converted to bitmap images and stored in a computer controller. LAMP uses an overhead gantry-style optical imaging system to smoothly raster a projected bitmap image across the entire build area. The material build platform has a z-stage where the photocurable resin is deposited in 50 – 100 µm layers. A recoating mechanism applies a uniform coating of the photocurable resin as the z-stage steps down after each layer is exposed.

There are three key, controllable processing parameters in the LAMP process: 1) energy density, 2) layer thickness, and 3) recoating speed. In this work, the material composition of the photocurable resin consists of a hydrogel and photoinitiator and possibly a UV absorber. UV radiation from the optical imaging system is primarily absorbed by the photoinitiator, and the cure depth is directly controlled by the photoinitiator concentration. The UV absorber attenuates light as it passes through the

resin and is used to give a sharp cure gradient. Together, photoinitiator and UV absorber concentrations affect the cure depth, amount of monomer conversion, and over-curing.

Optical scattering occurs as photons from the optical imaging system penetrate the resin. At the surface of the resin, the bitmap projected from the DMD chip will have sharp features, but further inside the resin, the image is blurred because the resin has a strong filtering affect. If this filtering affect is too strong then successive layers do not match up correctly and monomer conversion rates are low. The goal of a layered photopolymerization process is to have as little scattering as possible to give good feature resolution and high monomer conversion to give good mechanical properties.

Photopolymerization processes have been used in the past to process hydrogels for tissue engineering applications because they can allow for encapsulation of cells during processing and can build complex microarchitectured constructs. Typically a macromolecular hydrogel precursor is used instead of a monomer because of the high cytotoxicity of most monomers [28]. Polyethylene glycol (PEG) acrylate derivatives, PEG methacrylate derivatives, polyvinyl alcohol (PVA) derivatives, and hyaluronic acid derivatives have all been studied as photocrosslinkable hydrogels for tissue engineering [28].

Additive manufacturing techniques such as stereolithography (SLA) [29], two-photon photopolymerization (2PP) [30], and digital light projection (DLP) [31] have been investigated for processing 3D microarchitectured hydrogels. SLA and 2PP are disadvantaged when dealing with hydrogels loaded with cells because large constructs would require prohibitively long build times to complete. While DLP systems have fast build times, they are limited to small build windows that are not capable of building large

constructs. Because LAMP uses a DMD as a spatial light modulator that is carried on an overhead gantry system, the photopolymer can be exposed much more quickly than raster scanning line-by-line as in SLA and over a much larger area than with other DLP systems. This makes LAMP highly scalable technology while minimizing any loss of feature resolution.

1.4 Problem Statement

The fabrication of scaffolds for bone and cartilage constructs is extremely difficult due to requirements on transport and mechanical stability as well as the desire for good scaffold-cellular interactions and biodegradability of the scaffold on a correct time scale. Poor nutrient transport to the interior of the tissue constructs can result in necrosis of the embedded cells. If a scaffold undergoes mechanical failure in load bearing bone or cartilage it is generally catastrophic and would cause severe complications *in vivo*.

Several approaches have been attempted to improve the influx of nutrients and efflux of wastes from the bulk of the construct by creating porosity in the scaffolds, however the porosity is typically random and results in a substantial loss of effective mechanical strength. A microfluidic network embedded within the bulk of the construct may be able to meet the transport requirements of the interior cells but conventional manufacturing methods for scaffolds are—in most cases—limited to simple geometries and large feature sizes. To overcome this constraint, it is proposed that advanced additive manufacturing technologies such as SLS and LAMP be utilized.

1.5 Significance

Additive manufacturing technologies are highly desirable for medical applications because of the simple fact that one size does not fit all. Every surgery site is unique and

in many cases an exact fit of the implant is required. In regenerative medicine a mismatch between a tissue construct and a defect can result in catastrophic failure of the healing therapy. Designing and fabricating different sizes and shapes of implants for everyone from infant to adult and having them on hand for use is impossible when an exact fit is needed. However, it is feasible to use medical imaging techniques to determine the desirable size and shape of the implant and CAD to make a model that is manufacturable which can then be fabricated by additive manufacturing. In situations where very few parts are built, additive manufacturing is orders of magnitude faster and more cost efficient than conventional manufacturing techniques.

SLS and LAMP are cost-efficient, scalable techniques for the fabrication of tissue engineering scaffolds with computationally designed microarchitectures and customizable external geometries. A technological advancement in the fabrication of scaffolds with designed microarchitectures out of commercially available materials has broad implications in the area of tissue engineering beyond the present applications. It is not difficult to imagine extension of these techniques to tissues of multiple cell types including vascularized tissues, tumorogenesis models, and interfacial tissue engineering (bone/tendon, bone/ligament, bone cartilage) as well as investigational drug and stem cell differentiation studies. The ability to expand the thickness of constructs produced in a high-throughput manner also opens the possibility of these techniques being an enabling technology for the fulfillment of cost-efficient, readily available tissue engineered substitutes for clinical implementation at hospitals around the world.

1.6 Outline

This dissertation is divided into five chapters. Chapter 1 is the introduction covering the backgrounds of SLS and LAMP, the current problems in scaffold fabrication for tissue engineering, and the significance of using additive manufacturing for tissue engineering.

Chapter 2 gives a background of the technology of SLS and LAMP with special attention on the physical processes of the systems.

Chapter 3 describes the experimental methodology for material preparation, manufacturing, process parameter optimization, and characterization.

Chapter 4 discusses the results from experimentation and computational modeling with special attention focusing on material property characterization for SLS and feasibility studies for LAMP.

Chapter 5 concludes this work and revisits the objectives outlined in the problem statement. Future work is also discussed.

CHAPTER 2

BACKGROUND

This chapter provides an overview of the technology behind both SLS and LAMP and explains the experimental setup. The SLS system used is a Sinterstation® 2000 SLS machine (3D Systems Inc., Valencia, CA), and the LAMP system is a custom built prototype from Dr. Suman Das's lab group. Both systems give the user control over the processing parameters necessary for investigating different material systems whereas many other commercial systems lock processing settings making it impossible to investigate new material systems.

2.1 Laser Sintering of Thermoplastics

The process of sintering in thermoplastic powders is driven by a reduction in surface tension that was first described by Frenkel et al [32]. Frenkel's model characterizes the growth of the inner neck radius with time as

$$\left(\frac{x}{a}\right)^2 = \frac{3}{2\pi}\frac{\sigma}{a\eta}t \tag{2.1.1}$$

where x is the neck radius between particles, a is the radius of the particle, σ is the surface tension, η is the viscosity, and t is time. Based on this model, polymers that have high surface tension, low viscosity, and small particle size should have the fastest sintering rates. Semicrystalline polymers tend to have a steep drop in viscosity when melting resulting in a fast sintering rate and near-complete particle coalescence.

In SLS having a fast sintering rate generally results in better physical properties for a material system. Powdered materials are very porous and if the melted material is not able to flow quickly and coalesce during the short period in which it is heated by the

laser then the processed part will have a high degree of manufacturing induced porosity. Manufacturing induced porosity is porosity that occurs in the designed solid regions whereas designed porosity occurs on a much larger scale and comes from the desired geometry having a porous architecture. Pore sizes from incomplete particle coalescence are typically smaller than the average particulate size (<100 μm) while designed porosity is typically larger than the beam diameter and particulate size (>500 μm).

Fabricating parts that are near fully dense by SLS requires careful material selection and optimization of the processing parameters. A part can be considered near fully dense if its manufacturing induced porosity is less than 5% or it is more than 95% dense as measured by pycnometry or image analysis. High manufacturing induced porosity has deleterious effects on mechanical properties such as the elastic modulus and yield strength. In the case of tissue engineering, mechanical failure of a polymer scaffold can cause catastrophic failure of the entire tissue construct negatively affecting the patient.

The key processing variable to be optimized for SLS is the energy density ($\boldsymbol{U}$).

$$\boldsymbol{U = \frac{P}{vd}} \tag{2.1.2}$$

The energy density is equal to the laser power ($\boldsymbol{P}$) divided by the scan speed ($\boldsymbol{v}$) and scan spacing ($\boldsymbol{d}$). It is the energy input that overcomes the latent heat of fusion for the material resulting in a brief period where part of the material is in a liquid state and particles can coalesce. While most of the energy is provided by the radiant heaters which heat the entire powder bed close to the melting temperature, the energy input from the laser is crucial in determining how long the material stays above the melting temperature and how far past the melting temperature it gets.

2.2 Description of SLS Process

The SLS machine consists of several components that act together to take a digital representation of an object and produce a physical object. An STL (Standard Tessellation Language) file is the standard file type used for SLS machines. STL files only contain data about the surface geometry of a 3D object; they do not contain the additional information found in other CAD models such as color, texture, etc. STL files contain the unit normal and vertices of triangles in Cartesian coordinates (x,y,z). The number of triangles in each file differs based on the complexity of the object. More complex objects require more triangles to accurately represent them.

A typical build contains many different or repeated STL files that are arranged in the build area so that they do not overlap. The parts are typically arranged in a 2D grid on the x and y axes with their short axis in the z-axis because tall builds take longer to complete. Once the objects are arranged, they are sliced based on the layer thickness (~100 μm) and the path of the laser beam is planned. The laser typically scans in the x direction and can step either up or down in the y direction. Galvanometric scanning mirrors control the positioning of the laser beam and a lens focuses the laser to a 450 μm spot size on the powder bed. The order that the parts are scanned is also be rotated so that the deposited powder on top of each part does not get more or less exposure to the radiant heaters. A schematic of the subsystems in a conventional SLS machine is shown in Figure 2.1.

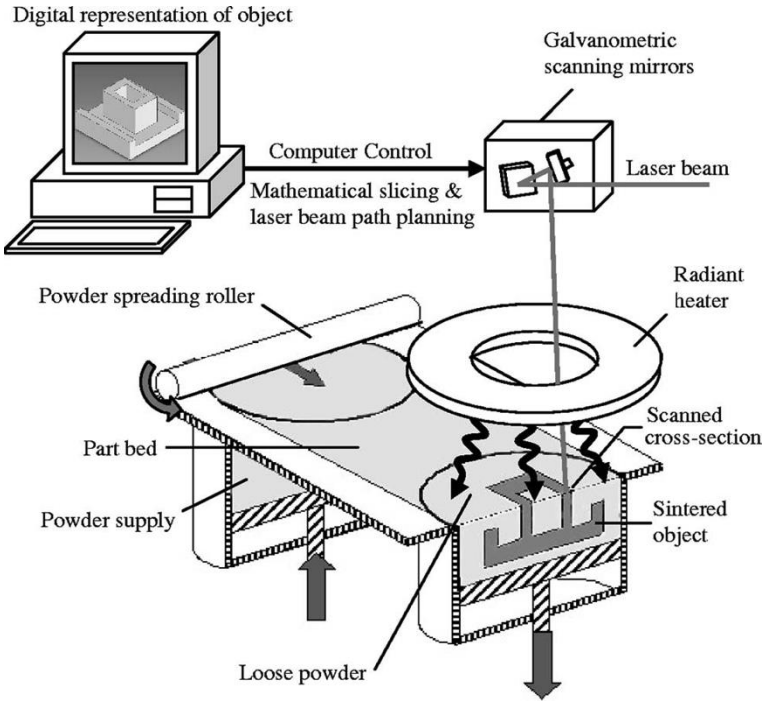

Figure 2.1. Schematic of SLS process [26].

2.3 Description of LAMP Process

LAMP is similar to many other additive manufacturing processes in that it starts with one or more STL files representing the parts to be built. A slicing software developed by Anirudh Rudraraju [33] is used to mathematically slice the STL files and export stacks of 1-bit TIFF images. The images are compressed by CCITT Group 4 compression, a lossless method originally developed for digital fax machines. Each image corresponds to a single layer of the build typically 50 – 100 μm in thickness.

A support structure is automatically generated to surround the desired parts and protect them while they are fabricated. This support structure is different from support structures that are created for parts built in vat photopolymerization systems because the support structure in LAMP completely surrounds the parts and acts as the retaining wall for the

uncured material. In the case of LAMP, the retaining wall that replaces the vat is built along with the parts and support structure as shown in Figure 2.2.

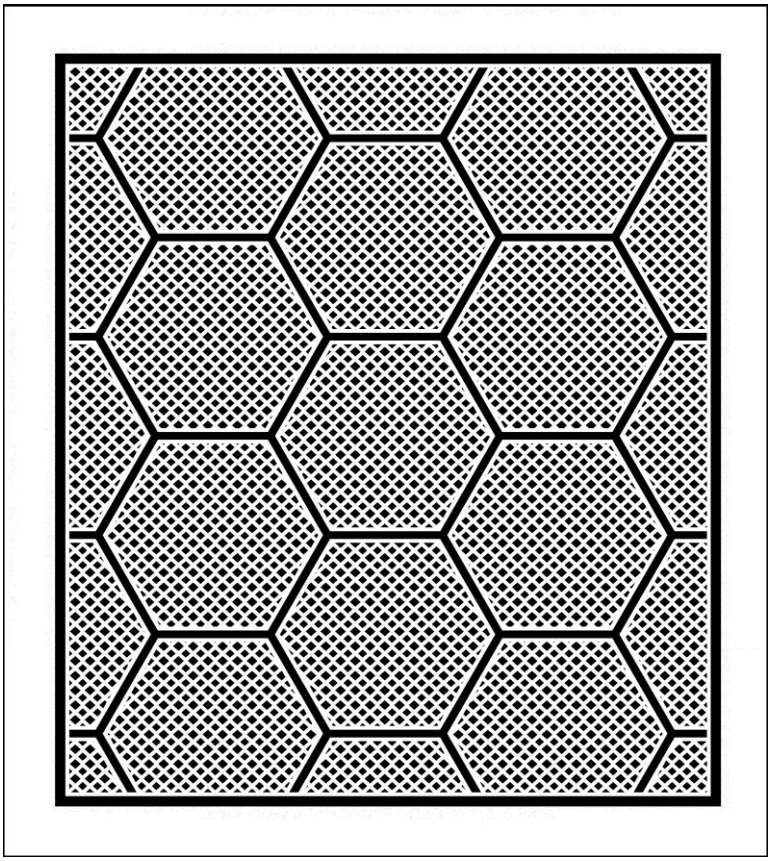

Figure 2.2. Design of the support structure and retaining wall for LAMP (101 x 113 mm)

The exposure head, which is mounted a high precision (1 μm) motion system, smoothly moves in a serpentine pattern across the entire build area. Using this method an area much larger than the DMD in the exposure head can be exposed. After the exposure is finished the build stage is moved down one layer by a stepper motor. Another stepper motor controls the recoating arm that swipes left while a peristaltic pump dispenses resin through the bottom of the recoater. After the recoater reaches the end of the sweep it reverses direction and returns to the right side of the build window while skimming off any excess material that was deposited. A computer controller then signals the exposure head to run the next exposure. Excess material deposited by the recoater is reclaimed

from a drain located under the build stage and is circulated back into the supply hopper by peristaltic pumps. A detailed schematic of the exposure head and material recoating system is shown in Figure 2.3.

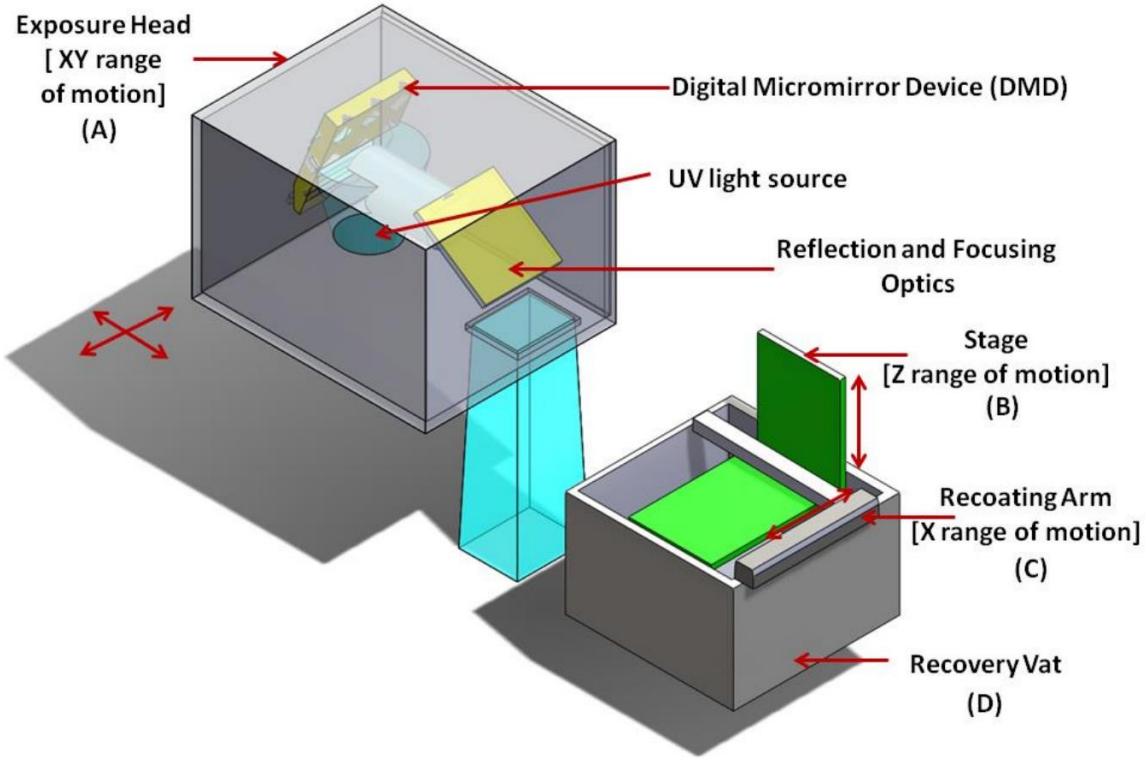

Figure 2.3. Schematic of LAMP setup detailing exposure head and material stage.

2.4 Dynamic Mask Photopolymerization of Hydrogels

LAMP is an attractive technology because the exposure area is much larger than SLA allowing for much faster build times while at the same time feature resolution is not sacrificed. In order to reach suitable energies densities for photopolymerization reactions to take place on a desirable time scale (< 1s), there must be a high power energy input from the light source. In the case of LAMP, the energy input comes from a high-pressure mercury arc lamp. The emission spectrum of the mercury arc lamp is shown in Figure 2.4. There are three distinct peaks that are in order from largest to smallest at 438 nm,

405 nm, and 365 nm. The peak at 438 nm corresponds to visible blue light and is not suitable for photopolymerization because it is not in the ultraviolet spectrum. The peak at 405 nm is on the upper end of what is considered UVA radiation (400-315 nm) while the peak at 365 nm in the range for UVA.

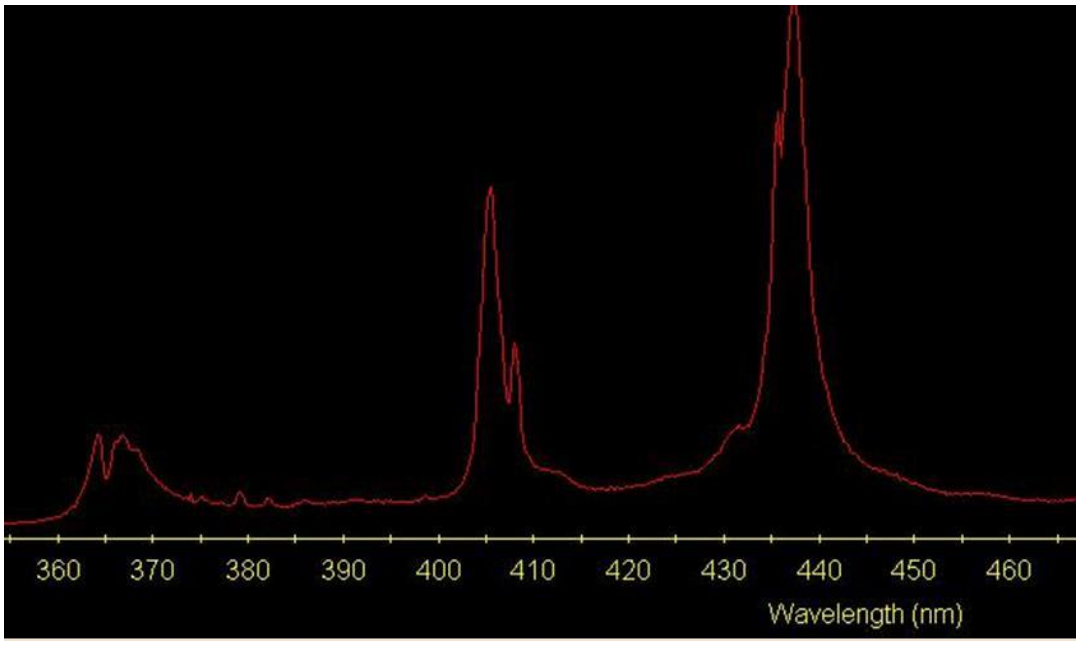

Figure 2.4. Spectrum of high pressure mercury light source used in LAMP [34].

2.4.1 Photopolymerization Kinetics

There are three stages in chain growth polymerization: initiation, propagation, and termination. There are multiple ways to initiate chain growth polymerization; however, in this work free radical polymerization is used for initiation. In radical photopolymerization photons homolytically cleave a bond in an initiator producing two radical species. In LAMP, the photons that provide the energy to cleave the initiator are supplied by the mercury arc lamp and dynamically modulated by the DMD to control which regions of the material system generate free radicals and therefore undergo polymerization.

The following equations can be used to describe the reaction rates for initiation (Equation 2.4.1.1), propagation (Equation 2.4.1.2), and termination (Equation 2.4.1.3).

$$v_i = \frac{d[M\cdot]}{dt} = 2k_d f[I] \tag{2.4.1.1}$$

$$v_p = k_p[M][M\cdot] \tag{2.4.1.2}$$

$$v_t = \frac{d[M\cdot]}{dt} = 2k_t[M\cdot]^2 \tag{2.4.1.3}$$

The efficiency of the initiator is *f*, and the constants for initiator dissociation, chain propagation and termination are k_d, k_p, and k_t respectively. [I], [M] and [M•] is the concentration of the initiator, monomer and the active growing chain. The rate of initiation can depend on the rate that photons are introduced into the material system.

Under steady state assumptions the concentration of the active growing chain can be expressed in terms of the known species (Equation 2.4.1.4).

$$[M\cdot] = \left(\frac{k_d[I]f}{k_t}\right)^{1/2} \tag{2.4.1.4}$$

The dynamic chain length, ℓ, is a measure of the average chain length of a reacting polymer chain and is a function of propagation rate and initiation rate (Equation 2.4.1.5) when chain transfer is not considered.

$$\ell = \frac{v_p}{v_i} = \frac{k_p[M][M\cdot]}{2k_d f[I]} = \frac{k_p[M]}{2(k_t k_d f[I])^{1/2}} \tag{2.4.1.5}$$

Lastly, the degree of polymerization, P_n, can be calculated as a function of dynamic chain length and the value δ which is 0 when chain termination is caused by combination of two chains and 1 when chain termination is caused by disproportionation (the transfer

of hydrogen from one chain to another). In a situation where combination and disproportionation both occur $\boldsymbol{\delta}$ will be somewhere between 0 and 1.

$$\boldsymbol{P_n = \frac{2}{1+\delta}\ell} \tag{2.4.1.6}$$

2.4.2 Light Sensitivity of Material System

The Beer-Lambert Law describes the attenuation of light as it passes through a material. It states that there is logarithmic relationship between the transmission ($\boldsymbol{T}$) of light and the product of attenuation coefficient ($\boldsymbol{\Sigma}$) and path length ($\boldsymbol{\ell}$).

$$\boldsymbol{T = \frac{I}{I_0} = e^{-\Sigma \ell}} \tag{2.4.2.1}$$

The transmission of light is described by the intensity after passage ($\boldsymbol{I}$) divided by the initial intensity ($\boldsymbol{I_0}$). The attenuation coefficient is the summation of the absorptivity multiplied by the concentration for all the absorbing species. Equation 2.4.2.1 can be rewritten in terms of energy ($\boldsymbol{E}$) as a function of depth ($\mathbf{z}$) where $\boldsymbol{E_0}$ is the initial energy dose.

$$\boldsymbol{E(z) = E_0 e^{-zD_p}} \tag{2.4.2.2}$$

The resin sensitivity ($\boldsymbol{D_p}$) is the inverse of the attenuation coefficient and describes the depth of penetration of the light in a photocuring process [35]. An estimation of the cure depth ($\boldsymbol{C_d}$) can be determined when the critical energy dose ($\boldsymbol{E_c}$) is taken into account.

$$\boldsymbol{C_d = D_p \ln\left(\frac{E_0}{E_c}\right)} \tag{2.4.2.3}$$

The critical energy dose is the minimum energy dose at which gelation starts to occur for the material system. Equation 2.4.2.3 is used to determine the resin sensitivity and critical

energy dose of a material system by regression of measured cure depths at varied energy doses. A typical cure depth plot is shown in Figure 2.5.

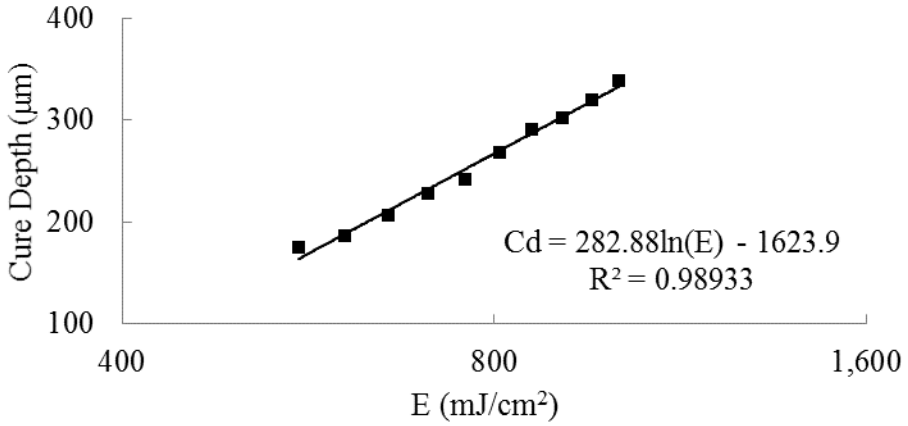

Figure 2.5. Typical cure depth plot for a polyethylene glycol diacrylate material system.

The slope of the logarithmic regression is $\boldsymbol{D_p}$. $\boldsymbol{E_c}$ can be determined from the y-intercept ($\boldsymbol{b}$) of the logarithmic regression as shown in Equation 2.4.2.4.

$$\boldsymbol{E_c = e^{-\frac{b}{D_p}}} \tag{2.4.2.4}$$

In the above example $\boldsymbol{E_c}$would be 311.21 mJ·cm^{-2}.

CHAPTER 3

EXPERIMENTAL METHODOLOGY

This chapter gives an overview of the materials and methods used for material preparation, fabrication, processing optimization, and characterization. The materials and methods for SLS and LAMP differ greatly as SLS uses thermoplastic powders and LAMP uses photocurable resins. A variety of compositions and processing parameters were investigated for both processes and a design of experiments approach was taken to optimize processing parameters. Detailed computational modeling and experimental mechanical characterization were conducted on the SLS processed samples to compare with conventional manufacturing techniques, e.g. injection molding. The application for SLS processed parts in bone tissue engineering places requirements on the porosity and mechanical strength of the scaffolds. Characterization of the samples manufactured by LAMP was conducted based on microarchitecture as hydrogels are not typically used in load bearing applications.

3.1 Materials Used for SLS

Polycaprolactone powder was purchased from Solvay Caprolactones (Warrington, UK) under the brand name CAPA®6501 (Solvay Caprolactones was acquired by Perstorp in 2008). PCL is a semicrystalline (56%) aliphatic thermoplastic with molecular formula $(C_6H_{10}O_2)_n$ as shown in Figure 3.1. PCL has a melting temperature (T_m) of 58–60 °C and a glass transition temperature (T_g) around -60 °C [36]. PCL has a molecular weight of M_n = 91,900 before SLS processing and M_n = 73,000 after processing. Mechanical sieving showed an average particle size of 90 μm for the powder according to ISO 2591-1 standards and 98% of all particles were less than 125 μm [37].

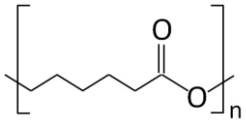

Figure 3.1. Repeating unit of poly(caprolactone) (PCL).

Hydroxyapatite (HA) powder was used as an inorganic bioactive filler to make composite scaffolds. HA has molecular formula $Ca_{10}(PO_4)_6(OH)_2$ and a molecular weight of M_n = 1004. Hydroxyapatite is a key component in bone where it exists in a carbonated form with lower crystallinity. The appearance of HA is a white powder with average particle size of 45 µm. The crystallinity characteristics of HA (Figure 3.2) were assessed by X-ray diffraction (XRD) in a X'Pert powder diffractometer (PANanalytical BV, Almelo, the Netherlands) using monochromatic, filtered Cu Ka (k = 1.5405 Å) radiation.

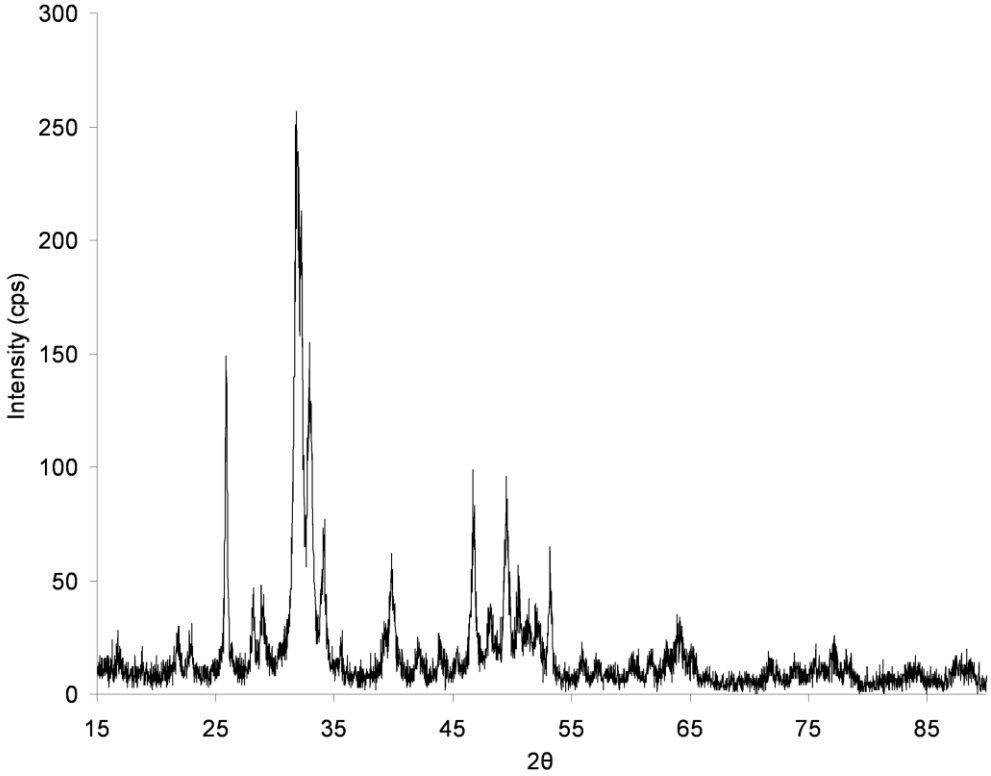

Figure 3.2. X-ray diffraction pattern for hydroxyapatite powder [38].

3.2 Methodology for SLS Fabrication

Powders were prepared for SLS by dry mixing different mixes of PCL and HA in a rotary tumbler (784 AVM, US Stoneware, OH) for 24 hours. This mixing protocol has been shown to provide dispersion for other composite material systems [38-42]. Powders were then mechanically sieved using a 150 μm mesh. Neat PCL and PCL:HA composite powders were processed in a commercial Sinterstation® 2000 SLS machine (3D Systems Inc., Valencia, CA). The SLS machine used has a CO_2 continuous wave laser (λ = 10.6 μm) that can reach a maximum power of 10 W at a spot size of 450 μm.

The SLS machine has a piston heater that is below the part bed as well as radiant heaters located between the laser window and the powder bed. The piston heater is typically used when a high melting point powder is used so that excessive heat loss does not occur through the bottom of the powder. In this case, the low melting temperature of PCL did not necessitate the use of the piston heater. The radiant heaters were set to heat the part bed to a temperature of 46 °C for neat PCL and 50 °C for the PCL:HA composites. An infrared sensor directed at the center of the part bed powder surface controls the output of the radiant heater using PI control. Radiant heaters are also located above each of the powder supply areas; these areas were set to a temperature of 25 °C and controlled by a thermocouple submerged in the powder.

A motorized steel roller is used to sweep the powder left and right to deposit uniform 100 μm layers. Hydraulic pistons control the positions of the part bed and powder bins. At the start of the build the roller is located to the right of the right powder supply bin. The sequence of events that occurs to complete a full cycle is as follows

1. Part bed moves down 100 μm.

2. Right powder supply bin moves up.
3. Roller moves to the left of the left powder supply bin.
4. Laser is rastered across the part bed in a pattern that corresponds the current build height.
5. Part bed moves down 100 μm.
6. Left powder supply bin moves up.
7. Roller moves to the right of the right powder supply bin.
8. Laser scans the next slice of the build.

The powder supply pistons are manually set to move the minimum distance required so that the roller is not starved of powder as it traverses the build area. The axes of the SLS machine are defined with the z-axis parallel to the motion of pistons, x-axis parallel to the motion of the roller, and y-axis orthogonal to both.

The powers of lasers in commercial SLS machines are known to change over time. Because of this a power calibration is conducted at regular intervals to estimate the intensity of the laser that reaches the powder. A small power meter is placed 150 mm above the part bed where the beam diameter is roughly 25 mm in diameter. The machine input laser power is then changed from 0 to 10 W in 1 W increments and the corresponding output is measured by the power meter as seen in Figure 3.3.

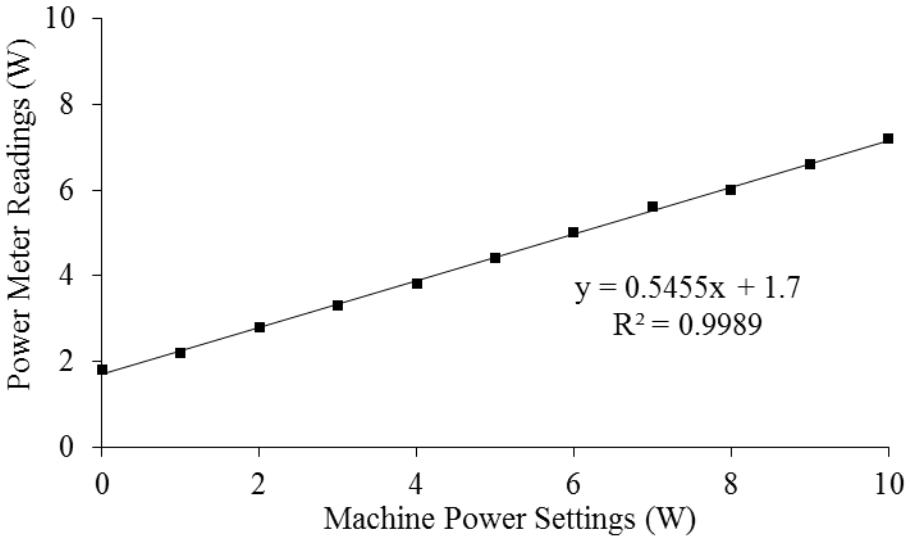

Figure 3.3. Calibration curve for the power of the CO_2 laser in the SLS machine.

In this text the measured laser power as determined by the power meter is reported whereas previously [37, 43] the machine setting was reported.

The optimal SLS processing parameters were determined from a design of experiments (DOE) approach as described by Partee et al. [26]. Briefly, a two-level DOE with 5 processing parameters (2^5=32 unique test conditions) that were laser power, scan speed, scan spacing, part bed temperature, and roller delay. The quality metric used was a weighted average of the qualitative ease of part breakout, degree of dimensional accuracy as measured by calipers, and part density as measured by image analysis. The processing parameters that were observed to have the largest effect were laser power, scan spacing, part bed temperature, and scan speed. The roller speed has been omitted because it was not observed to have a significant effect on the quality of the parts. The resulting optimal processing parameters based on that DOE and the calculated energy density are given in Table 3.1.

Table 3.1. Optimal SLS processing parameters and resulting energy density for neat PCL [26].

Processing Parameter	Value
Part Bed Temperature (°C)	46
Laser Power (W)	3.9
Scan Speed ($mm \cdot s^{-1}$)	1079.5
Scan Spacing (μm)	152.4
Energy Density ($J \cdot cm^{-2}$)	2.37

After the SLS processing of neat PCL was optimized a similar process was conducted for optimizing the SLS processing parameters of PCL:HA composites. However, in this case the scan spacing and roller delay were kept constant so that only the laser power, scan speed, and part bed temperature were varied.

3.3 Characterization of SLS Processed Specimens

3.3.1 Microstructural Characterization

One test specimen from each geometry type was scanned using a MS8X-130 Enhanced Vision Systems micro-computed tomography (μ-CT) machine (GE Medical Systems, Toronto, Canada) at a voxel resolution of 28.1μm. GEMS Microview software (GE Medical Systems, Toronto, Canada) was then used to determine the total (designed) porosity and the level of manufacturing induced porosity by selecting a region of interest (ROI) that encompassed the entire scaffold and then segmenting the processed PCL from air using the same procedure described previously [25].

3.3.2 Density Characterization

Optical microscopy and image analysis techniques were used to characterize the manufacturing-induced porosity of the SLS fabricated 100:0, 90:10, 80:20, and 70:30 PCL:HA parts. After fabrication, solid D638 specimens were cleaved parallel to the build direction. The resulting surfaces were then fully coated with a black wax and subsequently wiped with a cloth until only the wax in the pores remained. Photomicrographs were then taken of each cleaved surface near the center and periphery of the parts using a Leica optical microscope with a 5x objective. The photomicrographs were then analyzed using ImageJ software [44] to determine their void area fraction. The RGB photomicrographs were converted to grayscale and then to binary using a threshold. The histograms of the grayscale images were always bimodal so automatic thresholding based on histogram shape correctly segmented the voids.

3.3.3 Mechanical Characterization

Mechanical test specimen CAD files were created in SOLIDWORKS® (Dassault Systèmes, Vélizy-Villacoublay, France). A solid cylinder with a height of 25 mm and diameter of 12.5 mm was created according to ASTM-D695 Type 2a cylindrical geometry standards. A solid tensile specimen with inner length 57 mm, width 13 mm, and thickness 3.2 mm was created according to ASTM-D638 Type 3 standards. A network of 2 x 2 mm square cross-section channels spaced 0.7 mm apart were extruded as cuts in the z, x-y, and x,y,z directions to create scaffolds having 1, 2, and 3 dimensional porous architectures as seen in Figure 3.4. The loading directions for the mechanical test specimens are also indicated.

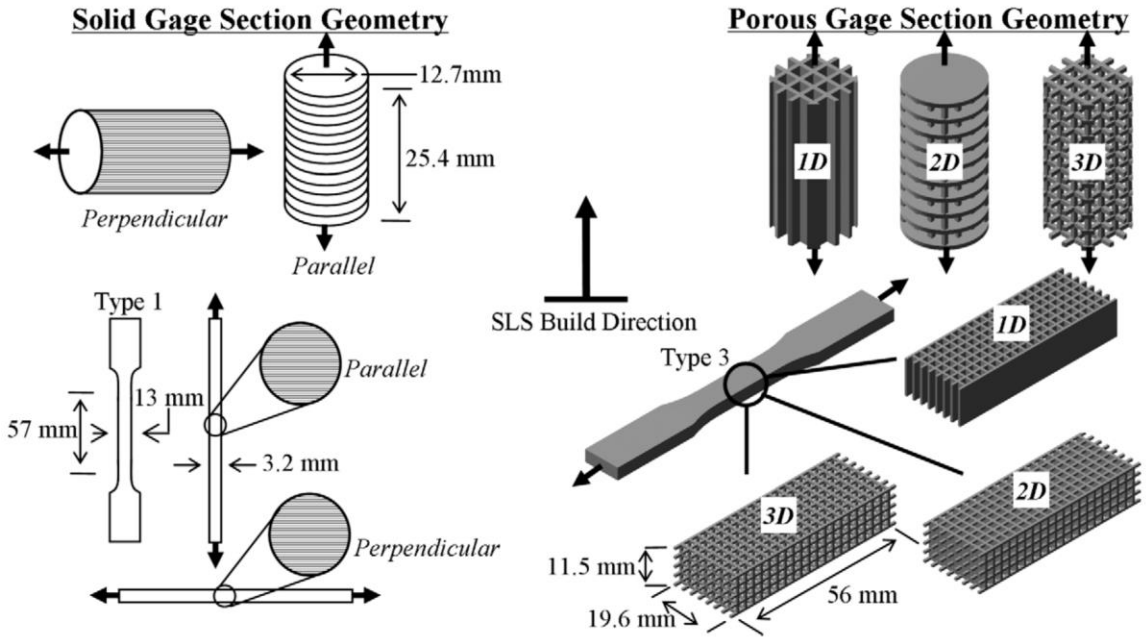

Figure 3.4. Mechanical test specimen geometries, build orientations, and loading directions [37].

It should be noted that the tensile bars were enlarged in order to incorporate a sufficient number of channels in the x-y plane. The solid and porous tensile specimens had the same length but the porous specimens were 1.5x wider and 3.5x thicker as depicted in Figure 3.4. It was not necessary to change the dimensions of the solid compressive specimens when adding the porous channels. The scaffolds with 1D, 2D, and 3D porosities were designed to have increasing levels of porosity. The designed porosities for the tensile and compressive specimens are given in Table 3.2.

Table 3.2. Designed porosities for 1D, 2D, and 3D porous tensile and compressive mechanical test specimens.

Pore Architecture	Porosity (%)	
	Tensile	Compressive
1D	56.9	51.1
2D	67.4	68.5
3D	83.3	80.9

Both tensile and compressive mechanical test specimens were fabricated in neat PCL; however, only compressive mechanical test specimens were fabricated in the PCL:HA composites because the size of the tensile specimens required a very large amount of material. The tensile specimens are referred to as D638-solid, D638-1D, D638-2D, and D638-3D for solid, 1D porous, 2D porous, and 3D porous geometries, respectively. Similarly, the compressive specimens are referred to as D695-solid, D695-1D, D695-2D, and D695-3D. Also, the different material compositions of PCL and PCL:HA composites are referred to as 100:0 for neat PCL. 90:10 for 10% volume loading of HA, 80:20 for 20% volume loading of HA, and 70:30 for 30% volume loading of HA.

Mechanical testing was conducted on SLS processed neat PCL specimens both parallel and perpendicular to the SLS build direction (i.e. across and along direction of layer stacking) while testing was performed only in the parallel direction for PCL:HA specimens. Tensile specimens were tested using a displacement controlled Instron 4206 tensile testing machine (Instron Corp., Canton, MA, USA) at a displacement rate of 50 $mm \cdot min^{-1}$. The specimens were loaded until failure unless the maximum crosshead travel was reached (433 mm). Compressive specimens were mechanically tested using a MTS Alliance RT30 test frame (MTS Systems Corp., Eden Prairie, MN, USA). Specimens were compressed to 50% strain between two steel plates at a rate of 1 $mm \cdot min^{-1}$ after an initial preload of 6.7 N was applied. The tensile and compressive properties were calculated based on the effective cross-sectional area of the test specimens neglecting the porous channels.

3.4 Microstructural Modeling of SLS Processed Parts

Computational modeling of the solid and porous D695 and D638 mechanical test geometries was conducted using MATLAB (MathWorks, Natick, MA, USA) and COMSOL Multiphysics (COMSOL Group, Stockholm, Sweden). In order to analyze the effect that varying HA loading had on the effective mechanical properties of the scaffolds a three-stage process based on first principles modeling was used (Figure 3.5) [43]. The distribution of HA particles in the sintered PCL matrix was modeled as random packing of spheres. The location data from the packing model was then used to build a micromechanical finite element model in order to determine the bulk mechanical properties of the composite. The effective mechanical properties of the full-sized scaffolds were then calculated based on a macroscale finite element analysis of the scaffold geometry.

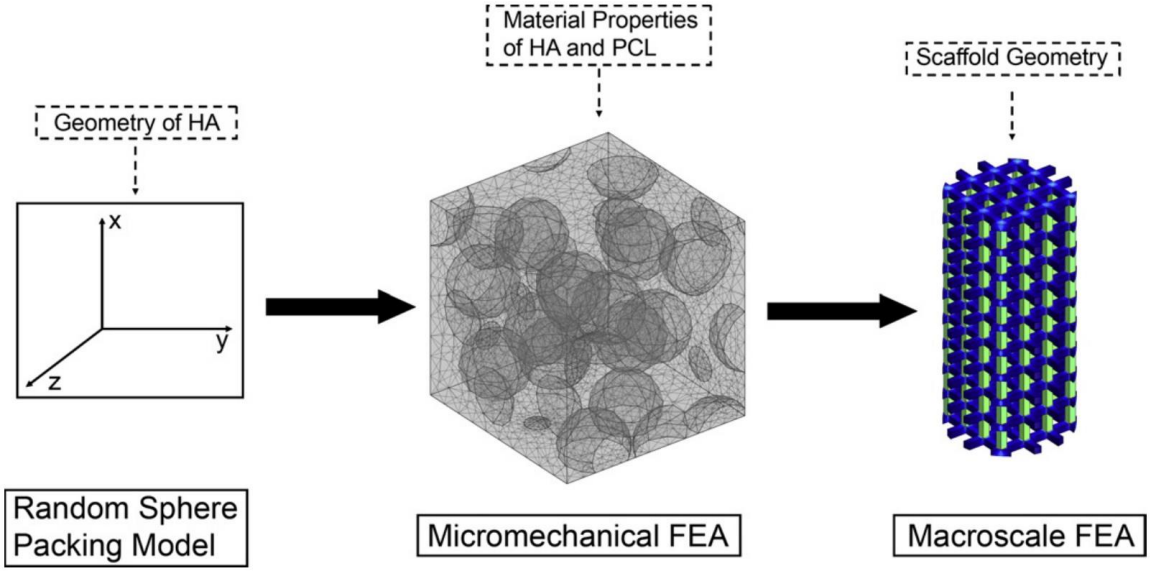

Figure 3.5. Diagram of the three-stage modeling process used to study the effects of filler loading on PCL:HA scaffolds [43].

The random sphere packing model used to model the distribution of HA is based on the work of Jodrey et al. [45] and implemented in MATLAB (see APPENDIX A). HA

particles were considered as spheres having a constant radius equal to the average particle size (25 μm). Fifty spheres were randomly placed with uniform distribution in a bounding box having a volume equal to the combined volume of the spheres (3.2725 x 10^6 μm^3). During placement of the spheres there was no constraint that the spheres should not overlap. The particles were iteratively moved apart in steps of λ until there was no longer any overlap. By using a large value for λ (~100 μm) low packing densities were obtained because the spheres had a larger average distance separating them when the end condition of no spheres overlapping was reached. Decreasing the value of λ from 100 to 1 μm resulted in the packing fraction increasing from 0.1 to 0.55 as seen in Figure 3.6.

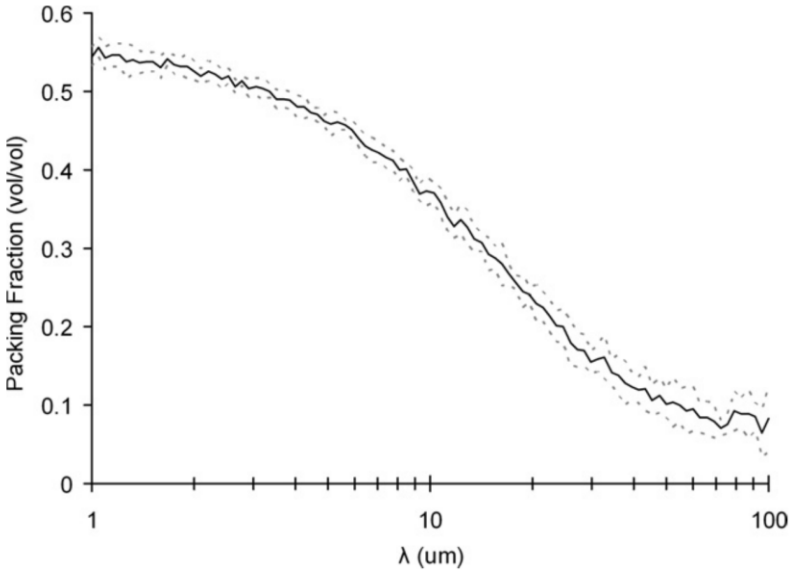

Figure 3.6. Distribution of packing fractions obtained from input step size $\boldsymbol{\lambda}$ in a random sphere packing model (n=10; dashed line indicates standard deviation) [43].

A micromechanical model was then created in COMSOL based on the location data obtained from the random sphere packing model. Each random configuration of the HA particles in a PCL matrix was created and meshed with quadratic tetrahedral elements. The HA particles that were partially outside of the bounding box were cropped so that only the space within the bounding box remained. Meshes varied in size from

16113 to 32507 elements based on the loading of HA and other factors arising from the random nature of the simulations. Boundary conditions were created on a pair of opposing faces with one face being held fixed and the other being displaced to an axial strain of 0.01 in compression. A linear stationary solver was then used and the reaction force at the fixed end was evaluated to determine the bulk elastic modulus using Hooke's Law. Five randomly generated geometries were created and loading was simulated in 3 different cases for the x, y, and z directions and then averaged for each loading fraction.

Using the bulk elastic moduli from the micromechanical model, the effective stiffness constants for the porous scaffolds were determined using a macroscale finite-element model in COMSOL so that they could be compared with mechanical testing of the scaffolds. Testing geometries were directly imported into the Structural Mechanics Module in COMSOL. The models were meshed using 6814, 16510 and 46568 tetrahedral elements for D695-1D, D695-2D, and D695-3D, respectively. A loading simulation was conducted with one end of the scaffold fixed and the other end strained in axial compression to 0.01. The resultant force at the fixed end was then divided by the effective area of the scaffolds which includes the porous channels to determine the effective stress. The effective stiffness constants were calculated using Hooke's Law from the effective stress and axial strain.

The material properties of the PCL and HA were assumed homogeneous and isotropic based on optical microscopy [46], mechanical testing, and previous computational modeling of SLS-processed PCL [25, 47]. The Poisson's ratio was assumed as 0.3. The elastic modulus of PCL (299.3 MPa) was determined from compression testing of solid gage pure PCL specimens, and the elastic modulus of HA

(3.69 GPa) was determined using a Hysitron TriboIndenter® (Eden Prairie, MN) to perform single nanoindentations.

3.5 Materials Used for LAMP

The macromer polyethylene glycol (600) diacrylate was purchased from Sartomer under the brand name SR-610 however Sartomer has since been acquired by Arkema (Colombes, France). The PEGDA used in this study has a viscosity of 90 cps at room temperature, a molecular weight of 742, and high solubility in water [48]. The chemical structure of PEGDA is given in Figure 3.7.

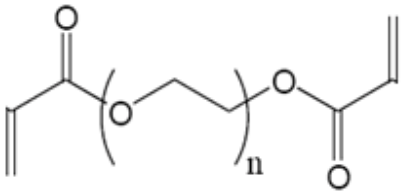

Figure 3.7. Chemical structure of PEGDA [48]

The photoinitiator Irgacure® 2959 having the chemical name 1-[4-(2-hydroxyethoxy)-phenyl]-2-hydroxy-2-methyl-1-propane-1-one was purchased from Ciba Specialty Chemicals (Basel, Switzerland). The chemical structure of Irgacure® 2959 is shown in Figure 3.8.

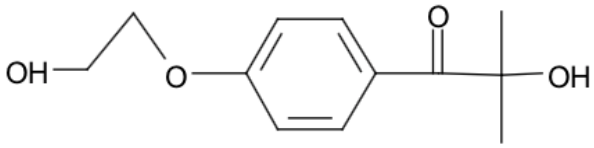

Figure 3.8. Chemical structure of Irgacure® 2959 [49]

Irgacure® 2959 is one of the few photoinitators used for biological study in the literature. It has some absorptivity at the lowest wavelength (365 nm) emitted by the UV light source used in LAMP as seen in Figure 3.9.

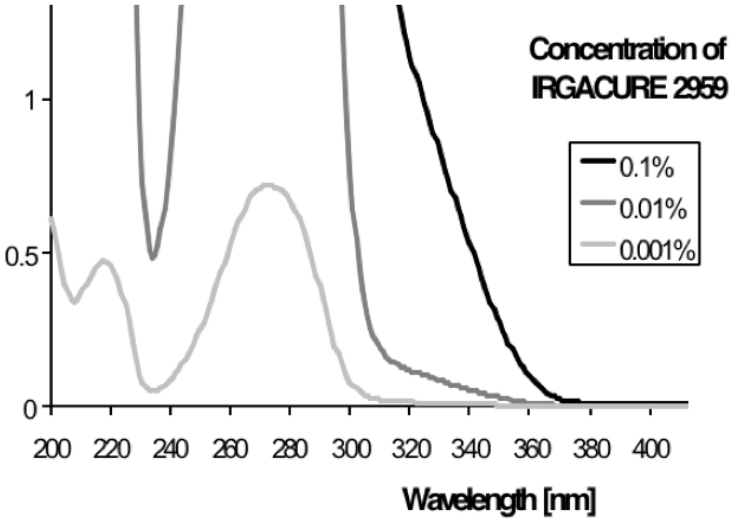

Figure 3.9. Absorption spectrum of the photoinitiator Irgacure® 2959 % in acetonitrile [49]

When exposed to UV radiation, Irgacure® 2959 dissociates and creates reactive radicals. The radicals disrupt the carbon-carbon double bond of the acrylate end groups on the PEGDA macromer causing free radical polymerization and creation of acrylate networks [50].

The UV absorber sulisobenzone also known as benzophenone-4 has the chemical name 4-hydroxy-2-methoxy-5-(oxo-phenylmethyl)benzenesulfonic acid was purchased from VWR International (Radnor, PA, USA). Sulisobenzone is a common component in sunscreen and provides broad spectrum absorbance of UV light. The chemical structure of sulisobenzone is given in Figure 3.10.

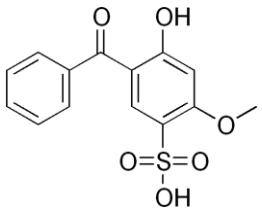

Figure 3.10. Chemical structure of sulisobenzone

UV absorbers such as benzophenones work by absorbing UV radiation thereby preventing the formation of free radicals by the photoinitiator. This effectively results in a

competition between the photoinitiator and UV absorber for incident light. The balance between the photoinitiator and UV absorber can be tailored to cause a steep attenuation of UV light as it travels through the resin resulting in a shorter cure depth. In terms of D_p and E_c, increasing the concentration of the UV absorber while keeping the concentrations of the macromer and photoinitiator constant results in a decrease in a decrease in D_p and little to no increase in E_c. Without a UV absorber or some other mechanism, it is not possible to change D_p without affecting E_c by only varying the macromer and photoinitiator concentrations.

The polysaccharide maltodextrin was used as a thickening agent to increase the viscosity of the mixture. Maltodextrin is a chain of D-glucose units with variable length (2 < n < 20) as shown in Figure 3.11.

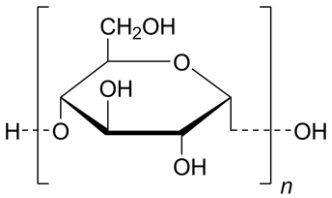

Figure 3.11. Chemical structure of maltodextrin

Maltodextrin was used because it dissolves well in aqueous solutions and can greatly increase the viscosity of liquids at relatively low concentrations as low as 0.5%. Maintaining a dynamic viscosity of the photocurable material in the region of 200-600 cP is important because too high of a viscosity would result in breaking fine features that are building when the recoater moves whereas a low viscosity would result in leakage through the seal and subsequent erosion of the wall.

3.6 Methodology for LAMP Fabrication

Photocurable hydrogel resins were prepared by mixing the hydrogel macromer,

photoinitiator, UV absorber, and thickening agents in saline solution for 12 hours on a rotary tumbler. The resin was kept in an amber bottle because direct exposure to sunlight would cause curing.

Optimizing the cure depth of the resin is important to ensure good mechanical properties as well as sharp feature resolution. The curing region needs some overlap with the underlying layer so that the layers are well bonded and interlayer delamination does not occur. A curing region that is too deep will result in poor resolution along the build axis.

Cure depth measurements were made by placing a glass slide on a dish of resin then running a grid of exposures (n=10) with varied exposure times corresponding to desired energy doses. The glass slide was then washed and a micrometer was used to measure the thickness of the cured samples. This data was then used to find the resin sensitivity and critical energy dose for the resin as described by Equation 2.4.3 a desirable resin formulation was then chosen based on these parameters.

The material formulations with desirable light sensitivities were then used for building 3D samples. To start a build, the z-axis stage is first moved to a level position with the surrounding window. Material is then dispensed from a hopper through a peristaltic pump to a recoating arm. The recoating arm dispenses material and moves left over the build area to an overflow well which feeds back to the hopper. The recoating arm then returns back to the starting position, and when the build area has a uniform layer of material the exposure head then exposes over the build area. The speed of the exposure head is adjusted to give the correct exposure time for the desired cured layer thickness.

During the exposure material is recovered from a vat below the build area and from the overflow well by peristaltic pumps.

The sequence of events that occur to complete a build are as follows:

1. The build stage moves down 50-100 μm.
2. A peristaltic pump dispenses ~100mL of material in a short burst and slowly primes.
3. The recoating arm moves left at 30 mm/s across the build platform to the overflow well.
4. The overflow well collects excess material and a peristaltic pump moves the material back to the supply.
5. The recoating arm moves back right across the build platform at 30 mm/s to skim excess material off the top of the build stage and to move out of the way of the exposure head which nests in the back left corner of the machine.
6. The exposure head smoothly rasters across the build stage at a speed determined by the exposure time and then returns to the nest position.
7. The process repeats.

Once the build finishes, the uncured material is drained out and the remaining walls, support structure, and parts are rinsed with water. Next the walls are cut off using a knife. The support structures are then broken off using a scraping tool. The parts are then carefully cut off the build platform and soaked in water.

3.7 Design of PEGDA Specimens

A variety of PEGDA specimens were designed in SOLIDWORKS to investigate the size, shape, and complexity of microfluidic channels that could be created by LAMP. Simple 1D and 2D circular channels were created to look at the difference in channel size manufacturability parallel vs perpendicular to the build direction. Complex 3D microfluidic channels were created to investigate the sizes and types of channels that are manufacturable. Square snake channels, circular helix channels, and circular branching channels were created with cross-sectional sizes from 0.381 to 1 mm.

Hollow dome shaped test geometries with circular channels were created in SOLIDWORKS to investigate the size of straight channels that could be created and cleared either parallel or perpendicular to the build direction. Three different sizes of circular channels at 0.375, 0.75, and 1.5 mm in diameter were specified for both channel orientations as shown in Figure 3.12. The domes have an inner and outer diameter of 7.5 and 10 mm respectively. The channels were placed near the positive z-axis limit of the specimens so they would not be in contact with the substrate and would therefore be less likely to be damaged during breakout.

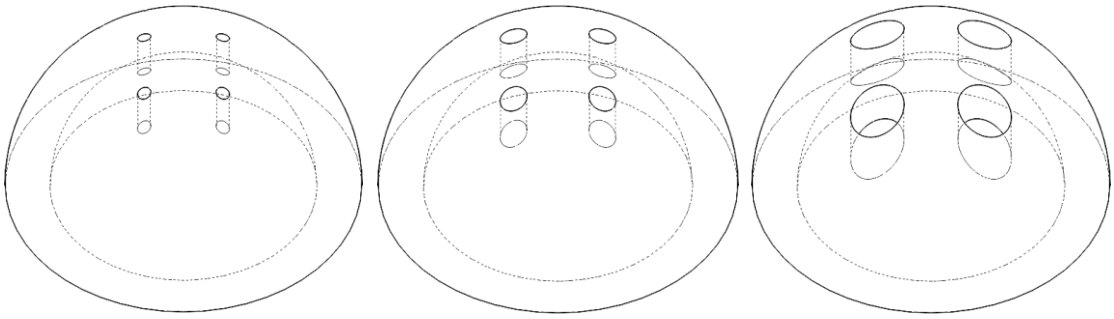

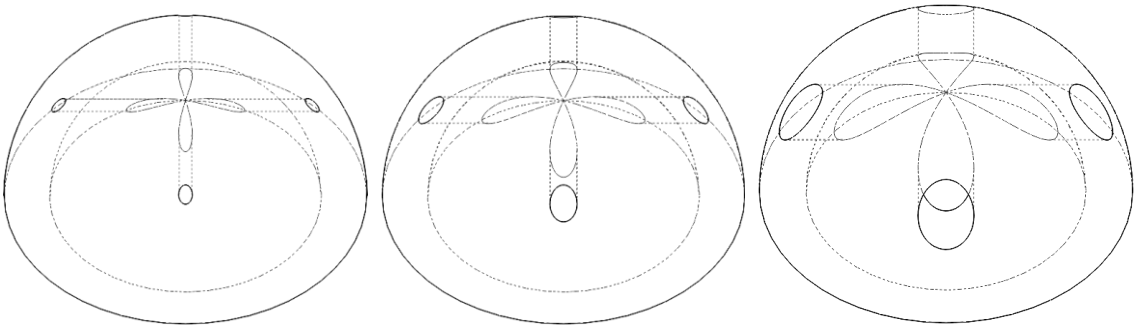

Figure 3.12. Designs of dome test geometries with 0.375, 0.75, and 1.5 mm circular channels oriented in the Z and XY directions

Several geometries with internal 3D microfluidic channels were designed in SOLIDWORKS to investigate the ability of LAMP to create complex flow geometries. Block specimens were created measuring 10 x 10 x 5.33 mm with either a 0.381 or 0.762 mm snaking channel as seen in Figure 3.13. An orthogonal channel design was chosen for the first attempt at fabricating 3D flow channels because the 90º turns are difficult to clear.

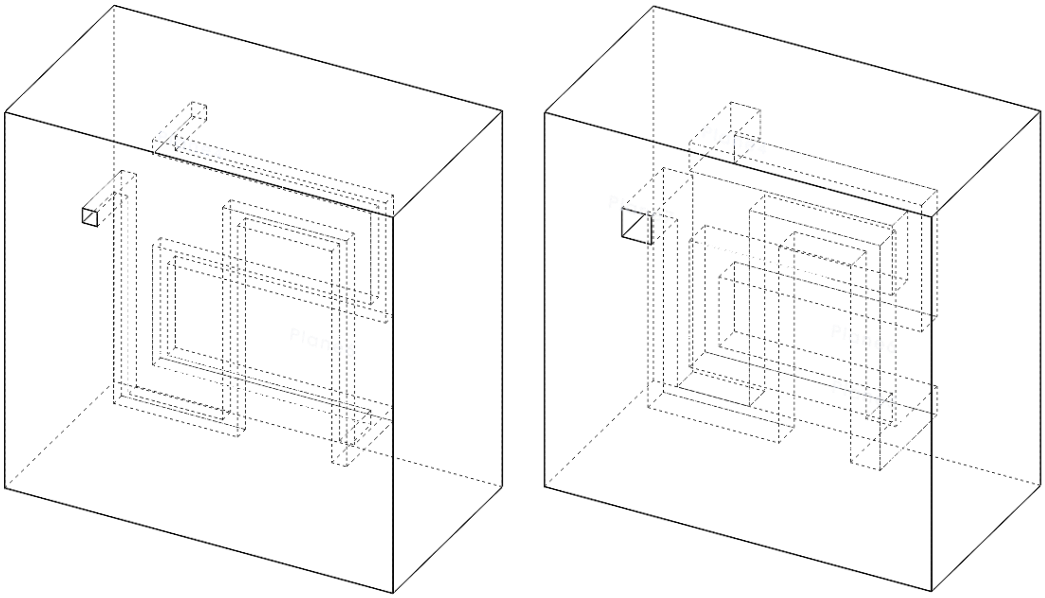

Figure 3.13. Designs of microfluidic geometries with snaking square channels having widths of 0.381 (left) and 0.762 mm (right).

Cylindrical geometries with a diameter of 12.5 mm and a height of 5.18 mm having a single helix circular channel were designed in SOLIDWORKS. The channels

were designed to have 0.5, 0.75, and 1 mm diameter cross-sections as shown in Figure 3.14.

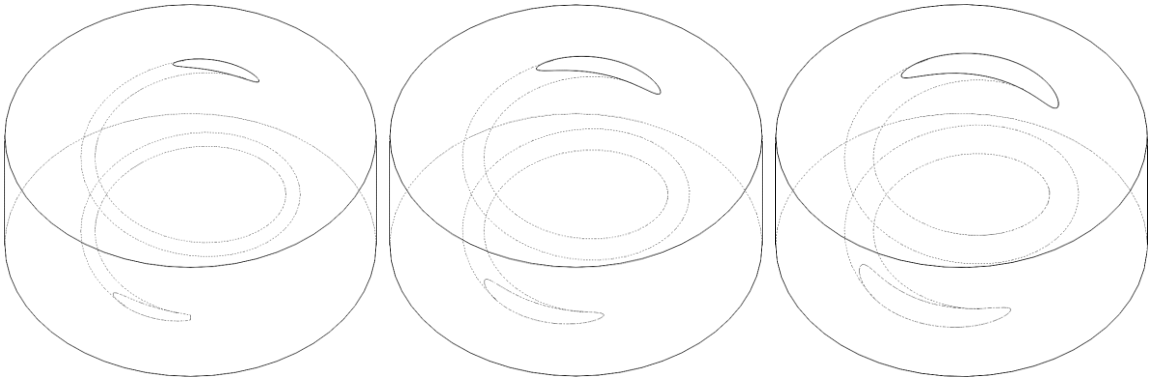

Figure 3.14. Designs of microfluidic geometries with helix circular channels having widths of 0.5 (left), 0.75 (center), and 1.00 mm (right).

Cylindrical geometries with a diameter of 12.5 mm and a height of 5.18 mm having circular branching channels were designed in SOLIDWORKS. The channels were designed to have 0.5, 0.75, and 1.0 mm diameter cross-sections as shown in Figure 3.15.

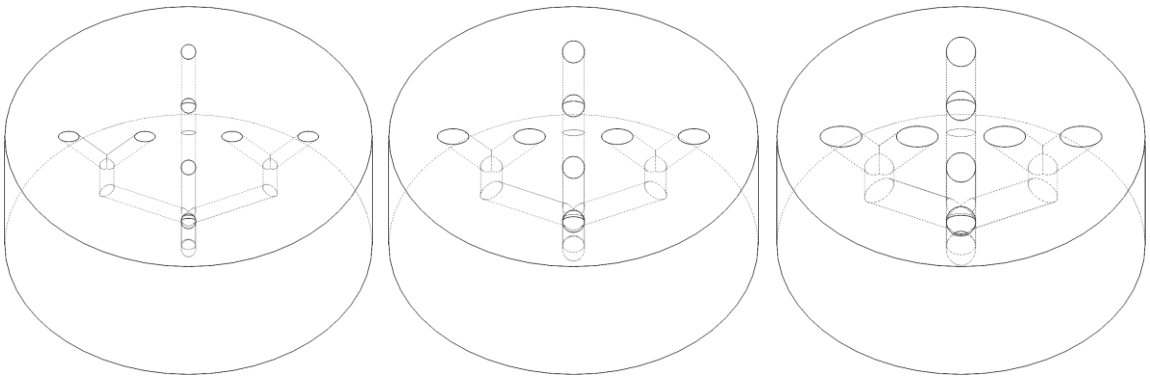

Figure 3.15. Designs of microfluidic geometries with branching circular channel having widths of 0.5 (left), 0.75 (center), and 1.00 mm (right).

A stereomicroscope with a 5x objective was used to characterize the microfluidic channels in the PEGDA specimens. Top and side view images of the intact specimens as well as planar images of the specimens after cleavage with a knife were taken. The RGB images were converted to grayscale and then analyzed using ImageJ software to manually

measure the dimensions of the channels. Digital photographs were also taken with a digital camera to give perspective of the size shape of the specimens.

3.8 Computational Fluid Dynamics Simulations of LAMP Processed Parts

Microfluidic test geometries were created in SOLIDWORKS to characterize the fluid flow through microfluidic channels. Geometries having channels oriented in the Z direction and the X-Y directions were created to investigate flow both parallel and perpendicular to the build direction (Z-axis). Circular channels were created at three different diameters: 0.15, 0.2, and 0.3 mm. The geometries are shown in Figure 3.16.

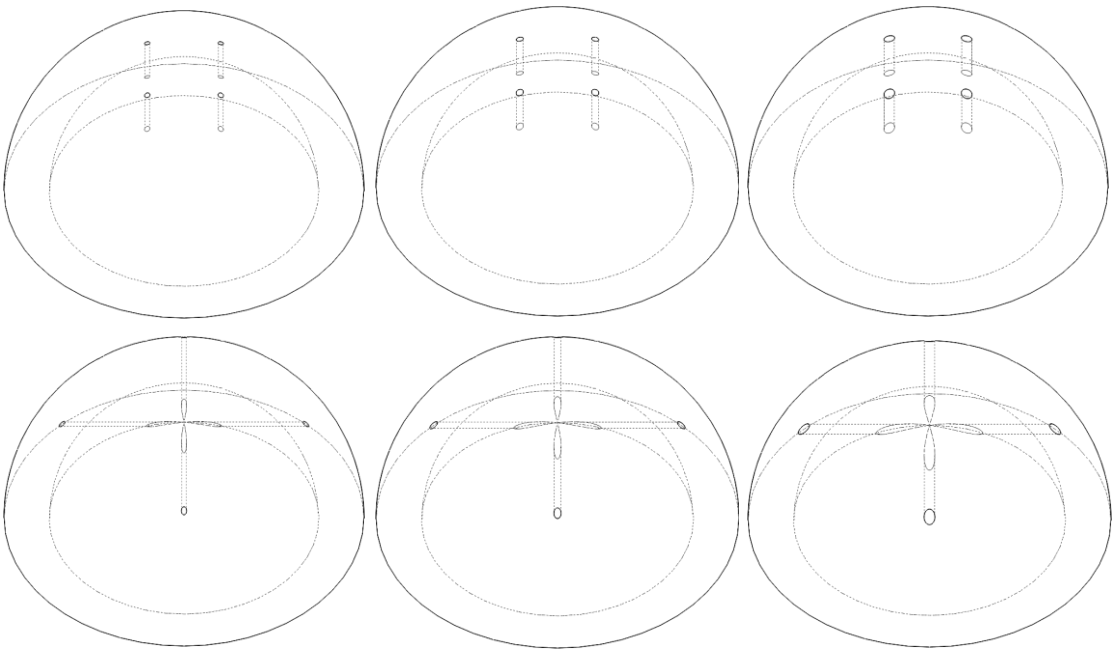

Figure 3.16. Designs of flow test specimens having channels oriented in the Z direction (top) and the X-Y directions (bottom) with circular channels having diameters of 0.15 (left), 0.2 (middle), and 0.3 mm (right).

Negatives of the microfluidic test geometries were imported into COMSOL Multiphysics (COMSOL Group, Stockholm, Sweden) using LiveLink for SOLIDWORKS to pull the native CAD geometries without having to export them as an

STL or VRML file. This method of import was used because unwanted boundaries that needed to be manually repaired were being created when using other options.

XZ and YZ symmetry planes were used to reduce the solution times. The top wall and ends of the channels were set as open boundaries with no pressure. All remaining walls were given a no-slip condition. The only external stimulus applied to the model was a volumetric force of $F_z = -g \cdot \rho$ to account for gravity, where F_z is a volumetric force in the z-direction, g is a constant for the acceleration due to gravity, and ρ is density. A physics-controlled meshing algorithm was used in COMSOL for each of the geometries and the mesh statistics are shown in Table 3.3.

Table 3.3. Mesh Statistics for CFD geometries

Geometry	Number of Elements	Minimum Quality	Average Quality
Z-Large	41,394	0.04987	0.645
Z-Medium	40,072	0.04283	0.645
Z-Small	40,723	0.0635	0.635
XY-Large	48,694	0.02382	0.643
XY-Medium	47,876	0.01623	0.629
XY-Small	49,257	0.02692	0.633

The average mesh quality for all the geometries was 0.638 with an average minimum quality of 0.0372 on a scale of 0 to 1. A laminar flow steady-state solver was then used to find the solution for each model with an average solution time of ~30s.

PEGDA specimens of the geometries were also fabricated by LAMP, using the method described in section 3.6, to experimentally validate the CFD results. After fabrication, breakout, and cleaning were finished the specimens were oriented with their open end pointed up and immersed in water. A stopwatch was then used to record the

time it took for each geometry to drain after removal from water. The drain time was measured for 2 identical specimens 3 times each giving 6 measurements.

CHAPTER 4

RESULTS

This chapter contains results and discussions regarding additive manufacturing of tissue engineering scaffolds for bone and cartilage. This section is divided into sections for SLS and LAMP. The SLS section is divided into material property characterization and computational modeling. The LAMP section focuses on feasibility of manufacturing and geometry characterization.

4.1 SLS Fabrication

SLS is a thermal manufacturing process where radiative heaters and an IR laser sinter and/or melt powder particles. The optimal SLS processing parameters are different depending on the selection of powder material. Suboptimal SLS processing parameters can result in the following:

1. **manufacturing-induced porosity** - the presence of voids in designed solid regions of the part that arise from incomplete densification of the powder
2. **thermal growth** - dilation of the part that results when extra powder attaches to the part from excessive sintering of surrounding powder
3. **curling** – curving of the part upwards along the build direction due to non-uniform cooling [51]

SLS processing parameters were optimized using a two-level factorial DOE in order to optimize the part density. Part density was chosen as the quality metric because it

correlates with the mechanical properties of the scaffolds, i.e. unwanted voids and unsintered powder present in the struts of the scaffolds greatly increase local stress concentrations causing mechanical failure at relatively low loads. The resulting optimal processing parameters are shown in Table 4.1.

Table 4.1. Optimal SLS processing parameters for PCL:HA composites at 0, 10, 20, and 30% volume loading.

Processing Parameter	Setting			
	100:0	90:10	80:20	70:30
Part Bed Temperature (°C)	46	50	50	50
Laser Power (W)	3.9	2.2	2.2	2.4
Scan Speed ($mm \cdot s^{-1}$)	1079.5	914	914	914
Scan Spacing (μm)	152.4	152.4	152.4	152.4
Energy Density ($J \cdot cm^{-2}$)	2.37	1.58	1.58	1.72

In the case of the composite powders, the part bed temperature can be maintained closer to the melting temperature of PCL because the HA acts as an anti-caking additive. Since the PCL is 30% closer to the melting temperature in this case a lower energy density was required to achieve full particle coalescence and densification.

Parts fabricated using the optimal processing parameters form the DOE were found to be dimensionally accurate (to within 3-8% of designed dimensions as measured by a Mitutuyo® Digimatic Caliper with 0.01 mm resolution), and near-fully dense (>95%) as determined by planar area-based void fraction analysis of cross-sectional micrographs. Porous mechanical test specimens fabricated using the optimal SLS processing parameters are shown in Figure 4.1.

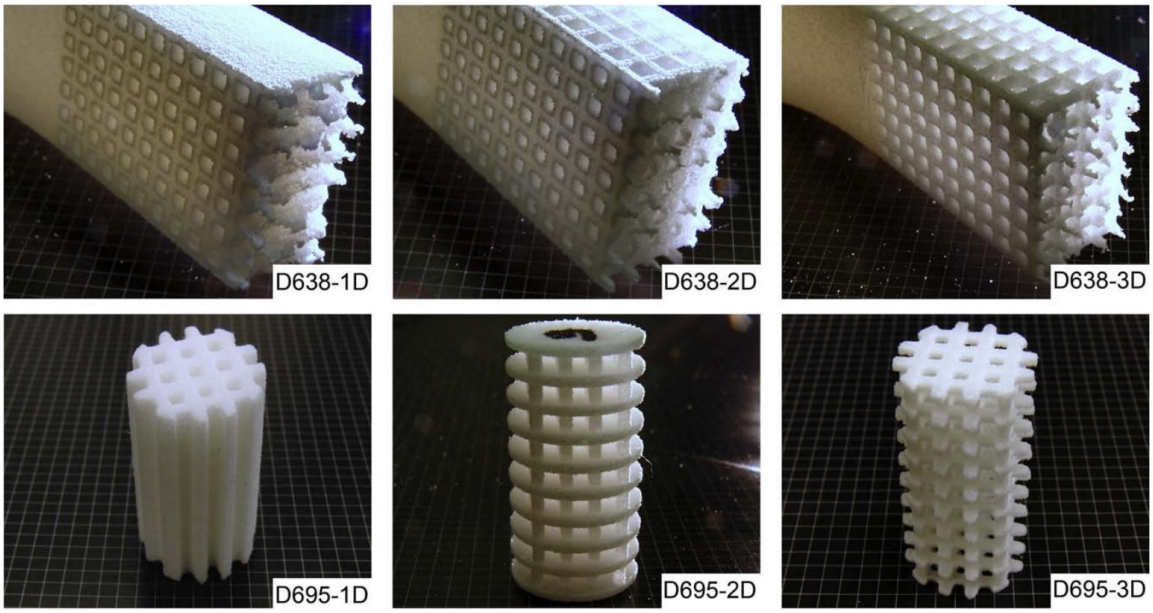

Figure 4.1. SLS processed PCL tensile (D638-1D, D638-2D, and D638-3D) post-fracture specimens and compressive (D695-1D, D695-2D, and D695-3D) specimens with 1D, 2D, and 3D orthogonal porous channels (placed on a 2 mm grid) [37].

4.2 Part Densities of SLS Specimens

The part densities of SLS processed PCL and PCL:HA specimens were determined by imaging of cross-sections and can be seen in Table 4.2. The part densities of neat PCL and PCL:HA composites reported here are very close to fully dense. This indicates successful optimization of the SLS processing parameters.

Table 4.2. Part densities of solid SLS processed PCL:HA specimens.

PCL:HA	Density (%)
100:0	99.6
90:10	99.8
80:20	99.5
70:30	99.6

Producing fully dense composite parts in many cases can be challenging because the addition of fillers to polymers reduces the sintering rate in SLS [52]. A slower sintering rate decreases the likelihood that a given space between particles is filled by molten polymer before solidification.

4.3 Mechanical Properties of SLS Parts

There is limited data on the mechanical properties of PCL and HA available from their manufactures and researchers, and there were no studies that report tensile and compressive mechanical properties of different layer orientations for SLS. The compressive mechanical properties of PCL:HA composites reported here are the highest reported in the literature likely due to the high part densities obtained through optimization of the SLS processing parameters.

4.3.1 Tensile and Compressive Mechanical Properties of Neat PCL

The manufacturer [36] of the PCL powder used in this works reports a tensile modulus of 430 MPa at a strain rate of 10 $mm \cdot min^{-1}$ for injection molded CAPA 6500 (M_n = 47,500). Pitt et al. [53, 54] studied the degradation of PCL and reported a tensile modulus of 264.8 MPa for melt-extruded PCL capsules (M_n = 50,900). Wehrenberg [55] reported a tensile modulus of 340 MPa and tensile strength of 19.3 MPa for compression molded PCL (M_n = 45,000). Engelberg and Kohn [56] reported a tensile modulus of 400 MPa and tensile strength of 16 MPa for compression-molded PCL (M_n = 42,500) and also noted that the high crystallinity inhibited solvent casting of PCL. Several other groups have also reported the mechanical properties of bulk processed PCL by conventional methods and their findings are given in Table 4.3.

Table 4.3. Bulk tensile mechanical properties of PCL reported in the literature [37].

Reference	Processing	Tensile modulus (MPa)	Tensile strength (MPa)	M_n	M_w
Perstorp [36]	Injection molding	430		47,500	84,500
Pitt et al. [53]	Melt extruding	264.8		50,900	84,500
Wehrenberg [55]	Compression molding	340	19.3		
Feng et al. [57]	Compression molding		21.6	45,000	50,400
Engelberg [56]	Compression molding	400	16	42,500	72,500
Vandamme et al. [58]	Compression molding	251.9		50,500	101,000
Rosa et al. [59]	Compression molding	429.1	16.9	50,000	80,000
Correlo [60]	Injection molding	378	27.3	64,000	124,000
Granado [61]	Injection molding	300	14		80,000

Several groups have previously reported compressive mechanical properties of PCL scaffolds manufactured by additive manufacturing processes in the literature. Zein et al. [62] have manufactured PCL scaffolds (M_n = 87,000) using fused deposition modeling (FDM) and reported mechanical properties ranging from a compression modulus of 4 MPa and a strength of 0.4 MPa at 77% porosity to a compression modulus of 77 MPa and strength of 3.6 MPa at 48% porosity. Shor et al. [63] used precision extruding deposition (PED) to create PCL scaffolds with a compression modulus of 59 MPa and a strength of 5.3 MPa at 65% porosity and solid gage specimens with a compression modulus of 109 MPa. Kim et al. [64], using a multi-headed deposition system (MHDS), produced PCL scaffolds (M_n = 65,000) with a compression modulus of 21.4 MPa and a strength of 1.3 MPa at 69.6% porosity. Williams et al. [25] used SLS to manufacture porous PCL scaffolds (M_n = 50,000) with designed porosity between 37% and 55% with compression moduli of 52–68 MPa and compression strengths of 2.0–3.2 MPa. Recently, Cahill et al. [47] reported a compression modulus of 47 MPa for bulk PCL processed by SLS and 6

MPa for PCL scaffolds at 55% porosity. The compressive properties of PCL scaffolds manufactured using different additive manufacturing techniques are listed in Table 4.4.

Table 4.4. Compressive mechanical properties of PCL scaffolds made by additive manufacturing [37].

Reference	Processing	Compression modulus (MPa)	Compression strength (MPa)	Porosity (%)	M_n	M_w
Hutmacher [65]	FDM	41.9	3.1	61	87,343	146,739
Zein [62]	FDM	4-77	0.4-3.6	48-77	87,000	147,700
Lam [66]	FDM	2.41	0.74	68	92,000	140,000
Zhou [67]	FDM	4.8	2.2	65		
Wang [68]	PED	150-200		53.1		44,000
Shor [63]	PED	59	5.3	65		
Shor [63]	PED	109		0		
Kim [64]	PED	21.0	1.3	69.6	65,000	
Williams [25]	SLS	52-68	2.0-3.2	37-55	50,000	
Cahill [47]	SLS	6		55		
Cahill [47]	SLS	47		0		

The mechanical properties of pure PCL processed by SLS were assessed by building D695 and D638 samples with their loading axis oriented both parallel (//) and perpendicular (⊥) to the build axis. This was done because incomplete bonding between layers would result in compromised structural stability in certain loading conditions. As can be seen in Figure 4.2 the compressive and tensile moduli are not significantly different when comparing the parallel and perpendicular specimens.

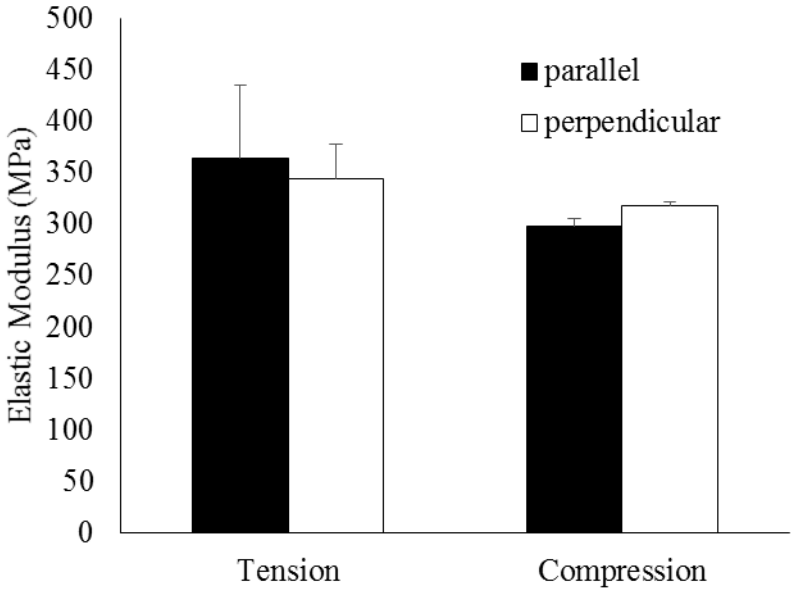

Figure 4.2. Elastic moduli of tensile (D638) and compressive (D695) SLS processed PCL specimens made with their long axis parallel and perpendicular to the build direction.

The tensile mechanical property measurements for SLS-processed solid and porous PCL specimens with their long axis oriented both parallel (across layers) and perpendicular (along layers) to the build direction are listed in Table 4.5 along with manufacturer reported values for injection molded solid specimens and reported values for trabecular bone. The mechanical properties are reported for the porous specimens using two methods to calculate the cross-sectional area: 1) in the first case the cross-sectional area is assumed to be the same as the solid specimens and the property is denoted as an effective property, and 2) in the second case the cross-sectional area is assumed to be the minimum cross-sectional area of the scaffold and the property is denoted as a corrected property. Even though the mechanical properties of SLS processed PCL exhibit slight dependence on the build orientation, they are comparable to those of PCL processed via injection molding. For solid PCL, the mean tensile strength in the perpendicular build orientation was 16.1 MPa, the mean Young's modulus was 343.9 - 363.4 MPa depending on the build orientation, and the mean 0.2% offset yield strength

was 8.2 - 10.1 MPa depending on the build orientation. Further, the strain at break was in excess of 790% for the perpendicular build orientation.

Table 4.5. Mechanical property assessment of solid and scaffold pure PCL specimens with parallel and perpendicular build orientations [37].

	Property	Unit	SLS					Injection Molding[2]	Trabecular Bone[3]
			Solid Specimen		Scaffold Specimen[1]				
			//	⊥	1D	2D	3D		
Tension	Effective Elastic Modulus, E	MPa	363.4 ± 71.6	343.9 ± 33.2	140.5 ± 19.6	42.0 ± 6.9	35.5 ± 5.8	430	---
	Corrected Elastic Modulus, E	MPa	363.4 ± 71.6	343.9 ± 33.2	325.6 ± 45.4	657.4 ± 108	555.7 ± 90.8	430	---
	Effective 0.2% Offset Yield Strength, σ_Y	MPa	8.2 ± 1.0	10.1 ± 1.5	3.2 ± 0.6	0.67 ± 0.08	0.67 ± 0.06	17.5	---
	Corrected 0.2% Offset Yield Strength, σ_Y	MPa	8.2 ± 1.0	10.1 ± 1.5	7.4 ± 1.4	10.5 ± 1.3	10.5 ± 0.9	17.5	---
	Strain at Yield, ε_Y	mm/mm	0.024 ± 0.006	0.031 ± 0.002	0.024 ± 0.001	0.017 ± 0.002	0.020 ± 0.002	---	---
	Effective Ultimate Tensile Strength, σ_{UT}	MPa	10.5 ± 0.3	16.1 ± 0.3	4.5 ± 0.4	1.2 ± 0.2	1.1 ± 0.1	---	---
	Corrected Ultimate Tensile Strength, σ_{UT}	MPa	10.5 ± 0.3	16.1 ± 0.3	10.4 ± 0.9	18.8 ± 3.1	17.2 ± 1.6	---	---
	Strain at Break, ε_B	mm/mm	0.043 ± 0.007	8.0 ± 0.3	0.095 ± 0.022	0.092 ± 0.022	0.096 ± 0.025	> 7	---
Compression	Effective Elastic Modulus, E	MPa	297.8 ± 7.1	317.1 ± 3.9	133.4 ± 2.6	12.1 ± 0.5	14.9 ± 0.6	---	1 to 5000
	Corrected Elastic Modulus, E	MPa	297.8 ± 7.1	317.1 ± 3.9	309.2 ± 6.0	189.4 ± 7.8	233.2 ± 9.4	---	---
	Effective 0.2% Offset Yield Strength, σ_Y	MPa	12.5 ± 0.3	10.3 ± 0.2	4.25 ± 0.05	0.45 ± 0.01	0.42 ± 0.03	---	---
	Corrected 0.2% Offset Yield Strength, σ_Y	MPa	12.5 ± 0.3	10.3 ± 0.2	9.9 ± 0.1	7.0 ± 0.2	6.6 ± 0.5	---	---
	Strain at Yield, ε_Y	mm/mm	0.052 ± 0.003	0.037 ± 0.002	0.0370 ± 0.000	0.0376 ± 0.001	0.0268 ± 0.003	---	---
	Effective Ultimate Tensile Strength, σ_{UT}	MPa	38.7 ± 0.3	38.80 ± 0.7	10.0 ± 0.6	0.60 ± 0.0	0.60 ± 0.0	---	0.1 to 27.3
	Corrected Ultimate Tensile Strength, σ_{UT}	MPa	38.7 ± 0.3	38.80 ± 0.66	23.2 ± 1.4	9.4 ± 0.0	9.4 ± 0.0	---	---

Notes: (1) $\mu \pm \sigma$ where μ denotes the mean and σ denotes the standard deviation, (2) effective properties are calculated with the same cross-sectional area as the solid specimen and corrected properties are calculated using the minimum cross-sectional area of the scaffold, and (3) n=6.

[1]Porous compressive specimens tested parallel to SLS build direction, porous tensile specimens tested perpendicular to SLS build direction.

[2]Reported by Perstorp Caprolactone, tests were conducted at a strain rate of 10 mm·min^{-1} to determine E and 100 mm·min^{-1} in all other cases.

[3]Compressive mechanical properties of trabecular bone reported in the literature by various groups [69-74].

In the case of the scaffold specimens, the tensile strength and Young's modulus undergo a significant reduction relative to the bulk properties. For the D638-1D specimens, the mean tensile strength was 4.5 MPa and the mean Young's modulus was 140.5 MPa, indicating a reduction to approximately 28% and 40% of the respective bulk values. For D638-2D and D638-3D, the reduction in tensile properties was even more drastic, with the tensile strength and modulus of D638-2D reduced to 7.5% and 12% of the respective bulk values while the tensile strength and modulus of D638-3D were reduced to 7% and 10% respectively of the bulk values.

The compressive mechanical properties of bulk and porous PCL specimens measured in this study are reported in Table 4.5. For solid PCL, the compression modulus was 299 - 317.1 MPa and the yield strength was 10.3-12.5MPa depending on the build orientation. It should be noted that the compression modulus reported here is over two times higher than what was previously obtained using unoptimized SLS parameters [25]. A sharp reduction in elastic modulus was observed when comparing the scaffold specimens to the solid specimens; however, the strain at yield did not drop as drastically. For D695-1D, yield strength and elastic modulus were reduced to 37% and 43% of the bulk values respectively. For D695-2D, the elastic modulus and yield strength were both reduced to approximately 4% of the respective bulk values; while for D695-3D, these values were reduced to 3.7% and 4.8% of the respective bulk values.

To summarize, 1-D, 2-D and 3-D orthogonally porous PCL compressive specimens with 2 x 2 mm square pore channels and 700 μm struts were produced by SLS, having a mean compression modulus between 14.9 and 113.4MPa and an ultimate compression strength between 0.6 and 10.0MPa for porosities ranging from 44.8-76.5%.

It should be noted that the increase in porosity from 2D to 3D scaffold geometries was not accompanied by an appreciable reduction in elastic modulus or yield strength likely because the material that was removed was located in regions of low strain. The compressive mechanical properties presented here are the highest reported values for scaffolds produced by SLS and among the highest reported for similar scaffolds produced through other layered manufacturing techniques. The compression modulus values of human trabecular bone range from 1 to 5000 MPa and the ultimate compression strength ranges from 0.1 to 27.3MPa [69-75] . Thus, the compressive mechanical properties of the porous PCL specimens reported in this work fall within the lower range of values reported for human trabecular bone.

4.3.2 Compressive Mechanical Properties of PCL:HA Composites

The compressive mechanical property measurements of SLS-processed solid and designed porous PCL:HA specimens are listed in Table 4.6. An overall improvement in compression modulus (*E*) was observed with the inclusion of HA in almost all cases. A significant difference ($n=5$, $p<0.05$) was not observed in the compression modulus of solid gage samples when comparing pure PCL to the 10% loaded PCL:HA composite samples. In the case of the 1D, 2D and 3D scaffold specimens, a significant difference ($n=5$, $p<0.05$) was observed in every case when comparing the effective compressive modulus of the corresponding pure PCL (100:0) scaffolds to the 90:10, 80:20 and 70:30 PCL:HA composite scaffolds. In summary, a significant increase in compressive modulus was measured when increasing the HA loading of the composite by as little as 10% in 11 out of the 12 cases.

Table 4.6. Mechanical property assessment of bulk and porous SLS-processed PCL:HA (ratios indicate volume) [43].

PCL:HA	Property	Unit	Solid Specimen	Scaffold Specimen		
				1D	2D	3D
100:0	Effective Elastic Modulus, E	MPa	299.3 ± 4.6	133.4 ± 1.3	12.1 ± 0.2	14.9 ± 0.3
	Corrected Elastic Modulus, E	MPa	299.3 ± 4.6	309.2 ± 3.0	189 ± 3.1	233.2 ± 4.7
	Strain at Yield, ε_Y	mm/mm	0.052 ± 0.001	0.037 ± 0.000	0.038 ± 0.000	0.027 ± 0.002
	Effective Ultimate Compressive Strength, σ_{UC}	MPa	34.5 ± 0.1	10.0 ± 0.3	0.7 ± 0.2	0.6 ± 0.0
	Corrected Ultimate Compressive Strength, σ_{UC}	MPa	34.5 ± 0.1	23.2 ± 0.7	11.0 ± 3.1	9.4 ± 0.0
90:10	Effective Elastic Modulus, E	MPa	311.2 ± 15.1	182.6 ± 13.1	36.6 ± 2.7	26.4 ± 1.1
	Corrected Elastic Modulus, E	MPa	311.2 ± 15.1	423.2 ± 30.4	572.9 ± 42.3	413.2 ± 17.2
	Strain at Yield, ε_Y	mm/mm	0.0054 ± 0.006	0.047 ± 0.007	0.034 ± 0.005	0.027 ± 0.002
	Effective Ultimate Compressive Strength, σ_{UC}	MPa	33.7 ± 1.0	10.8 ± 0.3	2.4 ± 0.8	0.8 ± 0.05
	Corrected Ultimate Compressive Strength, σ_{UC}	MPa	33.7 ± 1.0	25.0 ± 0.7	37.6 ± 12.5	12.5 ± 0.8
80:20	Effective Elastic Modulus, E	MPa	415.5 ± 17.6	261.9 ± 8.3	21.2 ± 2.0	25.9 ± 2.1
	Corrected Elastic Modulus, E	MPa	415.5 ± 17.6	607.0 ± 19.2	331.8 ± 31.3	405.4 ± 32.8
	Strain at Yield, ε_Y	mm/mm	0.037 ± 0.002	0.045 ± 0.003	0.04 ± 0.02	0.034 ± 0.008
	Effective Ultimate Compressive Strength, σ_{UC}	MPa	32.0 ± 1.0	14.5 ± 0.8	1.9 ± 0.3	1.0 ± 0.1
	Corrected Ultimate Compressive Strength, σ_{UC}	MPa	32.0 ± 1.0	33.6 ± 1.9	29.7 ± 0.7	15.7 ± 0..2
70:30	Effective Elastic Modulus, E	MPa	498.3 ± 21.8	271.9 ± 17.3	28.8 ± 3.5	36.2 ± 1.0
	Corrected Elastic Modulus, E	MPa	498.3 ± 21.8	630.2 ± 40.1	450.8 ± 54.8	566.6 ± 15.7
	Strain at Yield, ε_Y	mm/mm	0.050 ± 0.006	0.033 ± 0.003	0.037 ± 0.2	0.026 ± 0.005
	Effective Ultimate Compressive Strength, σ_{UC}	MPa	24.6 ± 0.8	10.6 ± 0.7	1.5 ± 0.1	0.9 ± 0.3
	Corrected Ultimate Compressive Strength, σ_{UC}	MPa	24.6 ± 0.8	24.6 ± 1.6	23.5 ± 1.6	14.1 ± 4.7

Solid gage samples showed an increase from 299.3 to 498.3 MPa when increasing the loading of HA from 0 to 30% and in the scaffold with the highest porosity (80.9%), the compressive modulus increased more than 100% (14.9 to 36.2 MPa). The improvement in compressive moduli for the scaffolds can be attributed to particulate reinforcement by the hard-phase HA filler. The ultimate compressive strength (σ_{uc}) and strain at yield (ε_y) of the solid and scaffold specimens did not improve with increased loading of HA.

The closest compression properties found in the literature were reported by Lu et al. [76] using a material jetting system to create a negative for a mold and then injection molded PCL:HA composites at 0, 10, and 20% filler loading with compression moduli of 215.4 ± 6.6, 447.6 ± 24.6, and 546.1 ± 27.8 MPa respectively. In every case except for the neat polymer the elastic moduli presented by Lu et al. were higher which is likely due to better dispersion of HA.

4.4 Computational Modeling of PCL and PCL:HA Scaffolds

4.4.1 Neat PCL Scaffolds in Tension and Compression

For neat PCL, the effective tension modulus and compression modulus were computed for the porous D638 and D695 geometries respectively using experimentally determined bulk properties. Plots of the von Mises stress distributions (Figure 4.3 and Figure 4.4) in the models showed no elements above the yield strength at 1% strain for solid neat PCL. Observation of the stress distribution in both the tensile and compressive scaffolds showed relatively low stress concentrations in the design solid regions that were

changed to void regions in going from the 2-D to 3-D geometries thus explaining the small change in mechanical properties between the 2-D and 3-D geometries.

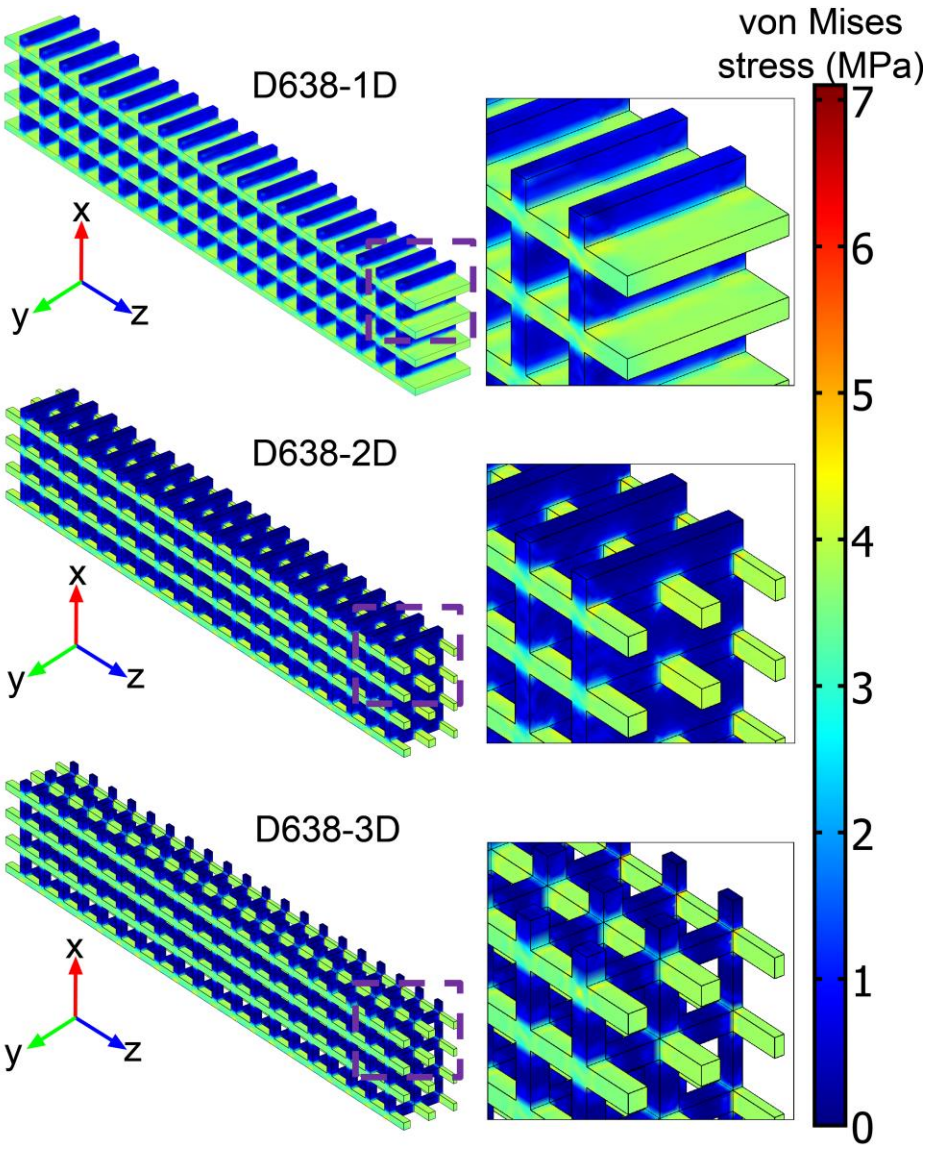

Figure 4.3. Plots of von Mises stress distributions for porous D638 tensile geometries [37].

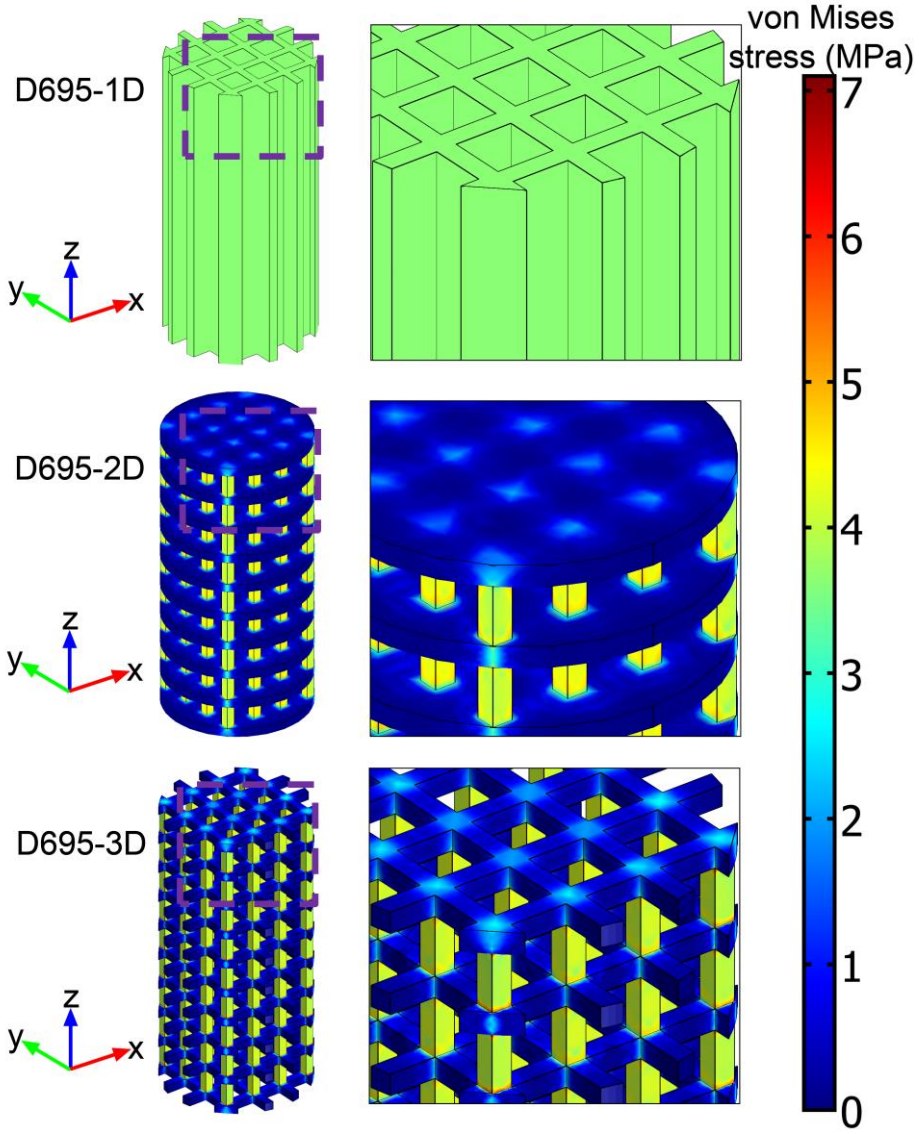

Figure 4.4. Plots of von Mises stress distributions for porous D695 compressive geometries [37].

Effective Young's moduli were computed in tension and compression at 1% axial strain using of the scaffold geometries and were in good agreement with the results from mechanical testing as shown in Figure 4.5.

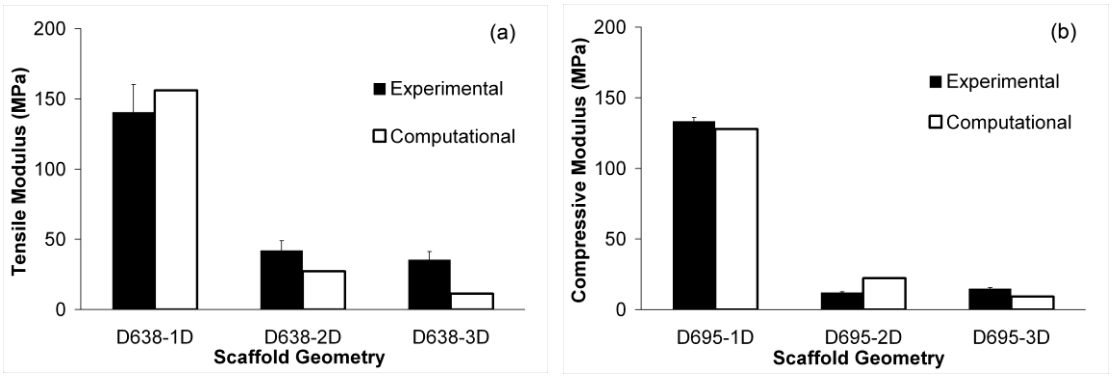

Figure 4.5. Experimental and computational effective (a) tensile moduli for D638 scaffold geometries and (b) compressive moduli for D695 scaffold geometries (error bars denote standard deviation; n=6).

The model tended to under-predict the effective modulus by a factor of 30%; however, it was expected that the model would tend to over-predict the effective modulus of the scaffolds in all cases because the bulk modulus used in the modulus was determined experimentally from solid gage specimens that tend to have a higher average density than scaffolds [26]. One possible cause for the under-prediction of the effective stiffness could be that the scaffolds were found to be measure 3-8% larger than designed due to partially sintered on the surface of the scaffolds.

4.4.2 PCL:HA Composite Scaffolds in Compression

A micromechanical modeling approach was used to compute the expected elastic moduli of SLS processed PCL:HA composites. Representative unit cells that were created by the random sphere packing model described in section 3.4 were analyzed using a finite element approach to determine their compression moduli. The compression moduli computed using this approach are shown in Table 4.7.

Table 4.7. Computed compression moduli of PCL:HA unit cells with 0, 10, 20, and 30% HA.

PCL:HA	Compression Modulus (MPa)
90:10	354.0
80:20	444.9
70:30	576.5

The computed compression moduli are in agreement with measurements from mechanical testing of solid gage specimens with an average error of 12.17%. A sharp increase in the elastic modulus of the composite can be observed as filler loading increases which is similar to other reinforced polymer composite systems.

The bulk properties from the micromechanical model were then used to model the stresses in the D695 porous composite specimens. Plots of the von Mises stress distributions for composite D695 scaffolds are shown in Figure 4.6. Stresses were evenly distributed in the 1D scaffold case. There were stress concentrations at the corners of the columns of the 2D and 3D scaffolds. In the areas of the high stress concentration, the von Mises stress did not exceed the yield stress for the bulk material.

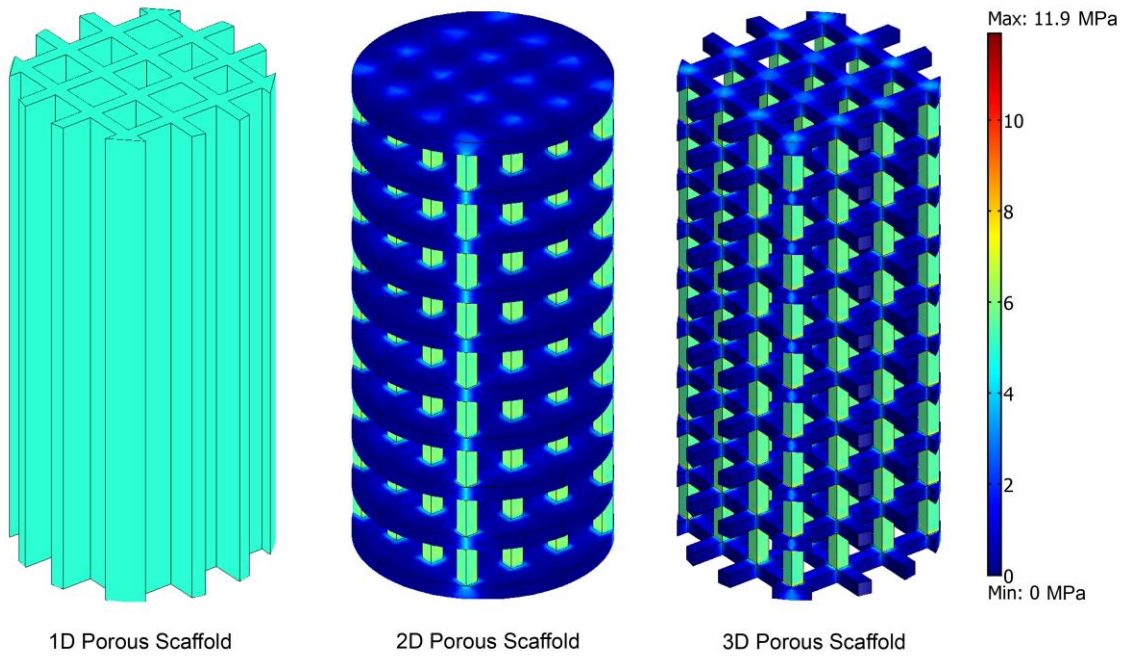

Figure 4.6. von Mises stress plots for porous compressive scaffold geometries; (left) 1D porous, (center) 2D porous and (right) 3D porous scaffolds for PCL:HA 70:30 [43]

A comparison of the computationally predicted vs experimentally measured effective compression moduli for D695-solid, D695-1D, D695-2D, and D695-3D composite test specimens is shown in Figure 4.7.

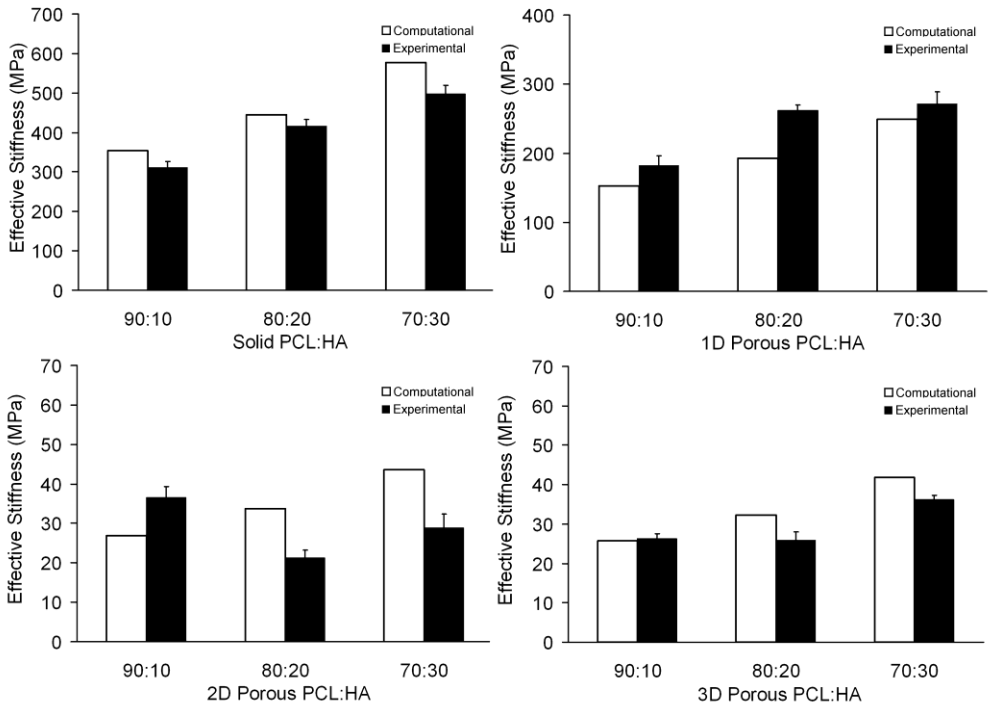

Figure 4.7. Experimental and computational effective compression moduli for 90:10, 80:20 and 70:30 PCL:HA composites: (top left) solid; (top right) 1-D porous; (bottom left) 2-D porous; (bottom right) 3-D porous (error bars denote standard deviation; n = 5) [43]

Compressive effective moduli for the porous scaffold geometries were predicted by FEA and also closely agreed with the results from mechanical testing with an average under-prediction of 25.65%. The average error of the FEA of PCL:HA composites reported here is lower than what has been reported in the literature by Williams et al. [25] (100% error) and Cahill et al. [47] (67% error). The highest amount of error was observed in the 2D porous scaffolds. One possible reason for the disagreement could be due to the 2D porous scaffolds having cylindrical solid sections that hinder particle coalescence.

4.5 LAMP Fabrication

LAMP is a photocuring manufacturing process where an overhead UV light source on an XY gantry system cures a resin that is deposited on a Z-axis build platform

by an X-axis recoater. The failure or success of a LAMP build hinges on the material composition of the photocurable material system. The properties of the material system that are most important are:

1. **light sensitivity** – the cure depth of the resin is directly determined by the light sensitivity of the resin and energy density from the exposure head.
2. **viscosity** – the sealing mechanism of the machine works best with viscosities over 200 cP while the material deposition system works best with viscosities below 600 cP.
3. **volumetric shrinkage after curing** – volumetric shrinkage for acrylate based systems can be an issue that results in curling.

The light sensitivity of the material system was the first property that was optimized by changing the ratio of water, macromer, photoinitiator, and UV absorber. It was found that increasing the UV absorber concentration had a strong effect on D_p without increasing E_c as can be seen in Figure 4.8.

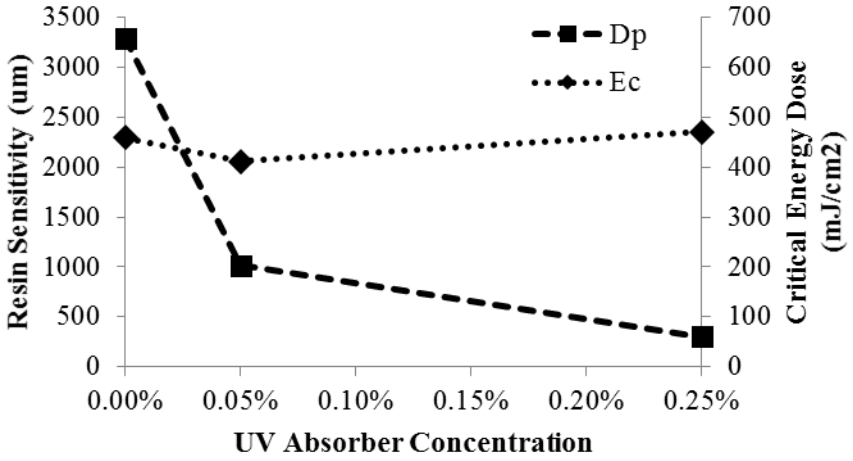

Figure 4.8. Plot of the effect of the UV absorber concentration (%w/w) on $\boldsymbol{D_p}$ and $\boldsymbol{E_c}$.

In the case of the macromer and photoinitiator concentrations, increasing either of their concentrations resulted in an increase in D_p and decrease in E_c. Figure 4.9 highlights the effect of the macromer concentration on D_p and E_c.

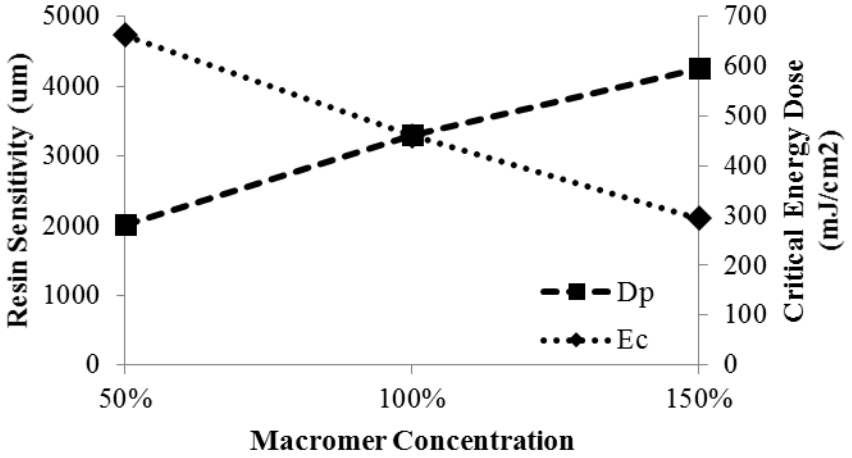

Figure 4.9. Plot of the effect of the macromer concentration (%w/w) on $\boldsymbol{D_p}$ and $\boldsymbol{E_c}$.

The final material composition that gave desirable light sensitivity and viscosity consisted of water as the solvent, PEGDA as the macromer, Irgacure® 2959 as the photoinitiator, sulisobenzone as the UV absorber, sodium chloride, and maltodextrin. The concentrations of each component are shown in Table 4.8.

Table 4.8. Photocurable material composition used for LAMP

Material	Concentration (% w/w)
Water	51.2
PEGDA	38.4
Irgacure® 2959	3.8
sulisobenzone	0.3
sodium chloride	2.6
maltodextrin	3.8

The PEGDA dome-shaped geometries described in section 3.7 were fabricated using an energy density of 510 mJ/cm^2 to give a desired cure depth of 152 µm. After breakout, each sample was flipped upside down and immersed in water to fill the inside

of the dome with liquid. They were then allowed to drain to make sure that all of the geometries had channels that were fully cleared.

A stereomicroscope was used to characterize the morphology of the PEGDA specimens. Micrographs of the PEGDA specimens are shown in Figure 4.10 from the top perspective along the build direction and also from a side view. Some stair stepping was observed corresponding to the 76.2 µm layer thickness.

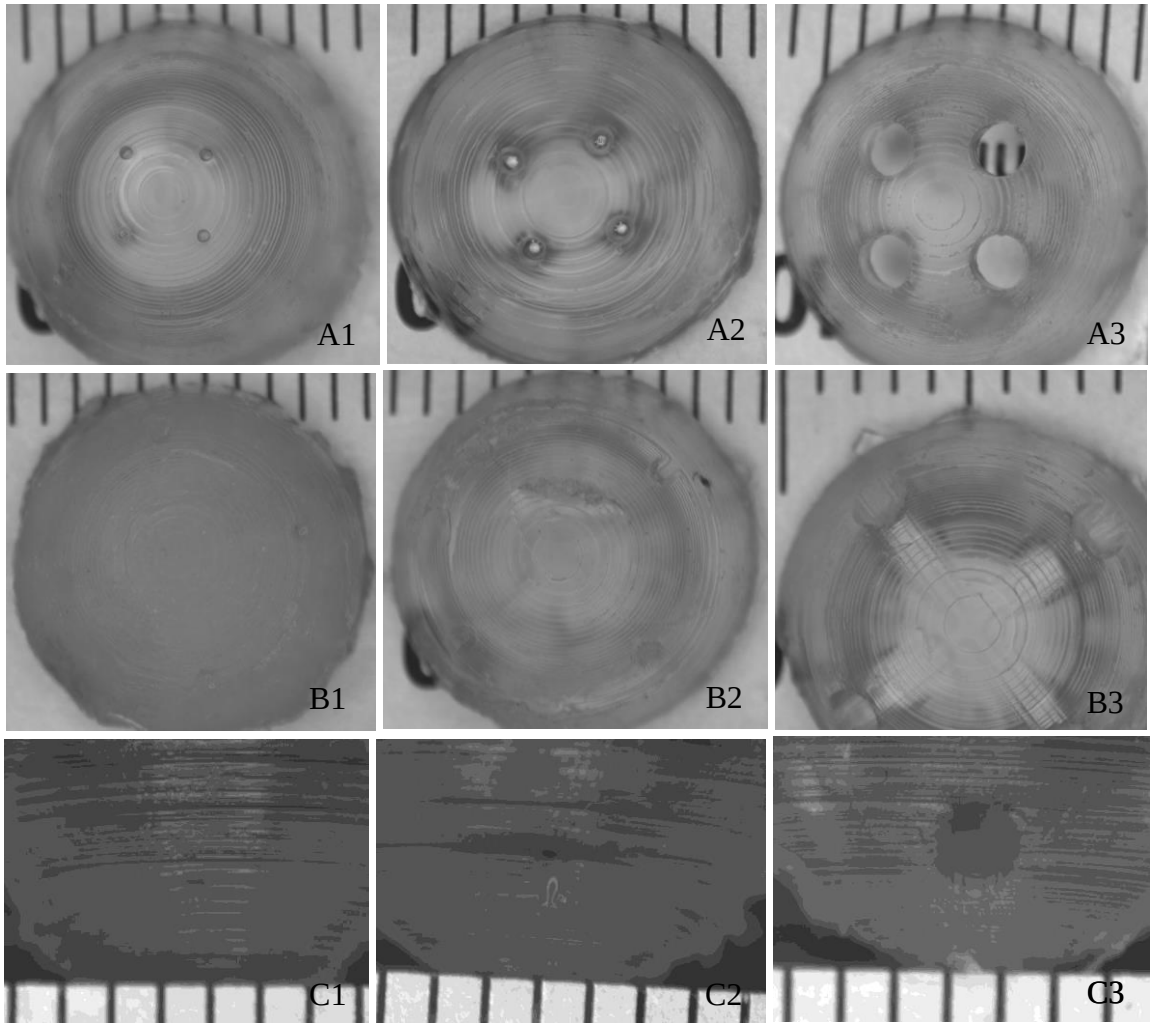

Figure 4.10. Stereomicrographs with a 1 mm scale of PEGDA dome specimens with (1) 0.375, (2) 0.75, and (3) 1.5mm circular channels oriented (A) parallel and (B,C) perpendicular to the build direction.

The channel diameters of the PEGDA specimens were characterized by optical microscopy. The designed and measured channel diameters are reported in Table 4.9.

with an average error of 5%. It was expected that the channels would be slightly smaller than designed due to side scattering and over-curing; however, in every case the channels were slightly larger than designed.

Table 4.9. Channel diameters for PEGDA specimens as measured by optical microscopy

Channel Orientation	Designed Channel Diameter (mm)	Measured Channel Diameter (mm)
Z	0.375	0.39
Z	0.75	0.79
Z	1.5	1.60
XY	0.375	0.39
XY	0.75	0.79
XY	1.5	1.59

Digital photographs were also taken of the PEGDA domes specimens to give some perspective of their macroscale morphology (Figure 4.11).

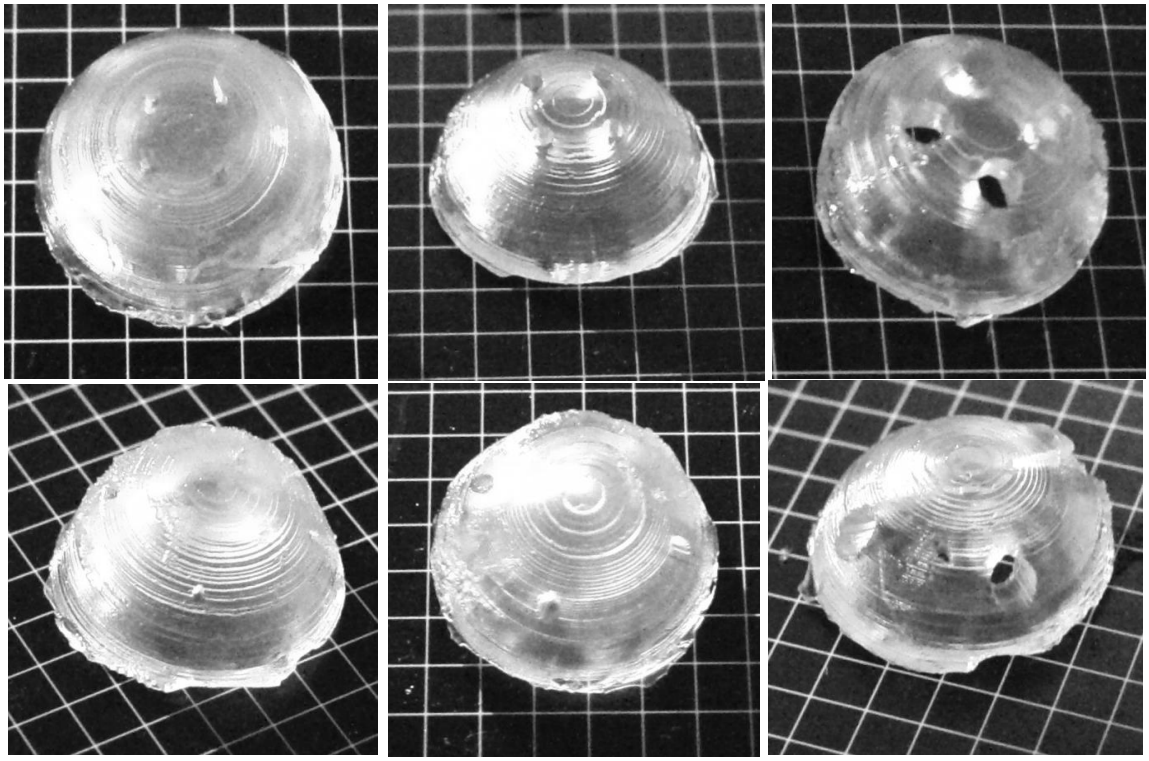

Figure 4.11. Digital photographs with a 2mm grid of PEGDA dome specimens with 0.375 (left), 0.75 (middle), and 1.5 mm (right) diameter circular channels oriented parallel (top) and perpendicular (bottom) to the build direction.

PEGDA microfluidic block geometries with a 3D snaking channel as described in section 3.7 were fabricated by LAMP to investigate whether or not complex flow geometries could be fabricated and cleared. Images of the PEGDA microfluidic specimens with a 0.381 and 0.762 mm channel after fabrication and breakout are shown in Figure 4.12.

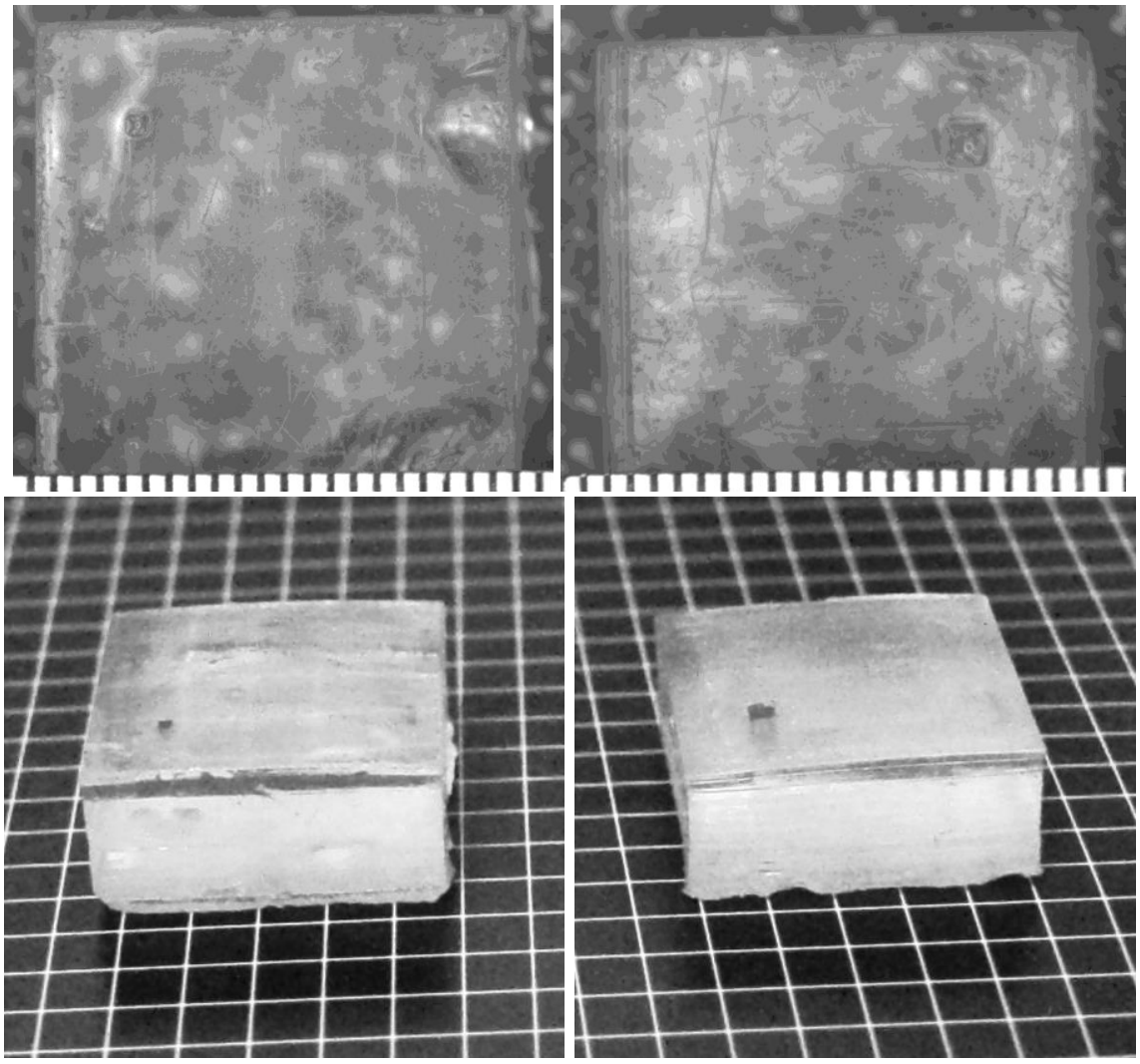

Figure 4.12. Stereomicrographs with a 0.5mm scale (top) and digital photographs with a 2mm grid (bottom) of PEGDA microfluidic specimens with 0.381 (left) and 0.762 mm (right) square channels

Additional images showing an outline of the 0.762mm channel and the corresponding build image used to create the channel are shown in Figure 4.13.

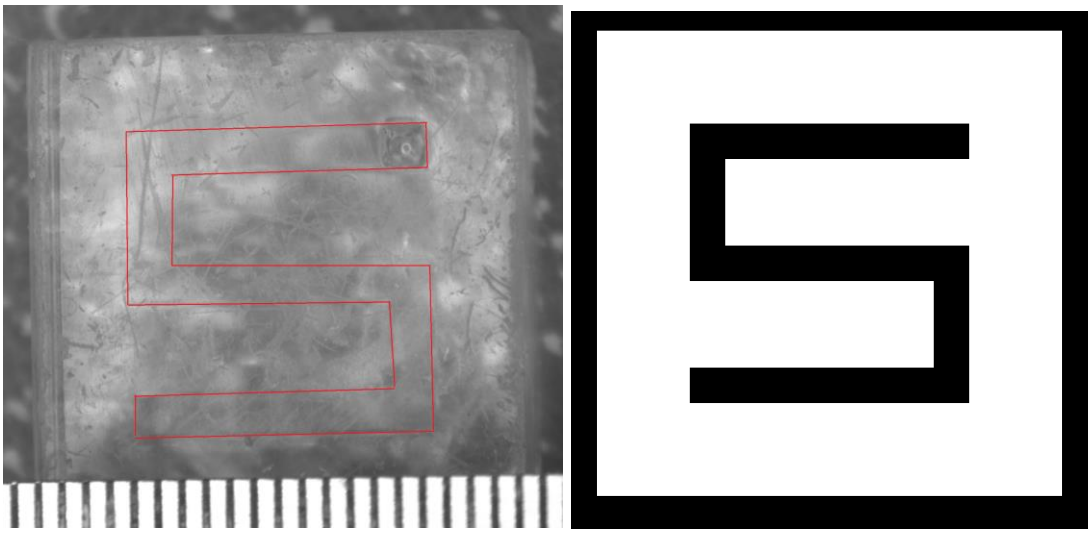

Figure 4.13. Stereomicrograph with a 0.5mm scale of the PEGDA microfluidic specimen with a 0.762 mm square channel (left) and the corresponding build image used to create the channel (right).

It was found that the snaking channel could be cleared with the 0.762mm channel size but not with the 0.381mm channel size. The layer thickness of 0.0762mm corresponds to a height of 10 layers for the larger channel but only 5 layers for the smaller channel. In photopolymerization processes there is always some amount of over-cure because otherwise there would be delamination between layers. In the case of this build the desired measured cure depth was 0.152 mm for a single exposure which is 2 times larger than the layer thickness. The over-cure makes it difficult to clear channels that are close in size to the cure depth and in this case the designed channel was only 2.5 times thicker than the measured cure depth. In Figure 4.14 a section view along the XZ plane of the 3D microfluidic design is shown along with a planar view of the corresponding cleaved PEGDA specimen.

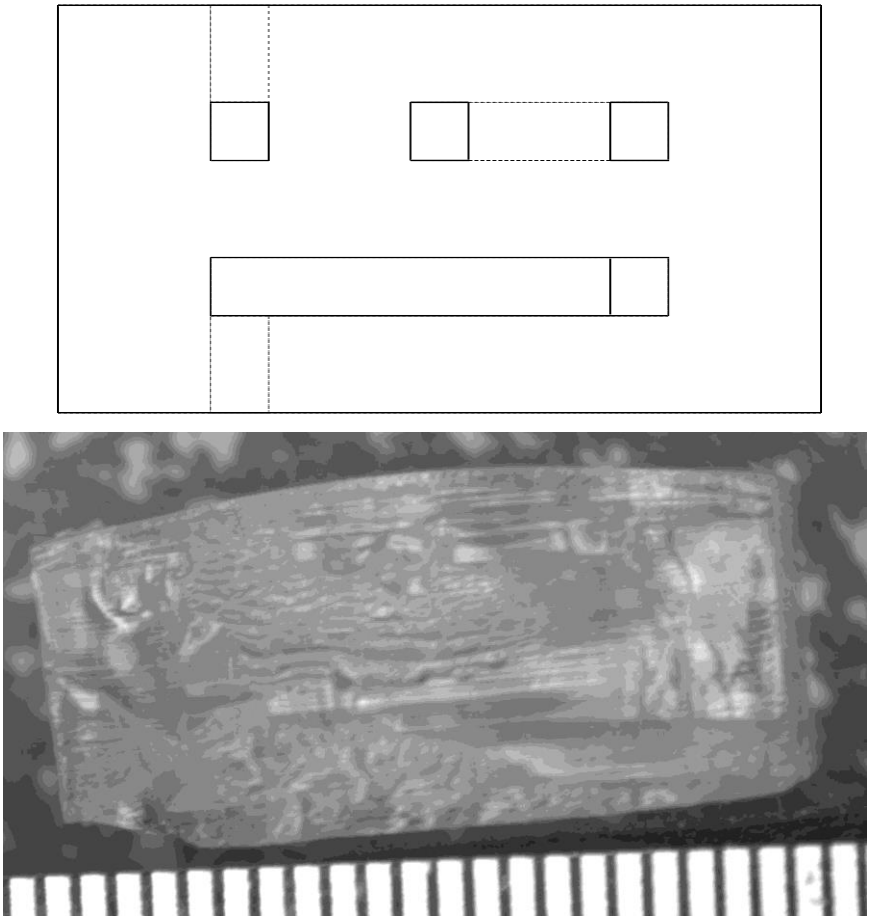

Figure 4.14. Section view of PEGDA microfluidic specimen design (top) and corresponding cleaved specimen (bottom) with 0.762 mm channel on a 0.5mm scale.

PEGDA microfluidic cylindrical geometries with helix channels as described in section 3.7 were fabricated by LAMP to investigate whether or not complex flow geometries could be fabricated and cleared. Images of the PEGDA microfluidic specimens after fabrication and breakout are shown in Figure 4.15.

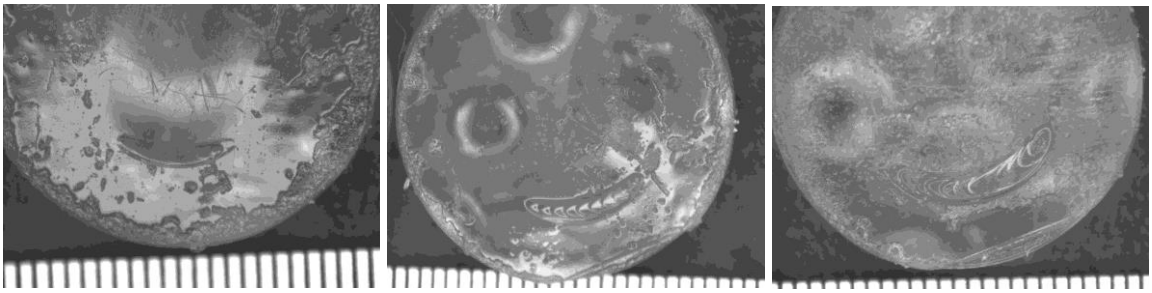

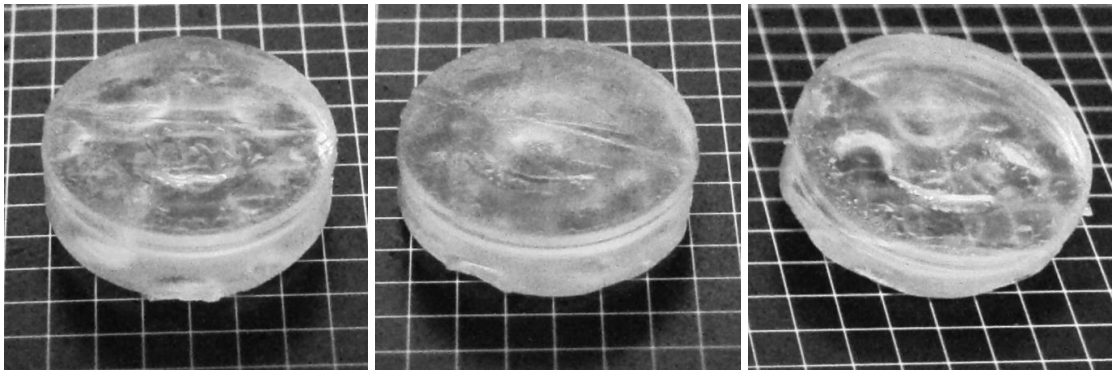

Figure 4.15. Stereomicrographs with a 0.5mm scale (top) and digital photographs with a 2mm grid (bottom) of cylindrical PEGDA microfluidic specimens with a helix circular channel having a cross-sectional diameter of 0.5 (left), 0.75 (center), and 1.0 mm (right).

PEGDA microfluidic cylindrical geometries with branching circular channels were also fabricated by LAMP. Images of the PEGDA microfluidic specimens after fabrication and breakout are shown in Figure 4.16.

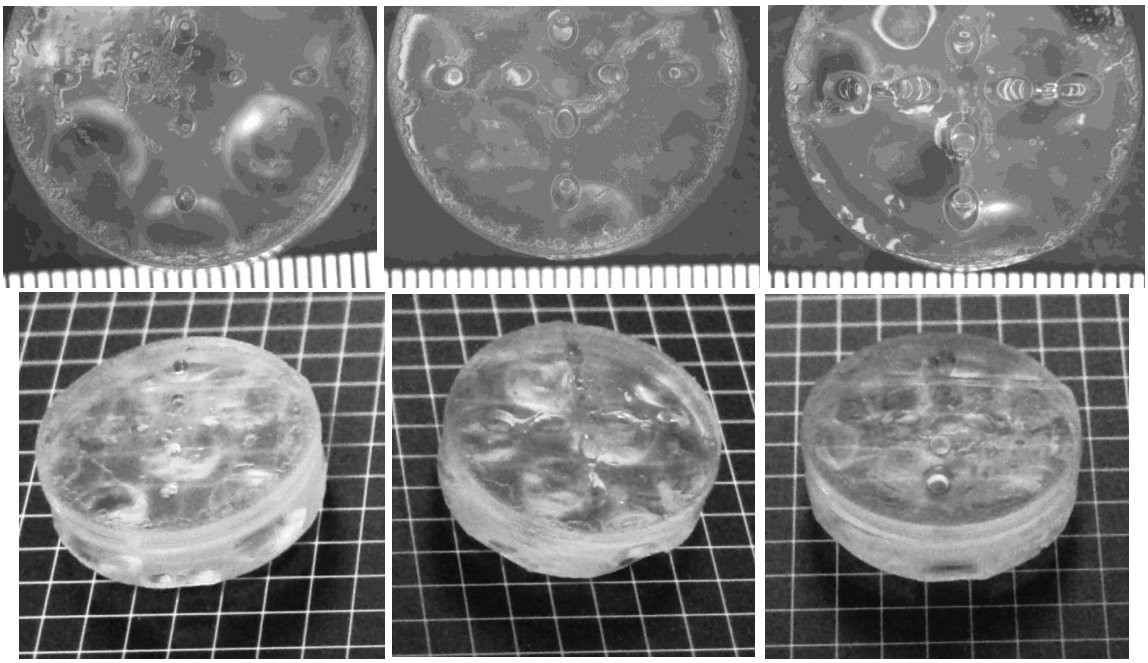

Figure 4.16. Stereomicrographs with a 0.5mm scale (top) and digital photographs with a 2mm grid (bottom) of cylindrical PEGDA microfluidic specimens with branching circular channels having cross-sectional diameters of 0.5 (left), 0.75 (center), and 1.0 mm (right).

It was observed that the helix and branching circular channels with 0.5, 0.75, and 1.0 mm diameters all cleared after breakout.

4.6 Computational Fluid Dynamics Simulations of PEGDA Scaffolds

The fluid velocity profiles for the PEGDA microfluidic geometries fabricated by LAMP that are described in section 3.8 were computed by CFD. Microfluidic geometries with channels oriented parallel (Z) and perpendicular (XY) to the build axis were created with large (0.071 mm^2), medium (0.031 mm^2), and small (0.018 mm^2) circular channels. As expected, the peak velocities were located in the center of the microfluidic channels, and the fluid velocity was effectively 0 in regions close to the walls and inside the fluid reservoir as can be seen in Figure 4.17.

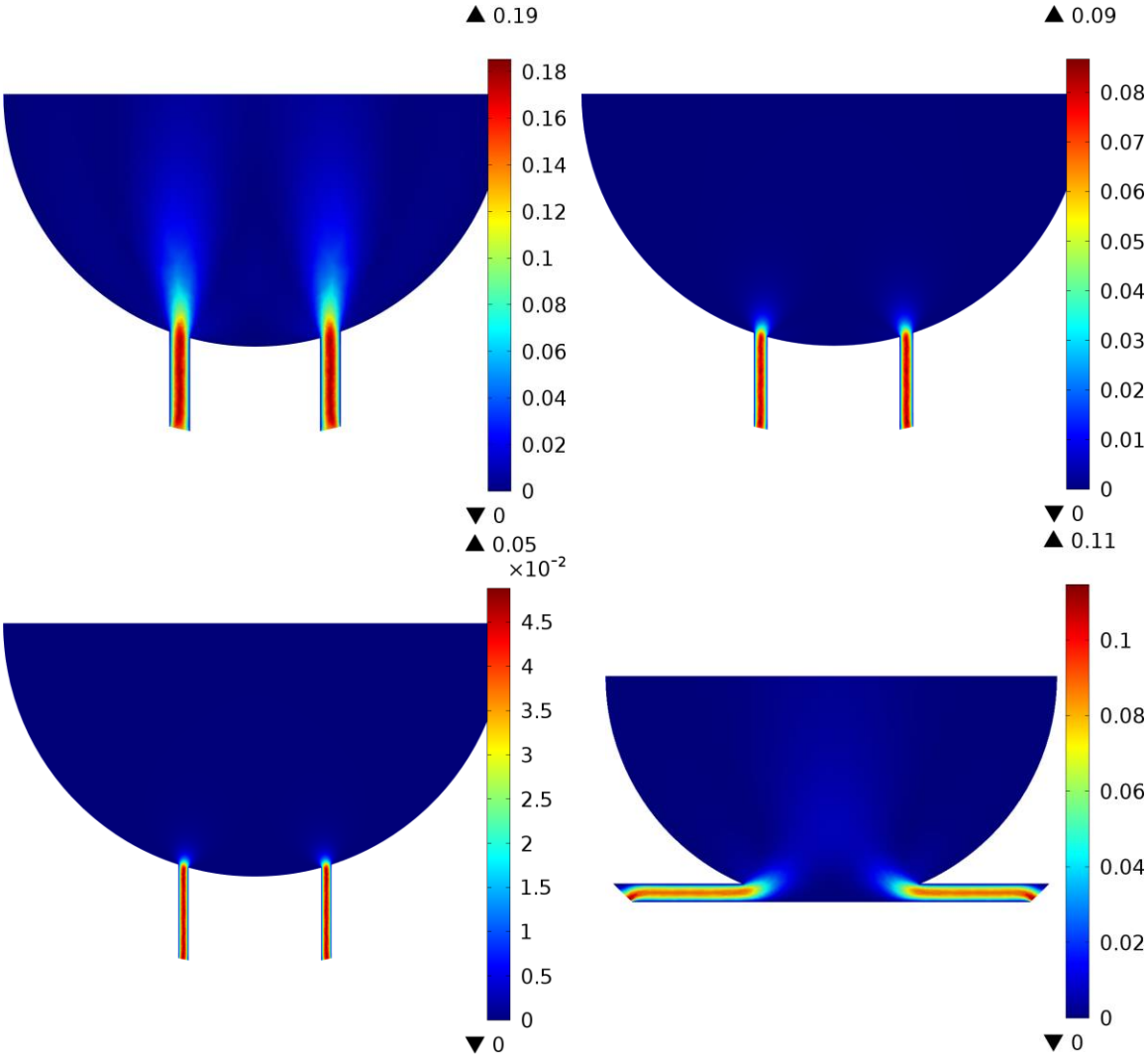

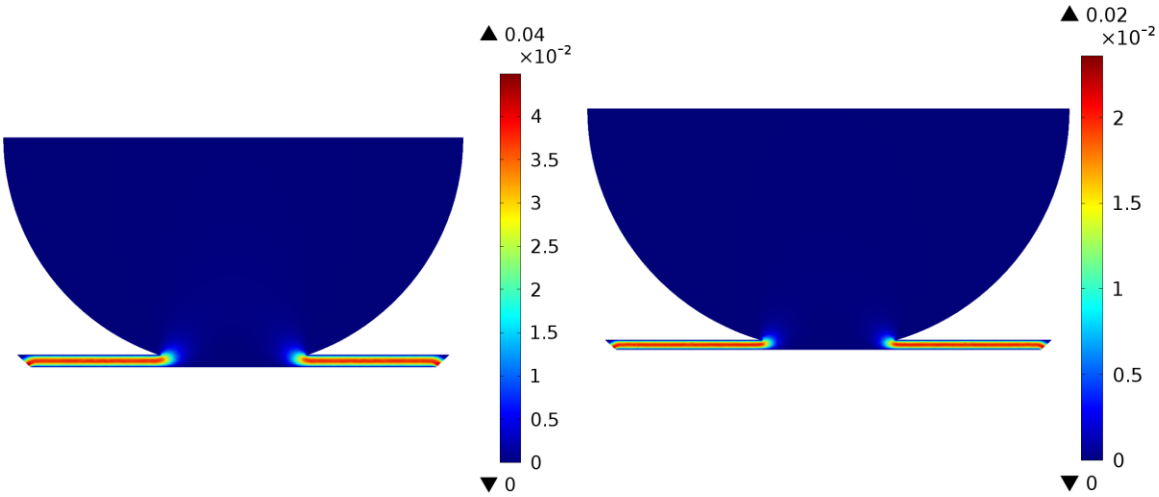

Figure 4.17. Velocity slice plots from CFD simulations of microfluidic geometries. Geometries with channels along the Z axis have (top-left) 0.071 mm^2, (top-right) 0.031 mm^2, and (middle-left) 0.018 mm^2 circular channels. Scaffolds with channels in the XY plane have (middle-right) 0.071 mm^2, (bottom-left) 0.031 mm^2, and (bottom-right) 0.018 mm^2 circular channels.

The volumetric flow rate through the channels was calculated by surface integration of the outlet surfaces and used to estimate the time it would take to drain the fluid reservoir for each geometry as shown in Table 4.10.

Table 4.10. Volumetric flow rates and drain times for CFD geometries

Geometry	Volume (mm^3)	Channel Area (mm^2)	Peak velocity (mm/s)	Flow rate (mm^3/s)	Drain Time (s)
Z-Large	1107.2	0.0707	185.12	265.198	4.175
Z-Medium	1105.1	0.0314	86.62	53.398	20.696
Z-Small	1104.4	0.0177	48.78	16.839	65.586
XY-Large	1110.3	0.0707	114.58	144.27	7.696
XY-Medium	1106.6	0.0314	44.85	25.707	43.047
XY-Small	1105.3	0.0177	23.57	7.6567	144.357

The peak velocities of the geometries with channels oriented in the z-direction were roughly twice that of geometries with channels oriented in the XY plane. Also, as the individual channel area reduced by a factor of $1/2$, the peak velocity was also reduced by a factor of $1/2$. It was observed that the estimated drain times were also much longer for XY-Medium and especially for XY-Small because the peak velocities

were reduced and the channels were not oriented along the direction of the volumetric force, in this case gravity. The estimated drain times for Z-Medium and XY-Medium were 21 and 43 seconds respectively while Z-Small and XY-Small were 66 and 144 seconds respectively. It is expected that at some point, the channel size will be too small for fabrication by LAMP and this will not allow fluid flow resulting in the model no longer being valid.

The original CAD files used to conduct the CFD analysis (Figure 3.16) were fabricated by LAMP. Validation of the CFD model was conducted by immersing the dome geometries in water and measuring the time to drain.

Table 4.11. Experimentally measured drain times for PEGDA specimens (n=6)

Geometry	CFD Drain Time (s)	Experimental Drain Time (s)	Error (%)
Z-Large	4.175	7.6±0.7	80.8
Z-Medium	20.696	31.1±2.0	50.4
Z-Small	65.586	81.8±6.8	24.7
XY-Large	7.696	9.2±0.9	19.5
XY-Medium	43.047	54.9±7.4	27.5
XY-Small	144.357	NA	NA

The measured drain times were found to be on average 40.6% higher than those predicted by CFD. The cause of the high error was likely due to the small size of the reservoirs and the fast drain time. It was observed that the XY-Small geometry which had a channel diameter of 150 μm did not fully clear the channels after breakout and cleaning and thus did not drain. This was expected based on the target cure depth used to fabricate the PEGDA specimens.

CHAPTER 5

CONCLUSIONS

This chapter concludes the dissertation. A summary of the dissertation is presented in section 5.1. The scientific and technical contributions of this work are outlined in section 5.2. Ideas for future work are given in section 5.3.

5.1 Summary of Dissertation

The objective of this dissertation was to investigate the fundamental scientific and engineering aspects of creating scaffolds for tissue engineering using additive manufacturing. This objective was achieved by utilizing two additive manufacturing technologies, SLS and LAMP, to investigate the processing and properties of tissue engineering scaffolds.

Chapter 3 describes the procedures used to produce PCL:HA scaffolds with SLS and PEGDA scaffolds with LAMP as well as to characterize them. Key processing parameters in SLS were identified by screening and then optimized using a design of experiments (DOE) approach to produce mechanically strong parts with SLS. Optical microscopy and micro-computed tomography were used to characterize internal geometry and microstructure of the scaffolds. Mechanical testing was used to characterize the mechanical properties, namely the stiffness and strength, of the scaffolds. A micromechanical computational model was developed to predict the bulk stiffness of PCL:HA composites at different filler loadings. A macroscale model was employed to estimate the effective stiffnesses of the different scaffold designs with varying levels of porosity. The design of microfluidic geometries with varying sizes and levels of complexity was discussed. Optical microscopy was used to characterize the channel

geometries that could be built by LAMP. A CFD model was developed to characterize the flow in PEGDA specimens with micro-sized channels. The CFD model was also experimentally validated with a simple fluid flow experiment.

Chapter 4 explains the results of fabrication, characterization, and modeling. In order to optimize the processing parameters for SLS, the manufacturing induced porosity, thermal growth, and curling of the parts were considered and a DOE approach was taken. After optimization, the PCL:HA scaffolds were processed using SLS to near full density (>98%) as determined by microscopic void fraction analysis. Geometrical accuracy was determined to be in the 3-8% range by μ-CT imaging and measurement with a caliper. The HA in the composite powders acted as an anti-caking agent and subsequently the powders with higher HA loading could be heated closer to the melting point of PCL and therefore a lower laser energy density could be used for processing. Mechanical characterization of the solid specimens showed that the stiffness of SLS processed neat PCL (363 MPa) was similar to injection molded parts (430 MPa) and in the lower range for trabecular bone (1-5000 MPa). Micro and macro-scale mechanical models were created to characterize the effect of changing HA loading on the bulk properties of the composites and to predict the effective stiffness of the scaffold geometries before compounding and fabrication. The computational model was found to have an average error of 25% when simulating compression along the build axis for scaffolds with 10, 20, and 30% HA loading in PCL.

It was found that LAMP was capable of manufacturing PEGDA hydrogel specimens with simple 1D channels at a size of 0.15 mm, simple 2D channels at a size of 0.2 mm, and complex 3D microfluidic channels at a size of 0.5 mm. Stair stepping was

observed in the PEGDA specimens that corresponded with the layer thickness of 76.2 µm. A CFD model was developed to investigate the velocity profile of a fluid traveling through 1D and 2D microfluidic circular channels with diameters of 0.15, 0.2, and 0.3 mm. As expected, it was observed that the peak velocity of the fluid was directly proportional to the cross-sectional area of the channels. The model was validated by experimentally measuring the drain times of the 1D and 2D specimens and comparing it with the drain times predicted by the model and an average error of 40.6% was measured. The large error was likely due to the small volume of the fluid reservoir.

5.2 Scientific and Technical Contributions

The contributions of this work are divided into the following categories:

1. Contributions to the fundamental scientific knowledge of creating scaffolds for tissue engineering by additive manufacturing
2. Technical contributions

5.2.1 Scientific Contributions

This dissertation gives new insight and understanding towards creating tissue engineering scaffolds by additive manufacturing. Hard and soft tissue scaffolds with complex 3D microarchitectures were designed and created using additive manufacturing methods.

Hard tissue scaffolds were created by SLS having fully interconnected porous channels with up to 81% porosity while not compromising on mechanical stiffness because the porous channels were created through engineering design. In general the change in effective stiffness of the scaffold corresponded with the reduction in minimum cross-sectional area; a 93.6% drop in cross-sectional area for the 81% porous PCL:HA

70:30 scaffold corresponded to a 92.7% reduction in effective stiffness. Multiple designs of biodegradable composite scaffolds with stiffnesses in the lower range of trabecular bone were fabricated by SLS. Optimization of the SLS processing parameters yielded results showing fully dense scaffolds with high geometric accuracy that have not previously been presented in the literature. A maximum stiffness of 498.3 MPa was achieved with a 70:30 PCL:HA composite that was shown to be stiffer than other PCL:HA composites manufactured by SLS that were reported by other groups including Eosoly et al. who reported a compressive modulus of 5.58 MPa at 30% loading [77]. The micromechanical model presented here gave estimations of the mechanical properties of 3D porous scaffolds that were much more accurate than others presented in the literature. Williams et al. [25] reported an average error of 100% for pure PCL scaffolds and Cahill et al. [47] reported an average error of 67% for PCL:TCP composite scaffolds; whereas, the model presented here has an average error of 25.65%. The model presented here likely has a better agreement with experiment because of two reasons: 1) a micromechanical model of the filler particles in the polymer matrix is used to characterize the bulk mechanical properties of the composite; and 2) the manufacturing induced porosity in the scaffolds (<1%) was much lower in this study than what was reported by others in the literature (>5%).

This dissertation demonstrates the capability to manufacture geometrically accurate 3D microarchitectured PCL:HA scaffolds with mechanical properties similar to conventionally manufacturing and in the lower range of trabecular bone. The results of the work presented in this dissertation yielded two peer reviewed articles [37, 43] on SLS of PCL and PCL:HA that have together generated over 140 citations at the time of

writing this dissertation. Many of the articles citing this work focus on the fabrication of polymeric scaffolds for tissue engineering using additive manufacturing techniques. The polymers investigated range from PVA to PEEK and hard fillers such as chitosan and β-TCP are also being investigated.

Soft tissue PEGDA specimens were created by LAMP with flow geometries having varying levels of complexity. It was observed that the 3D flow geometries were more difficult to build than 2D flow geometries, and the more complex channels had to be designed with larger channel area so that they could be cleared. Channels with an area of 0.018 mm^2 and a diameter of 0.150 mm could be created as long as they were simple straight channels; however, channels with a designed area of 0.145 mm^2 and a diameter of 0.381 mm did not clear when they were given a complex 3D path.

5.2.2 Technical Contributions

This dissertation contributes to the advancement of the state-of-the-art in additive manufacturing of tissue engineering scaffolds by demonstrating the capabilities of SLS and LAMP to fabricate hard and soft tissue scaffolds with complex 3D microarchitectures. The ability to use additive manufacturing to create tissue scaffolds with complex 3D microarchitectures is one step in the direction of creating scaffolds that can mimic the geometry of native tissue. The methodologies presented here to fabricate PCL:HA scaffolds with optimized geometric accuracy and mechanical properties have been cited by other groups to create their own scaffolds [47, 78]. A novel computational framework for modeling the mechanical properties of composite scaffolds with virtually any filler loading and architecture is also presented. The computational model is useful for designing the composite material system and scaffold geometry when knowing the

mechanical use conditions and complements the design for additive manufacturing process.

LAMP was utilized to manufacture PEGDA scaffolds that were optimized to have high feature resolution enabling the creation of complex 3D microfluidic geometries. A workable resin composition was developed to have the correct UV light sensitivity and viscosity for LAMP. The minimum channel sizes that could be fabricated for varying levels of channel path complexity were determined. A CFD model was created that could be used to investigate the movement of fluid within the microfluidic channels.

5.3 Future Work

Based on the work discussed in this dissertation, several recommendations for future work have been prepared.

1. A multifunctional scaffold with hard and soft regions embedded with channels that are joined together would be an interesting extension of this work. The soft part of the scaffold could be intended to interface with articular cartilage while the hard part of the scaffold could transition to bone. However, the interphase between the materials would be a challenging engineering problem.
2. Engineered structures such as I beams and composite structure arrangements as well as biomimetic structures such as Haversian canals and trabeculae could be built with SLS or another additive manufacturing technique. For the biomimetic structures, this would require improvements in the minimum feature size of the scaffolds.
3. PCL is limited in that its degradation time is on the order of 2 years which longer than what is typically needed for bone tissue engineering. New material systems

with faster degradation times that retain their mechanical strength during degradation can be investigated.

4. The micromechanical model for PCL:HA scaffolds can be expanded to characterize the scaffolds when under high strain.
5. A photoinitiator that has better absorption at longer wavelengths of light would be useful for LAMP because it would allow for lower concentrations of photoinitiator to be used.
6. Characterization of the effect of the stair-stepping caused by the layered manufacturing process on the roughness of the channels in the hydrogels scaffolds would give more information about the flow fields.
7. The mechanical properties of PEGDA scaffolds manufactured by LAMP can be characterized. Fillers such as nanoclays could be used to improve the mechanical properties of the scaffolds, but they would also increase the cost.
8. Modeling the O_2 consumption inside the tissue constructs could be used to inform the design of scaffolds with complex 3D flow geometries. Such geometries would likely be impossible to build using conventional manufacturing techniques but could be made with additive manufacturing.

APPENDIX A

COMPUTATIONAL MODELING OF SLS PROCESSED PCL:HA

Appendix A contains scripts and functions that were used to generate models of spherical HA particles in a PCL matrix for finite element analysis. A description of the methodology behind this approach is given in Chapter 3 section 4. A user must have "COMSOL with MATLAB" installed and then call the function "randompack.m" with a nonzero positive value for lambda. The helper function "HAupdate.m" is used to iteratively update the position matrix.

randompack.m

```
function [density fem] = randompack(lambda)

% Created by Shaun Eshraghi 09/01/10
% random packing of N spheres in a cube at 30% volume loading

N = 50; %number of HA particles
R = 25; %Radius of sphere (microns)

V_HA = 4/3*pi*R^3; %(um^3)
V = N*V_HA; %(um^3) total volume of HA
L = V^(1/3);

% position of sphere
for ii = 1:N
        HA(ii).pos = (L-2*R)*rand(1,3) - L/2+R;
end

% initialize matrix for distance to other spheres
for ii = 1:N
        HA(ii).dis = zeros(N,1);
end

for ii = 1:N
        HA(ii).dx = zeros(N,3); % initialize dx
end

%update HA.dis, HA.dx, and distances from HA.pos
```

```
[HA, distances] = HAupdate(HA);


done = 0;
c = 0;

while done == 0
        c = c + 1;
        a = min(min(distances));
        if a > 2*R
                w = 'win';
                break
        end
        I = find(distances==a);
        [m,n] = ind2sub(size(distances),I);
        HA(m).pos(1) = HA(m).pos(1) + HA(m).dx(n,1)*lambda;
        HA(m).pos(2) = HA(m).pos(2) + HA(m).dx(n,2)*lambda;
        HA(m).pos(3) = HA(m).pos(3) + HA(m).dx(n,3)*lambda;
        HA(n).pos(1) = HA(n).pos(1) + HA(n).dx(m,1)*lambda;
        HA(n).pos(2) = HA(n).pos(2) + HA(n).dx(m,2)*lambda;
        HA(n).pos(3) = HA(n).pos(3) + HA(n).dx(m,3)*lambda;

        [HA, distances] = HAupdate(HA);
end

% Block representing PCL matrix
b1 = block3(L,L,L,'base','corner','pos',[-L/2 -L/2 -L/2]);
L]);

%Sphere position matrix
pos = zeros(length(HA),3);
for ii=1:length(HA)
        pos(ii,:) = HA(ii).pos;
end

% Find spheres completely outside the box
f = 1;
for ii = 1:length(HA)
        x = abs(HA(ii).pos(1));
        y = abs(HA(ii).pos(2));
        z = abs(HA(ii).pos(3));
        dx = max(x-L/2,0);
        dy = max(y-L/2,0);
        dz = max(z-L/2,0);
        if dx^2 + dy^2 + dz^2 > R^2
                m1(f) = ii;
```

```
                f = f+1;
        end
end


%Delete Spheres completely outside the box
HA(m1) = [];

% Update sphere position matrix
pos = zeros(length(HA),3);
for ii=1:length(HA)
        pos(ii,:) = HA(ii).pos;
end

% Create Sphere Objects
g1 = struct([]);
for ii = 1:length(HA)
        g1{ii} = sphere3(R, 'pos', HA(ii).pos);
end

s1 = g1{1};
for ii = 2:length(g1)
        s1 = s1 + g1{ii};
end

% Crop these spheres
g2 = g1;
for ii = 1:length(HA)
        g2{ii} = g1{ii}*b1;
end

s2 = g2{1};
for ii = 2:length(g2)
        s2 = s2 + g2{ii};
end

% PCL Matrix
b4 = b1;
for ii = 1:length(HA)
        b4 = b4 - g1{ii};
end

g2{length(g2)+1} = b4;

fem = [];
```

```
fem = geomanalyze(fem,g2,'ns','CO1');
fem.mesh = meshinit(fem.geom,'report','off');
fem.xmesh = meshextend(fem);

V1 = postint(fem,'1');

density = V1/V;
```

HAupdate.m

```
function [HA, distances] = HAupdate(HA)

% helper function
% updates HA by using values from HA.pos to find new distances

N = length(HA);

%Update HA.dis from HA.pos

for ii = 1:N
        for jj = 1:N
                HA(ii).dis(jj) = sqrt((HA(ii).pos(1)-HA(jj).pos(1))^2 + (HA(ii).pos(2)-
                HA(jj).pos(2))^2 + (HA(ii).pos(3)-HA(jj).pos(3))^2); % dx(jj,1) =
                lambda_x, dx(jj,2) = lambda_y; distance from ii to jj
        end
end

% Update distances matrix

distances = zeros(N);

for ii = 1:N
        distances(ii,:) = HA(ii).dis';
end

for ii = 1:N
        distances(ii,1:ii) = NaN;
end

for ii = 1:N
        for jj = 1:N
                HA(ii).dx(jj,:) = (HA(ii).pos-HA(jj).pos)/HA(ii).dis(jj); % HA(ii).dx(jj,1)
                = lambda_x, HA(ii).dx(jj,2) = lambda_y; distance from sphere ii to jj
        end
end
```

APPENDIX B

SUPPLEMENTAL IMAGES OF PEGDA SPECIMENS

Appendix B contains supplemental images of the PEGDA specimens fabricated by LAMP. Images of the specimens used for validation of the CFD model are shown in Figure B 1.

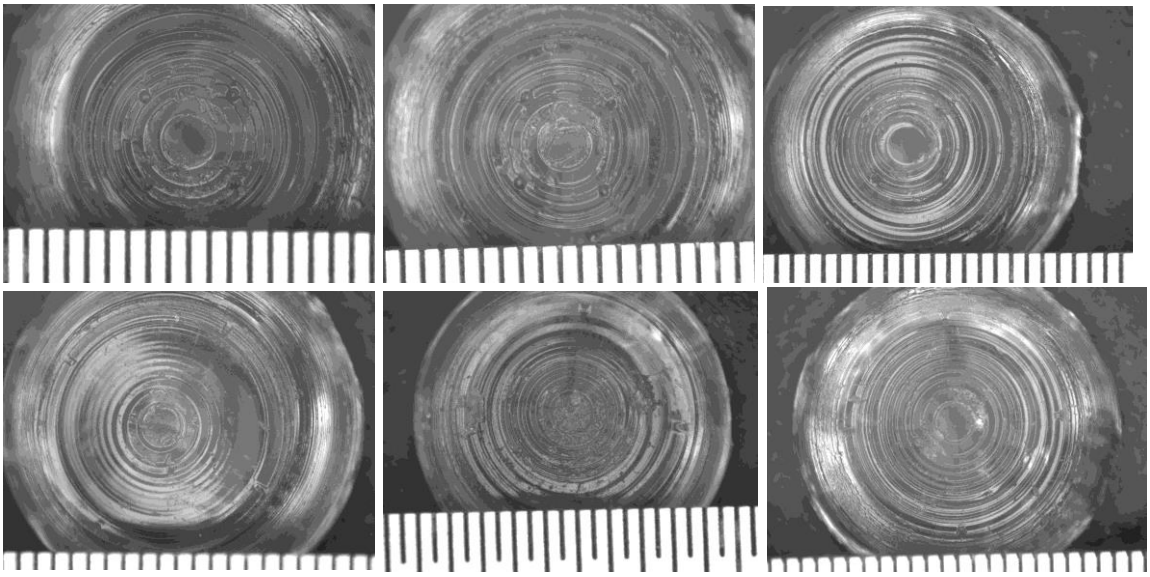

Figure B 1. PEGDA dome specimens for CFD validation with (top-left) 0.3, (top-middle) 0.2, and (top-right) 0.15 mm circular channels oriented in the Z direction and (bottom-left) 0.3, (bottom-middle) 0.2, and (bottom-right) 0.15 mm circular channels oriented in the XY directions.

APPENDIX C

REPRESENTATIVE IMAGES OF LAMP BUILDS

Representative images of the image stacks used to build the PEGDA specimens are given here.

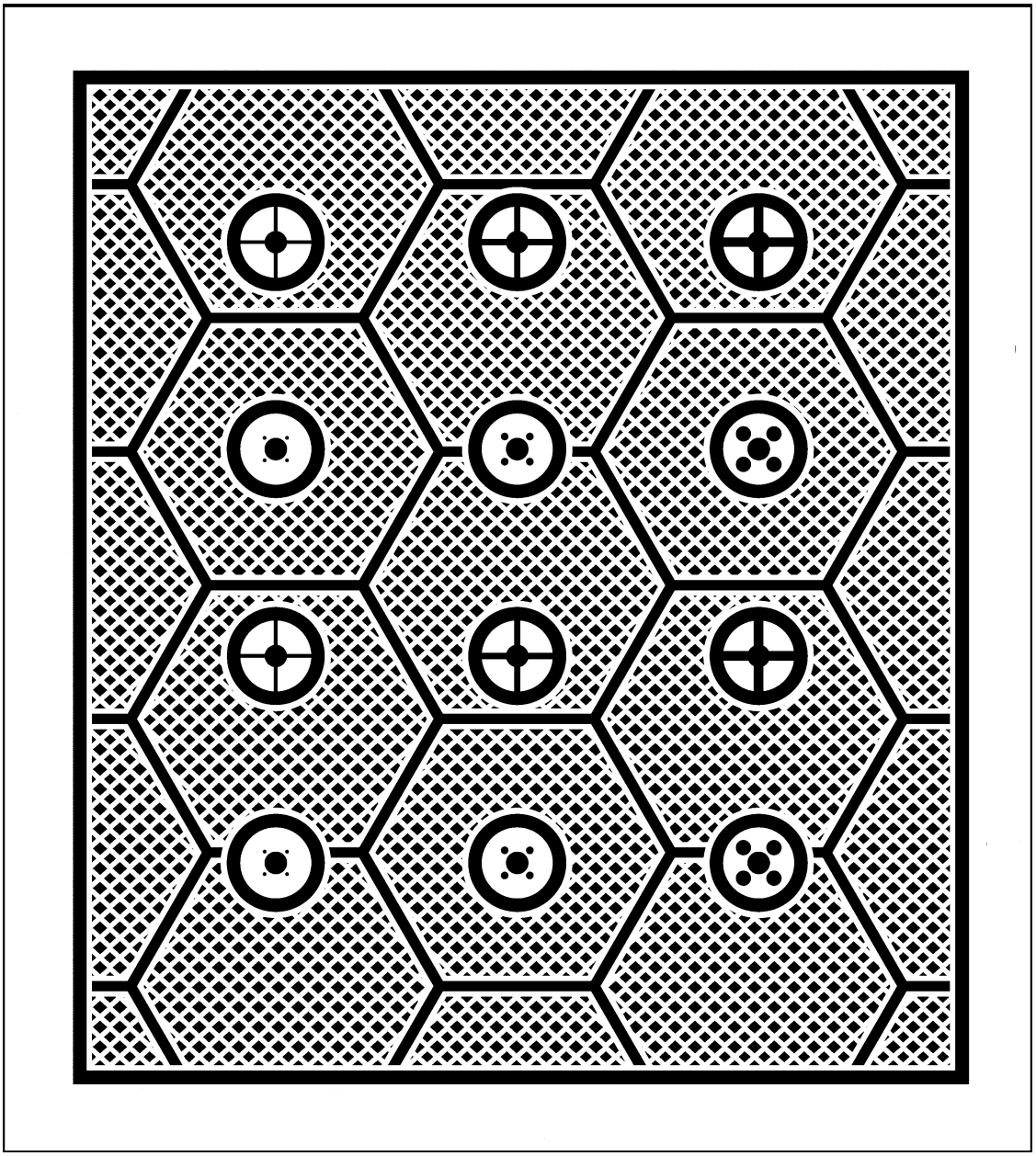

Figure C 1. Image number 47 of 65 of the LAMP build image stack for dome specimens with 0.375, 0.75, and 1.5 mm circular channels.

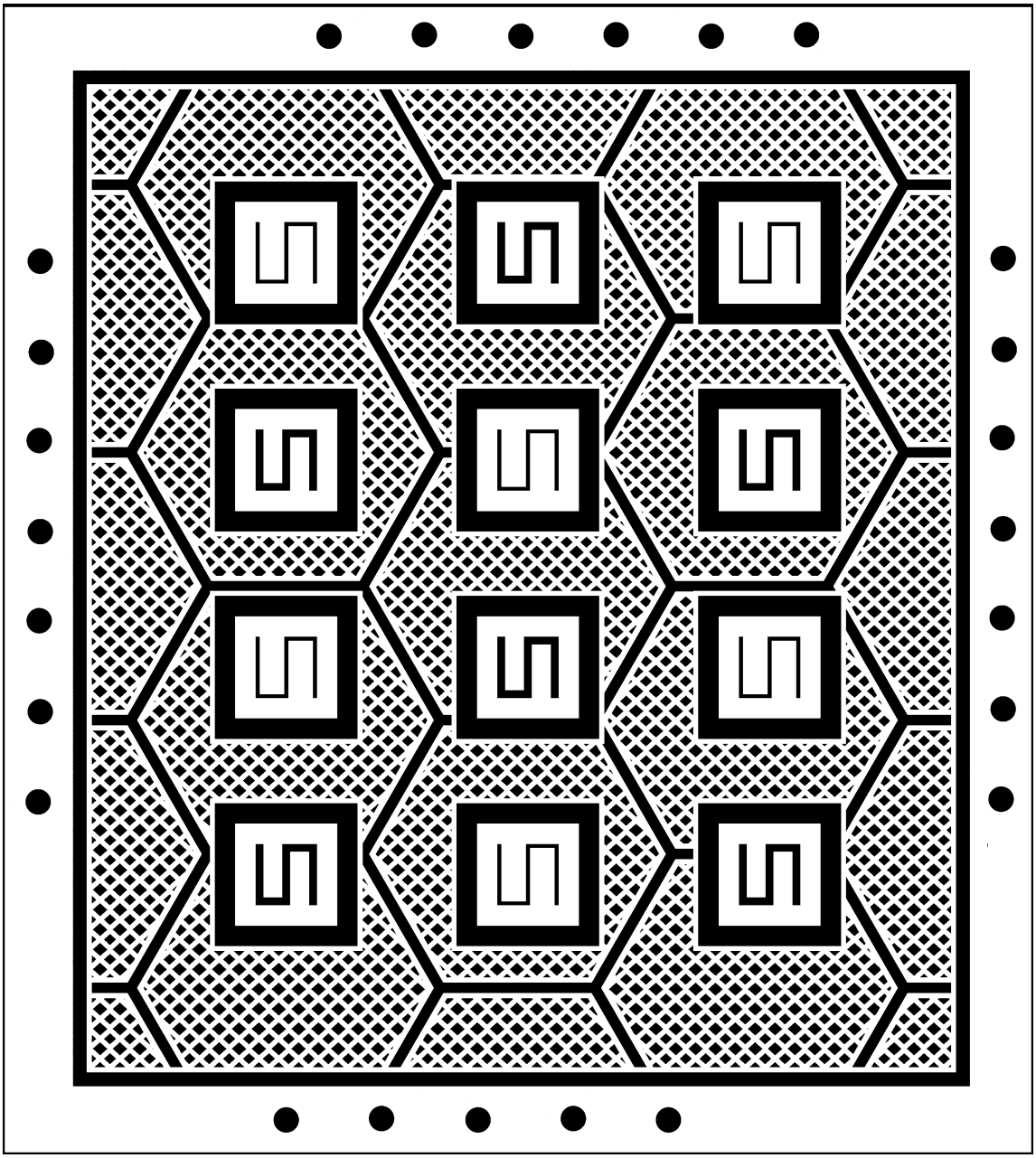

Figure C 2. Image number 50 of 70 of the LAMP build image stack for the snake shaped microfluidic flow specimens with 0.381 and 0.762 mm square channels.

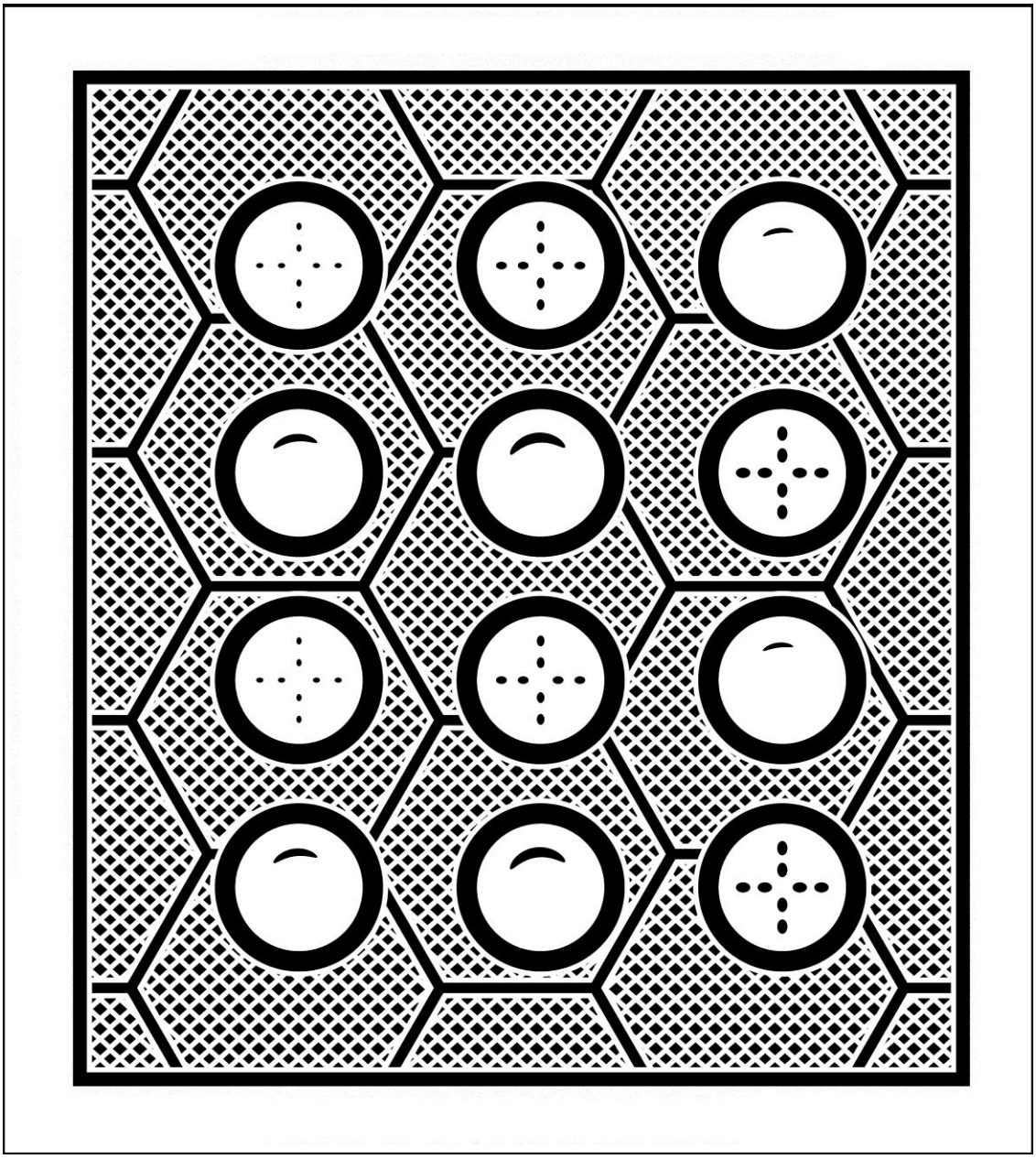

Figure C 3. Image number 65 of 67 of the LAMP build image stack for the helix and branch shaped microfluidic flow specimens with 0.5, 0.75, and 1.0 mm circular channels.

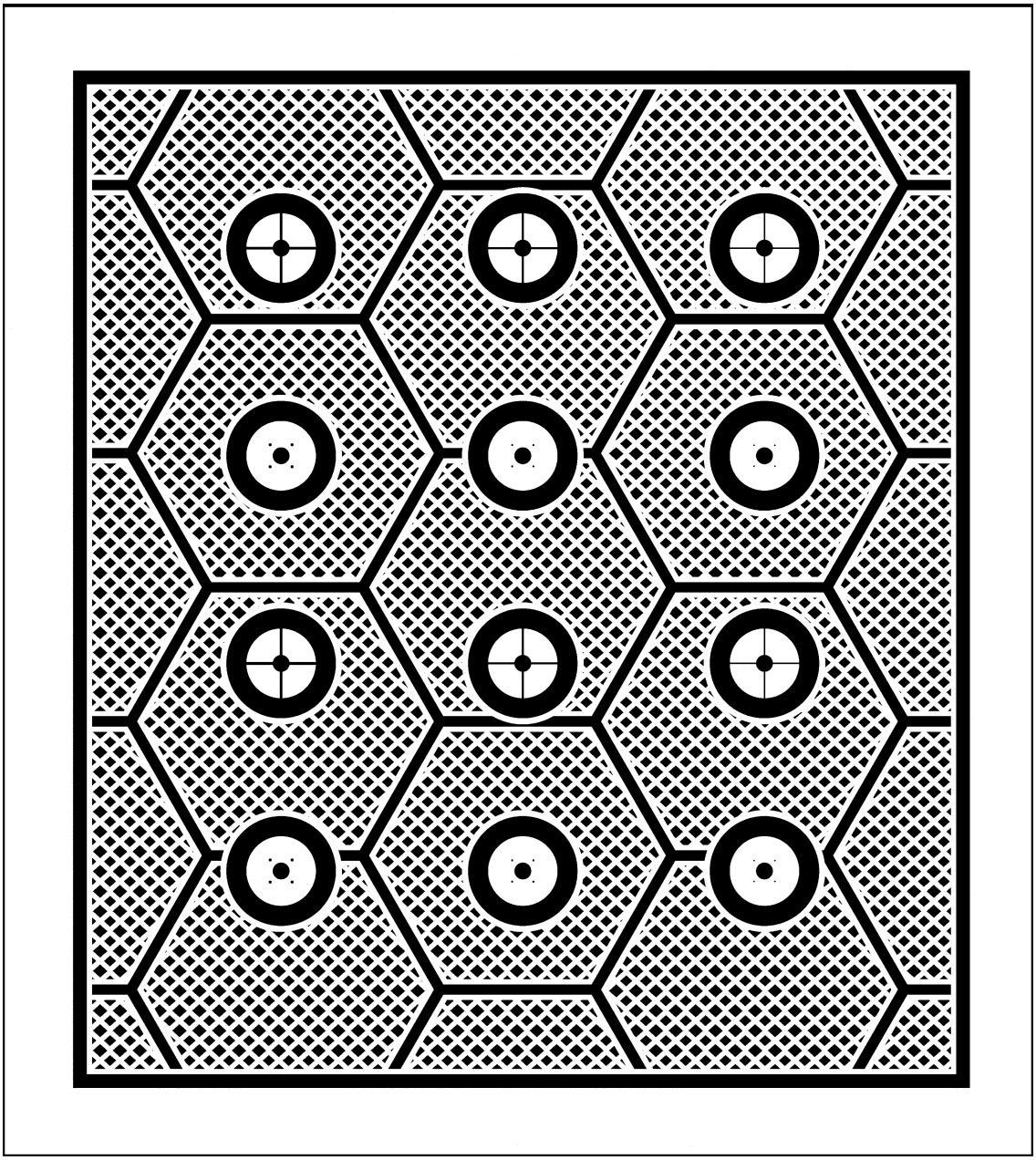

Figure C 4. Image number 48 of 66 of the LAMP build image stack for the CFD validation specimens with 0.15, 0.2, and 0.3 mm circular channels.

REFERENCES

1. Harris, L.D., B.-S. Kim, and D.J. Mooney, *Open pore biodegradable matrices formed with gas foaming.* 1998.
2. Liao, C.J., et al., *Fabrication of porous biodegradable polymer scaffolds using a solvent merging/particulate leaching method.* Journal of biomedical materials research, 2002. **59**(4): p. 676-681.
3. Hutmacher, D.W., *Scaffolds in tissue engineering bone and cartilage.* Biomaterials, 2000. **21**(24): p. 2529-2543.
4. ASTM, *Standard Terminology for Additive Manufacturing Technologies*, in *ASTM F2792-12a*. 2012: West Conshohocken, PA.
5. Deckard, C.R., *Selective Laser Sintering*, in *Mechanical Engineering*. 1988, University of Texas at Austin: Austin.
6. Cesarano III, J., et al., *Customization of Load-Bearing Hydroxyapatite Lattice Scaffolds.* International Journal of Applied Ceramic Technology, 2005. **2**(3): p. 212-220.
7. Hutmacher, D.W., M. Sittinger, and M.V. Risbud, *Scaffold-based tissue engineering: rationale for computer-aided design and solid free-form fabrication systems.* Trends in Biotechnology, 2004. **22**(7): p. 354-362.
8. Jiankang, H., et al., *Custom fabrication of composite tibial hemi-knee joint combining CAD/CAE/CAM techniques.* Proceedings of the Institution of Mechanical Engineers, Part H: Journal of Engineering in Medicine, 2006. **220**(8): p. 823-830.
9. Dyson, J.A., et al., *Development of Custom-Built Bone Scaffolds Using Mesenchymal Stem Cells and Apatite-Wollastonite Glass-Ceramics.* Tissue Engineering, 2007. **13**(12): p. 2891-2901.
10. Moroni, L., et al., *Finite Element Analysis of Meniscal Anatomical 3D Scaffolds: Implications for Tissue Engineering.* 2007.
11. Popov, V.K., et al., *Laser technologies for fabricating individual implants and matrices for tissue engineering.* J. Opt. Technol., 2007. **74**(9): p. 636-640.
12. Saijo, H., et al., *Maxillofacial reconstruction using custom-made artificial bones fabricated by inkjet printing technology.* Journal of Artificial Organs, 2009. **12**(3): p. 200-205.
13. Wu, G., et al., *Selective laser sintering technology for customized fabrication of facial prostheses.* The Journal of Prosthetic Dentistry, 2008. **100**(1): p. 56-60.
14. Berry, E., et al., *Preliminary experience with medical applications of rapid prototyping by selective laser sintering.* Medical engineering & physics, 1997. **19**(1): p. 90-96.
15. Rimell, J.T. and P.M. Marquis, *Selective laser sintering of ultra high molecular weight polyethylene for clinical applications.* Journal of Biomedical Materials Research, 2000. **53**(4): p. 414-420.
16. Leong, K., et al., *Fabrication of porous polymeric matrix drug delivery devices using the selective laser sintering technique.* Proceedings of the Institution of Mechanical Engineers, Part H: Journal of Engineering in Medicine, 2001. **215**(2): p. 191-192.

17. Shishkovsky, I., et al., *The synthesis of a biocomposite based on nickel titanium and hydroxyapatite under selective laser sintering conditions.* Technical Physics Letters, 2001. **27**(3): p. 211-213.
18. Popov, V.K., et al. *Selective laser sintering of 3-D biodegradable scaffolds for tissue engineering*. 2003.
19. Tan, K.H., et al., *Scaffold development using selective laser sintering of polyetheretherketone-hydroxyapatite biocomposite blends.* Biomaterials, 2003. **24**(18): p. 3115-3123.
20. Antonov, E.N., et al., *Three-Dimensional Bioactive and Biodegradable Scaffolds Fabricated by Surface-Selective Laser Sintering.* Advanced Materials, 2004. **17**(3): p. 327-330.
21. Chua, C.K., et al., *Development of tissue scaffolds using selective laser sintering of polyvinyl alcohol/hydroxyapatite biocomposite for craniofacial and joint defects.* Journal of Materials Science: Materials in Medicine, 2004. **15**(10): p. 1113-1121.
22. Kim, J. and T.S. Creasy, *Selective laser sintering characteristics of nylon 6/clay-reinforced nanocomposite.* Polymer Testing, 2004. **23**(6): p. 629-636.
23. Shi, Y., et al., *Effect of the properties of the polymer materials on the quality of selective laser sintering parts.* Proceedings of the Institution of Mechanical Engineers, Part L: Journal of Materials: Design and Applications, 2004. **218**(3): p. 247-252.
24. Tan, K.H., et al., *Selective laser sintering of biocompatible polymers for applications in tissue engineering.* Bio-Medical Materials and Engineering, 2005. **15**(1): p. 113-124.
25. Williams, J.M., et al., *Bone tissue engineering using polycaprolactone scaffolds fabricated via selective laser sintering.* Biomaterials, 2005. **26**(23): p. 4817-4827.
26. Partee, B., S.J. Hollister, and S. Das, *Selective laser sintering process optimization for layered manufacturing of CAPA® 6501 polycaprolactone bone tissue engineering scaffolds.* Journal of Manufacturing Science and Engineering, Transactions of the ASME, 2006. **128**(2): p. 531-540.
27. Huang, M.S., Suming Li, Dietmar Werner Hutmacher, Jan-Thorsten Schantz, Charles Alfred Vacanti, Christian Braud, Michel Vert,, *Degradation and cell culture studies on block copolymers prepared by ring opening polymerization of ε-caprolactone in the presence of poly(ethylene glycol).* Journal of Biomedical Materials Research Part A, 2004. **69A**(3): p. 417-427.
28. Nguyen, K.T. and J.L. West, *Photopolymerizable hydrogels for tissue engineering applications.* Biomaterials, 2002. **23**(22): p. 4307-4314.
29. Dhariwala, B., E. Hunt, and T. Boland, *Rapid prototyping of tissue-engineering constructs, using photopolymerizable hydrogels and stereolithography.* Tissue engineering, 2004. **10**(9-10): p. 1316-1322.
30. Beebe, D.J., et al., *Functional hydrogel structures for autonomous flow control inside microfluidic channels.* Nature, 2000. **404**(6778): p. 588-590.
31. Lu, Y., et al., *A digital micro-mirror device-based system for the microfabrication of complex, spatially patterned tissue engineering scaffolds.* Journal of Biomedical Materials Research Part A, 2006. **77**(2): p. 396-405.

32. Frenkel, J., *Viscous flow of crystalline bodies under the action of surface tension.* Journal of Physics (Moscow), 1945. **9**: p. 385-391.
33. Rudraraju, A., *Digital data processing and computational design for large area maskless photopolymerization*, in *Woodruff School of Mechanical Engineering*. 2013, Georgia Institute of Technology.
34. Alabi, T.R., *Design of photomodifiable material systems for maskless patterning of functional ceramic and metallic materials at multiple length scales*, in *Material Science and Engineering*. 2013, Georgia Institute of Technology.
35. Tomeckova, V. and J.W. Halloran, *Predictive models for the photopolymerization of ceramic suspensions.* Journal of the European Ceramic Society, 2010. **30**(14): p. 2833-2840.
36. Perstorp, *Biodegradable CAPA Thermoplastics*. 2003.
37. Eshraghi, S. and S. Das, *Mechanical and microstructural properties of polycaprolactone scaffolds with one-dimensional, two-dimensional, and three-dimensional orthogonally oriented porous architectures produced by selective laser sintering.* Acta Biomaterialia, 2010. **6**(7): p. 2467-2476.
38. Athreya, S.R., K. Kalaitzidou, and S. Das, *Processing and characterization of a carbon black-filled electrically conductive Nylon-12 nanocomposite produced by selective laser sintering.* Materials Science and Engineering A, 2010. **527**(10-11): p. 2637-2642.
39. Athreya, S.R., K. Kalaitzidou, and S. Das, *Mechanical and microstructural properties of Nylon-12/carbon black composites: Selective laser sintering versus melt compounding and injection molding.* Composites Science and Technology, 2011. **71**(4): p. 506-510.
40. Athreya, S.R., K. Kalaitzidou, and S. Das, *Microstructure, thermomechanical properties, and electrical conductivity of carbon black-filled nylon-12 nanocomposites prepared by selective laser sintering.* Polymer Engineering & Science, 2012. **52**(1): p. 12-20.
41. Chung, H. and S. Das, *Processing and properties of glass bead particulate-filled functionally graded Nylon-11 composites produced by selective laser sintering.* Materials Science and Engineering A, 2006. **437**(2): p. 226-234.
42. Chung, H. and S. Das, *Functionally graded Nylon-11/silica nanocomposites produced by selective laser sintering.* Materials Science and Engineering: A, 2008. **487**(1–2): p. 251-257.
43. Eshraghi, S. and S. Das, *Micromechanical finite-element modeling and experimental characterization of the compressive mechanical properties of polycaprolactone–hydroxyapatite composite scaffolds prepared by selective laser sintering for bone tissue engineering.* Acta Biomaterialia, 2012. **8**(8): p. 3138-3143.
44. Schneider, C.A., W.S. Rasband, and K.W. Eliceiri, *NIH Image to ImageJ: 25 years of image analysis.* Nat Methods, 2012. **9**(7): p. 671-5.
45. Jodrey, W. and E. Tory, *Computer simulation of close random packing of equal spheres.* Physical review A, 1985. **32**(4): p. 2347.
46. Partee, B., S.J. Hollister, and S. Das, *Selective laser sintering process optimization for layered manufacturing of CAPA 6501 polycaprolactone bone*

tissue engineering scaffolds. Transactions of the ASME. Journal of Manufacturing Science and Engineering, 2006. **128**(2): p. 531-40.
47. Cahill, S., S. Lohfeld, and P. McHugh, *Finite element predictions compared to experimental results for the effective modulus of bone tissue engineering scaffolds fabricated by selective laser sintering.* Journal of Materials Science: Materials in Medicine, 2009. **20**(6): p. 1255-1262.
48. Sartomer USA, L., *SR-610 data sheet*. 2014.
49. Ciba, *Irgacure® 2959*. 2014.
50. Bae, M., et al., *Fabrication of poly (ethylene glycol) hydrogel structures for pharmaceutical applications using electron beam and optical lithography.* Journal of Vacuum Science & Technology B, 2010. **28**(6): p. C6P24-C6P29.
51. Bidanda, B., et al., *Virtual prototyping & bio manufacturing in medical applications*. 2008: Springer.
52. Kim, J. and T. Creasy, *Selective laser sintering characteristics of nylon 6/clay-reinforced nanocomposite.* Polymer Testing, 2004. **23**(6): p. 629-636.
53. Pitt, C.G., et al., *Aliphatic polyesters. I. The degradation of poly (ε-caprolactone) in vivo.* J Appl Polym Sci, 1981. **26**: p. 3779-3787.
54. Pitt, C.G., et al., *Aliphatic polyesters II. The degradation of poly (DL-lactide), poly (ε-caprolactone), and their copolymers in vivo.* Biomaterials, 1981. **2**(4): p. 215-220.
55. Wehrenberg, R.H., *Lactic acid polymers: strong, degradable thermoplastics.* Mater. Eng, 1981. **94**(3): p. 63-66.
56. Engelberg, I. and J. Kohn, *Physico-mechanical properties of degradable polymers used in medical applications: A comparative study.* Biomaterials, 1991. **12**(3): p. 292-304.
57. Feng, X., C. Song, and W. Chen, *Synthesis and evaluation of biodegradable block copolymers of ε-caprolactone and D,L-lactide.* J. Polym. Sci. Polym. Lett., 1983. **21**(8): p. 593-600.
58. Vandamme, T.F. and R. Legras, *Physico-mechanical properties of poly(ε-caprolactone) for the construction of rumino-reticulum devices for grazing animals.* Biomaterials, 1995. **16**(18): p. 1395-1400.
59. Rosa, D.S., et al., *Evaluation of the thermal and mechanical properties of poly(ϵ-caprolactone), low-density polyethylene, and their blends.* Journal of Applied Polymer Science, 2004. **91**(6): p. 3909-3914.
60. Correlo, V.M., Luciano F. Boesel, Mrinal Bhattacharya, Joao F. Mano, Nuno M. Neves, Ruis L. Reis,, *Hydroxyapatite Reinforced Chitosan and Polyester Blends for Biomedical Applications.* Macromolecular Materials and Engineering, 2005. **290**(12): p. 1157-1165.
61. Granado, A., J.I. Eguiazábal, and J. Nazábal, *Structure and mechanical properties of blends of poly(ε-caprolactone) with a poly(amino ether).* Journal of Applied Polymer Science, 2008. **109**(6): p. 3892-3899.
62. Zein, I., et al., *Fused deposition modeling of novel scaffold architectures for tissue engineering applications.* Biomaterials, 2002. **23**(4): p. 1169-1185.
63. Shor, L., et al., *Precision extruding deposition (PED) fabrication of polycaprolactone (PCL) scaffolds for bone tissue engineering.* Biofabrication, 2009. **1**(1): p. 5003.

64. Kim, J., et al., *Cell adhesion and proliferation evaluation of SFF-based biodegradable scaffolds fabricated using multi-head deposition system.* Biofabrication, 2009. **1**(1): p. 5002.
65. Hutmacher, D.W., *Scaffold design and fabrication technologies for engineering tissues state of the art and future perspectives.* Journal of Biomaterials Science, Polymer Edition, 2001. **12**: p. 107-124.
66. Lam, C.X.F., S.H. Teoh, and D.W. Hutmacher, *Comparison of the degradation of polycaprolactone and polycaprolactone-(β-tricalcium phosphate) scaffolds in alkaline medium.* Polymer International, 2007. **56**(6): p. 718-728.
67. Zhou, Y., et al., *In vitro bone engineering based on polycaprolactone and polycaprolactone-tricalcium phosphate composites.* Polymer International, 2007. **56**(3): p. 333-342.
68. Wang, F., et al., *Precision extruding deposition and characterization of cellular poly-e-caprolactone tissue scaffolds.* Rapid Prototyping Journal, 2004. **10**(1): p. 42-49.
69. Goldstein, S.A., *The mechanical properties of trabecular bone: Dependence on anatomic location and function.* Journal of Biomechanics, 1987. **20**(11-12): p. 1055-1061.
70. Goulet, R.W., et al., *The relationship between the structural and orthogonal compressive properties of trabecular bone.* Journal of Biomechanics, 1994. **27**(4): p. 375-377, 379-389.
71. Lang, S., et al., *Correlation of mechanical properties of vertebral trabecular bone with equivalent mineral density as measured by computed tomography.* J Bone Joint Surg Am, 1988. **70**(10): p. 1531-1538.
72. Lotz, J.C., T.N. Gerhart, and W.C. Hayes, *Mechanical Properties of Trabecular Bone from the Proximal Femur: A Quantitative CT Study.* Journal of Computer Assisted Tomography, 1990. **14**(1): p. 107-114.
73. Mow, V., et al., *Basic orthopaedic biomechanics*. 1997: Lippincott-Raven Philadelphia.
74. Ouyang, J., et al., *Biomechanical characteristics of human trabecular bone.* Clinical Biomechanics, 1997. **12**(7-8): p. 522-524.
75. Porter, B.D., et al., *Mechanical Properties of a Biodegradable Bone Regeneration Scaffold.* Journal of Biomechanical Engineering, 2000. **122**(3): p. 286-288.
76. Lu, L., et al., *Mechanical study of polycaprolactone-hydroxyapatite porous scaffolds created by porogen-based solid freeform fabrication method.* Journal of applied biomaterials & functional materials, 2013. **12**(3): p. e145-54.
77. Eosoly, S., S. Lohfeld, and D. Brabazon, *Effect of Hydroxyapatite on Biodegradable Scaffolds Fabricated by SLS.* Key Eng Mater, 2009. **396**: p. 398.
78. Eosoly, S., et al., *Selective laser sintering of hydroxyapatite/poly-ε-caprolactone scaffolds.* Acta Biomaterialia, 2010. **6**(7): p. 2511-2517.